

Tidal Heating and Tidal Evolution in the Solar System

by

Jennifer Ann Meyer

Submitted to the Department of Earth, Atmospheric and Earth Sciences

in partial fulfillment of the requirements for the degree of

Doctor of Philosophy in Planetary Science

at the

MASSACHUSETTS INSTITUTE OF TECHNOLOGY

June 2011

© Massachusetts Institute of Technology 2011. All rights reserved.

Author

Department of Earth, Atmospheric and Earth Sciences

April 25, 2011

Certified by

Jack Wisdom

Professor

Thesis Supervisor

Accepted by

Maria Zuber

Chair, Earth, Atmospheric and Planetary Sciences

Tidal Heating and Tidal Evolution in the Solar System

by

Jennifer Ann Meyer

Submitted to the Department of Earth, Atmospheric and Earth Sciences
on April 25, 2011, in partial fulfillment of the
requirements for the degree of
Doctor of Philosophy in Planetary Science

Abstract

In this thesis, we examine the effects of tidal dissipation on solid bodies in application and in theory. First, we study the effects of tidal heating and tidal evolution in the Saturnian satellite system. We constrain the equilibrium heating of Enceladus to be less than $1.1(18000/Q_S)$ GW, where Q_S is the tidal quality factor of Saturn. The constraint on the heat flow is calculated from simple conservation of energy and angular momentum arguments and does not depend on the internal parameters of the satellites. We then look for dynamical disequilibrium by constructing a resonance model, tested by n-body integrations, to establish a consistent resonance history for Mimas, Enceladus, and Dione. We find that Enceladus is at or near equilibrium in its current 2:1 mean motion resonance with Dione. We also look for thermal disequilibrium using the oscillation model of Ojakangas and Stevenson (1986) [Icarus 66, 341-358]. We find that Enceladus does not experience oscillations in heat flow for any choice of parameters. We conclude that the most likely explanation for Enceladus' anomalous heat flow is a Q_S lower than 18,000, which implies either time or frequency dependent dissipation for Saturn.

Next, we create a coupled thermal-orbital model for the early evolution of the Moon. We compute the tidal heating in a dissipative lid overlying a magma ocean and the associated tidal evolution of the lunar orbit. We find that moderately high orbital eccentricities can be obtained, but show that the nonhydrostatic shape of the Moon cannot be explained by the shape solution of Garrick-Bethell et al. (2006) [Science 313, 652-655]. First, the orbit corresponding to the shape solution cannot be reached without stretching the tidal dissipation in the Earth to unphysically large values. Second, we show that the Moon will either crack or deform following the epoch of the shape solution and cannot maintain the shape until the present.

We continue our study of the Moon by considering the evolution of the precession of the lunar core as the Moon tidally evolves in its orbit. Early on in the Moon's history, we show that inertial coupling will force the spin axis of the core to precess along with the spin axis of the mantle. The coupling precludes a lunar dynamo before the Moon reaches a semimajor axis of 26.0-29.0 Earth radii. We also note that the Cassini transition happens after inertial coupling has weakened enough to allow

the core to precess independently. The time of the Cassini transition is therefore a promising epoch for the existence of a powerful lunar dynamo.

Finally, we present a new formulation of tides on solid bodies. Tidal deformations are modeled as the excitation of elastic modes. We derive general expressions for tidal heating, despinning, semimajor axis change, and eccentricity change for zero-obliquity bodies with a perturber on a non-inclined, eccentric orbit. We then specialize these equations to the constant time lag model and confirm our theory using the classical expressions.

Thesis Supervisor: Jack Wisdom

Title: Professor

Acknowledgments

It is a pleasure to thank the many people who made this thesis possible.

Foremost, I would like to express my sincere gratitude to my advisor, Professor Jack Wisdom, for his irreplaceable guidance, encouragement, and instruction in solar system dynamics.

I would also like to thank my committee members, Professor Benjamin Weiss, Professor Linda Elkins-Tanton, and Dr. Ruth Murray-Clay, for their time, effort, and mentorship.

Thanks also to my family and friends for making my time in graduate school fruitful and, dare I say, enjoyable.

Finally, an immense amount of gratitude to Leo Stein for his love and support.

Contents

1	Introduction	21
2	Tidal heating of Enceladus	29
2.1	Introduction	29
2.2	Heating from Torques	33
2.3	Equilibrium Eccentricity	37
2.4	Conclusion	40
3	Tidal evolution of Mimas, Enceladus, and Dione	45
3.1	Introduction	46
3.2	Model	47
3.3	Equilibrium Eccentricity	47
3.4	Enceladus-Dione 2:1 e -Enceladus Resonance—Future	49
3.5	Mimas-Enceladus 3:2 e -Enceladus Resonance	50
3.6	Mimas-Enceladus 6:4 ee' Resonance	51
3.7	Mimas-Enceladus 3:2 e -Mimas Resonance	52
3.8	Mimas-Dione 3:1 Resonance	53
3.9	Enceladus-Dione 2:1 e -Enceladus Resonance—Past	53
3.10	Discussion	56
3.11	Conclusion	57
3.12	Acknowledgements	60
4	Episodic Volcanism on Enceladus: Application of the Ojakangas-	

Stevenson Model	73
4.1 Introduction	73
4.2 Ojakangas and Stevenson Evolution Equations	74
4.3 Stability Analysis	77
4.4 Conclusion	78
5 Coupled Thermal-Orbital Evolution of the Early Moon	83
5.1 Introduction	83
5.2 Geochronology Constraints	85
5.3 The Orbital and Rotational Model	86
5.4 The Dissipative Lid Model	91
5.5 Elastic Stability of the Shape Solution	98
5.6 Conclusions	103
5.7 Acknowledgements	106
6 Precession of the Lunar Core	117
6.1 Introduction	117
6.2 Model and Results	119
6.3 Conclusion	125
6.4 Acknowledgments	126
7 Tidal theory in an elastic mode formulation	131
7.1 Introduction	131
7.2 Static Tidal Distortion	133
7.3 Tidal Disturbing Potential	136
7.4 Elastic Free Modes	136
7.5 Representation of Tidal Distortion by Elastic Modes	138
7.6 Lagrangian for Elastic Modes	140
7.7 Kinetic Energy	141
7.8 Potential Energy	144
7.9 Lagrangian and Equations of Motion	145

7.10	Chandler Wobble	148
7.11	Dissipation	151
7.12	Wobble Damping	153
7.13	Tidal Friction	154
7.14	Tidal Friction with Eccentricity	157
7.14.1	Orbital Evolution Not in Spin-Orbit Resonance	160
7.14.2	Orbital Evolution in Spin-Orbit Resonance	162
7.15	Conclusion	164
8	Conclusions and Future Work	167
A	The Resonance Model	171
B	Tidal Heating in a Two-Layer Model	177
C	Transition from Locked to Unlocked Core	183
D	Surface and Solid Spherical Harmonics	189

List of Figures

- 2-1 The approximate locations of the first-order resonances among the Saturnian satellites are shown for $Q_S = 18,000$. The shift of position of the resonances due to Saturn's oblateness has been ignored. Also shown are the tidally evolved orbits as a function of time. The dotted line shows the synchronous radius. The minimum Q_S is determined by placing Mimas at the synchronous radius at the beginning of the solar system. The current 2:1 and 4:2 resonances between Enceladus-Dione and Mimas-Tethys are not shown. 42
- 2-2 The eccentricity of Enceladus approaches an equilibrium value as the system evolves into the e -Enceladus 3:2 Mimas-Enceladus resonance. 43
- 2-3 The solid line shows the k_{2E}/Q_E for which the current configuration of Enceladus (with eccentricity 0.0047) and Dione is a tidal equilibrium for the given value of Q_S . The dotted line shows the value of k_{2E}/Q_E using Kelvin's formula for the Love number, using a rigidity of $4 \times 10^9 \text{N/m}^2$, and a Q of 20. The dashed line gives the equilibrium heating rate H in Enceladus as a function of Q_S 44
- 3-1 The future evolution of Enceladus's eccentricity as it evolves deeper into the Enceladus-Dione 2:1 e -Enceladus resonance. The system approaches equilibrium, but the libration amplitude is unstable and the eccentricity enters a chaotic phase with large variations in amplitude. Eventually the system falls out of resonance. Here k_2/Q of Enceladus is 8.6×10^{-5} 61

3-2	The future evolution of Enceladus's eccentricity in the Enceladus-Dione 2:1 e -Enceladus type resonance for $k_2/Q = 1.0 \times 10^{-4}$. After the chaotic phase the system enters a limit cycle in which the eccentricity oscillates.	62
3-3	The initial evolution, spanning 1.3 Gyr, for $k_2/Q = 1.0 \times 10^{-4}$ is shown in the phase plane $h_0 = e_0 \sin \sigma_0$ versus $k_0 = e_0 \cos \sigma_0$. The evolution begins with a libration near $\sigma_0 = 0$, the amplitude increases as the eccentricity increases. There is a chaotic transient which makes a splatter of points on the phase plane. The system eventually settles down on a limit cycle (see Figure 3-4).	63
3-4	The evolution of Enceladus in the Enceladus-Dione 2:1 e -Enceladus type resonance for $k_2/Q = 1.0 \times 10^{-4}$ eventually settles on a limit cycle, shown here in the phase plane $h_0 = e_0 \sin \sigma_0$ versus $k_0 = e_0 \cos \sigma_0$. The plotted segment of the orbit spans 3 Gyr.	64
3-5	The eccentricity of Enceladus in the Enceladus-Dione 2:1 e -Enceladus type resonance for $k_2/Q = 3.3 \times 10^{-4}$ reaches a stable equilibrium. The libration amplitude damps to zero.	65
3-6	The upper trace shows the evolution of the eccentricity of Mimas in the Mimas-Enceladus 6:4 mixed ee' resonance. The lower trace shows the evolution of the eccentricity of Enceladus. After leaving the resonance at -1.15 Gyr (for $Q_S = 18,000$), the eccentricity of Mimas decays to the current free eccentricity. Here k_2/Q for Mimas is 1.3×10^{-6} , and k_2/Q for Enceladus is 4.1×10^{-5} .	66
3-7	The evolution of the eccentricity of Mimas as it encounters the Mimas-Enceladus 3:2 e -Mimas resonance. The eccentricity approaches an equilibrium value of 0.052, but as it reaches equilibrium, the libration amplitude grows. Eventually the system escapes from the resonance and the eccentricity decays to the current value at the present. Here k_2/Q of Mimas is 1.42×10^{-6} and the timescale for eccentricity decay is about 1.3 Gyr.	67

- 3-8 The resonance angle of the Mimas-Enceladus 3:2 e -Mimas resonance versus time. There is a sudden growth in the libration amplitude because the system was captured by a 3-fold secondary resonance. When the amplitude reaches π , the system falls out of resonance. This figure corresponds to Figure 3-7. 68
- 3-9 The evolution of the eccentricity of Mimas as it encounters the Mimas-Dione 3:1 e^2 -Mimas resonance. The eccentricity grows to an equilibrium value of 0.07 before escaping the resonance and decaying to the present value of 0.02. Escape from the resonance occurs via unstable growth of the libration amplitude. Here k_2/Q for Mimas is 3.0×10^{-6} . 69
- 3-10 The past evolution of the eccentricity of Enceladus in the Enceladus-Dione 2:1 multiplet of resonances. Feature ‘b’ shows the entrance into the ee' resonance and feature ‘d’ shows capture into a 2:1 secondary resonance. In this simulation, the k_2/Q of Enceladus is the equilibrium value of 8.0×10^{-4} , so the constant equilibrium eccentricity of Enceladus, which it achieves shortly after it leaves the secondary resonance, is the current value of 0.0047. 70
- 3-11 The past evolution of the eccentricity of Dione in the Enceladus-Dione 2:1 multiplet of resonances. Feature ‘a’ shows passage through the e -Dione resonance. The rise in eccentricity between events ‘b’ and ‘c’ is due to the ee' -mixed resonance. The value of k_2/Q of Dione is 1.24×10^{-4} . 71
- 3-12 The solid line shows the k_2/Q for Mimas for which the eccentricity of Mimas will decay to the current value for a given Q_S if the system was caught in the Mimas-Dione 3:1 e^2 -Mimas resonance. The dotted line shows the k_2/Q for Mimas for which the eccentricity of Mimas will decay to the current value for a given Q_S if the system was caught in the Mimas-Enceladus 3:2 e -Mimas resonance. 72

4-1	The scaled eccentricity e_N (solid) and the non-dimensional heat flow q_N (dotted) are plotted versus the non-dimensional time for Io. The timescale τ_{th} is about 135Myr, the scale for the heatflow is 0.53 W m^{-2} , and the scale for the eccentricity is 0.0052. Here $m = 12$, $n = 25$, $(Q/k)_0 = 200/0.027$, $(Q/k)_{min} = 3/0.027$, and $Q_J = 10^5$	80
4-2	The scaled eccentricity e_N (solid) and the non-dimensional heat flow q_N (dotted) for Enceladus are plotted versus the non-dimensional time.	81
4-3	The parameter n' (solid) is plotted as a function of n , for Enceladus. This is to be compared with $m + p$ (dotted) plotted as a function of n . For $n' < m + p$ the system damps to the equilibrium state. The system is stable for all n . Here $(Q/k)_0$ is $100/0.0018$; $(Q/k)_{min}$ is $3/0.0018$; $T_0/T_m = 0.70$; and $m = 13$	82
5-1	The eccentricity of the lunar orbit plotted versus the semimajor axis of the orbit, for the dissipative lid model. For reference, the dot shows the orbit that gives the solution to the shape problem for synchronous rotation.	107
5-2	The tidal heating rate in the lid plotted versus time (solid line, see left axis). The radiogenic heating rate in the magma ocean is shown as a dotted line. The dashed line shows the orbital eccentricity versus time (see right axis).	108
5-3	The depth of the magma ocean δ_f (solid) and the depth of the lid δ_l (dotted) plotted versus the logarithm of the time. In this model the magma ocean disappears after about 217 Myr and the lid reaches its full depth of about 46.3 km.	109
5-4	The temperature at six layers in the lid plotted versus the logarithm of the time. The eccentricity behavior is as shown in Figure 5-1. The depths of each layer are 5 km, 10 km, 15 km, 20 km, 25 km, and 30 km. The temperature increases with depth. The horizontal line indicates the approximate closure temperature of zircon.	110

5-5	The temperature at six layers in the lid plotted versus the logarithm of the time. Here the eccentricity and consequently the tidal heating are set to zero. The depths of each layer are 5 km, 10 km, 15 km, 20 km, 25 km, and 30 km. The temperature increases with depth. The horizontal line indicates the approximate closure temperature of zircon.	111
5-6	Recalculation of Figure 1 from Peale, Cassen, and Reynolds (1979). This shows the ratio of the total dissipation in the two-layer model to the total dissipation in a homogeneous body ($\eta = 0$) plotted versus η , the fractional thickness of the interior.	112
5-7	The eccentricity of the lunar orbit plotted versus the semimajor axis of the orbit, for maximum realistic dissipation parameters. For reference, the dot shows the orbit that gives the solution to the shape problem for synchronous rotation.	113
5-8	The depth of the magma ocean δ_f (solid) and the depth of the lid δ_l (dotted), plotted versus the logarithm of the time using maximum realistic dissipation parameters. The magma ocean disappears after about 272 Myr, and the lid reaches its full depth of about 46.3 km.	114
5-9	The temperature at six layers in the lid plotted versus the logarithm of the time, for maximum realistic dissipation parameters. The depths of each layer are 5 km, 10 km, 15 km, 20 km, 25 km, and 30 km. The temperature increases with depth. The horizontal line indicates the approximate closure temperature of zircon. The temperatures are not significantly different from the temperatures in Figure 5-4.	115

- 6-1 The flattening of the lunar core plotted versus the assumed density of the core, for fixed core moment of inertia. For the non-hydrostatic mantle model, three curves are plotted. These three curves are the upper three on the plot and indistinguishable from each other. These three curves correspond to different core moments: $C_f/C = 0.8 \times 10^{-3}$, 1.2×10^{-3} and 1.6×10^{-3} . Similarly, the lower curves (also indistinguishable) show the results for the hydrostatic mantle model and the same core moment values. 127
- 6-2 The period of precession of the lunar orbit and lunar mantle (line A), of the lunar core in the “hydrostatic mantle” model (lines B), and of the lunar core in the “non-hydrostatic mantle” model (lines C), plotted as a function of lunar semimajor axis in Earth radii. For lines *B* and *C* the solid line takes into account the forced obliquity of the Moon, whereas the dashed line assumes zero obliquity. The gap in the non-hydrostatic mantle model occurs at the Cassini transition. The core precesses with the mantle when the Moon is close to the Earth; and the lunar core decouples from the mantle at large semimajor axis. The point of transition depends on the model. 128
- 6-3 The offset of the core spin axis from the mantle symmetry axis is plotted versus the core flattening for the equilibrium points of the system. The equilibrium points are found by adding a small dissipation and integrating the equations of motion. Two broken curves are shown. For the solid curve the full resonance Hamiltonian was used; for the dotted curve the nonlinearity parameter k was set to zero. For small flattening the offset of the core is approximately the obliquity; the core spin axis is perpendicular to the orbit. For large flattening, the offset tends to zero; the core spin axis is locked to the mantle. 129

7-1	The solid line shows the z component of the tidal shape function \vec{u}_T^0 . The dashed line shows the representation of the tidal shape function using the $n = 1$ elastic mode. The dotted line shows the representation using the $n = 1$ and $n = 2$ modes. The three mode representation is indistinguishable from the solid line on this scale.	139
C-1	The offset of the core spin axis from the mantle symmetry axis is plotted versus the core flattening for the equilibrium points of the system. The equilibrium points are found by adding a small dissipation and integrating the equations of motion. Two broken curves are shown. For the solid curve the full resonance Hamiltonian was used; for the dotted curve the nonlinearity parameter k was set to zero. For small flattening the offset of the core is approximately the obliquity; the core spin axis is perpendicular to the orbit. For large flattening, the offset tends to zero; the core spin axis is locked to the mantle.	187

List of Tables

4.1	The adopted physical parameters for Io and Enceladus are presented.	79
-----	---	----

Chapter 1

Introduction

Tides sculpt the solar system, creating such instantaneously dramatic effects as the plumes on Enceladus and also the slow inexorable drift of the Moon away from the Earth. As a secondary object orbits around a primary body, the gravitational force of the primary causes a distortion in the shape of the secondary, and vice versa. We can refer to one body as the perturber and the other body as the extended body, but both objects are causing and experiencing distortion. This distortion is the tidal bulge. Because the body experiences friction as the bulge is raised, the bulge is offset from the line from the primary to the secondary. This offset is quantified as the tidal phase lag δ , which is often related to the tidal quality factor $Q = \cot \delta$.

If the extended body is rotating significantly faster than the perturber is orbiting, the tidal bulge will lead the perturber. Then the bulge has a positive torque on the orbit of the perturber, increasing the semimajor axis. If the extended body rotates more slowly than the perturber orbits, the bulge will lag behind, creating a negative torque that decreases the semimajor axis of the orbit. The change in orbital angular momentum of the perturber is counterbalanced by change in rotational angular momentum of the extended body. Any change in the total rotational plus orbital energy is counterbalanced by heating in the extended body as a result of friction. So we see that tides can affect both the thermal evolution of a satellite's interior and the orbital evolution.

Chapter Two describes work published by Meyer & Wisdom (2007) on the tidal

heating of Enceladus. Enceladus presents quite a puzzle to planetary scientists. The 2005 Cassini flyby revealed active plumes emanating from the south pole (Porco et al., 2006) and a heat flow of 5.8 ± 1.9 GW (Spencer et al., 2006). This heat flow estimate has been revised upward as more flybys occurred. The most recent estimate is 17.0 ± 3.3 GW (Howett et al., 2010). This heat flow is higher than expected from traditional estimates of tidal heating and higher than on the neighboring satellites of Enceladus, such as Mimas. The conventional formula for tidal heating in a satellite around a primary is proportional to k_2/Q of the satellite, where k_2 is the Love number and Q is the tidal quality factor. Because these two parameters are largely unconstrained, the estimated tidal heating is very dependent on one's assumptions about the satellite properties.

We compute the equilibrium tidal heating of Enceladus in its current 2:1 mean motion resonance with Dione, independent of the satellites' physical properties. The resonance excites Enceladus' eccentricity e , while tidal dissipation damps the eccentricity. These two effects balance each other, resulting in constant eccentricity, when Enceladus is in tidal equilibrium. Energy is transferred to the satellites in the amount $n_0 T_0 + n_1 T_1$, where n is the mean motion and T is the torque from Saturn on each of the satellites, and some of that energy goes into expanding the orbits. The rest is dissipated as tidal heating in the interior of the satellites. Combining this argument with conservation of angular momentum L allows us to derive the maximum equilibrium tidal heating of a satellite in resonance:

$$H = \frac{n_0 T_0}{\sqrt{1 - e_0^2}} + \frac{n_1 T_1}{\sqrt{1 - e_1^2}} - \frac{T_0 + T_1}{L_0 + L_1} \left(\frac{GMm_0}{a_0} + \frac{GMm_1}{a_1} \right) = 1.1 (18000/Q_S) \text{ GW}. \quad (1.1)$$

The second equality is derived by using the masses, semi-major axes, and eccentricities of Enceladus and Dione, which are well known. No assumptions about the interior properties were required. The resulting heat flow depends only on the tidal quality factor Q of Saturn.

We argue that the minimum Q of Saturn is 18,000 because if the average Q of Saturn is less than that, Mimas's orbit would have evolved outward more than what

is observed. This constraint can be avoided if Saturn’s Q has changed over time or if the Q of Saturn is very frequency-dependent so that the Q applicable for Mimas is not the Q applicable for Enceladus. Alternatively, if Enceladus is not in tidal and thermal equilibrium, the heating rate could be higher.

Chapter Three describes our investigation into possible tidal disequilibrium for Enceladus, published by Meyer & Wisdom (2008b). If the current or very recent evolution in the 2:1 Enceladus-Dione resonance is chaotic or quasiperiodic, Enceladus’s eccentricity could be or have been temporarily higher than the equilibrium eccentricity, creating a heat flux above the equilibrium heat flux computed in Chapter Two.

In order to investigate this possibility, we characterized the current and past resonances experienced by Enceladus. First, we examined the orbital history of Enceladus and the other Saturnian satellites. We created a resonance model, verified by n-body integrations, and applied it to past resonances involving Mimas, Enceladus, and Dione to create an orbital history for the satellites, consistent with the current semimajor axes and eccentricities. This investigation included Enceladus’ current 2:1 resonance with Dione. The 2:1 resonance is split into a multiplet of resonances due to the oblateness of Saturn. Some of the resonances excite the eccentricity of Enceladus, some excite the eccentricity of Dione, and some excite a combination. Enceladus and Dione currently inhabit the e -resonance, which excites only the eccentricity of Enceladus. The e -resonance is located at the largest semimajor axis in the multiplet, so as Enceladus and Dione evolve outwards due to the tides from Saturn, they pass by or through all the other resonances in the multiplet.

We find that Enceladus evolves past the e' resonance that only excites the eccentricity of Dione, enters the ee' resonance, exits that resonance and enters the e resonance. As the system evolves deeper into this resonance, Enceladus enters a secondary resonance inside the e resonance, which causes chaotic variations in the eccentricity. However, we know that this resonance is in the past, based on the current semimajor axis ratio between Enceladus and Dione. Instead, we are currently in the regime immediately after these chaotic variations. Enceladus exits the secondary

resonance with an eccentricity very close to its equilibrium eccentricity in each simulation we performed. As a result, Enceladus reaches tidal equilibrium (constant eccentricity) almost immediately after leaving the secondary resonance. Based on this, we conclude that Enceladus is in or near tidal equilibrium today and that there is no resonance dynamic justification for a different amount of tidal heating than is described in Meyer & Wisdom (2007).

Chapter Four describes our investigation into thermal disequilibrium, published by Meyer & Wisdom (2008a), using a thermal oscillation model originally developed by Ojakangas & Stevenson (1986) for application to Io. The model relies on a temperature-dependent Q and a lag between eccentricity growth and melting/advection to create oscillations in both orbital eccentricity and heat flow. Due to Enceladus' smaller size compared to Io, this model does not produce oscillations - the system reaches equilibrium very quickly.

Chapter Five includes a study of the early evolution of the Moon, as published by Meyer et al. (2010). Tides have shaped the history of our Moon. The most accepted scenario for the formation of the Moon involves a giant impact between the Earth and a Mars-sized planetesimal that spewed out material which then coalesced into the Moon (Canup, 2004). The Moon formed in an orbit with a semimajor axis of only a few Earth radii and then tidal dissipation expanded its orbit to the current value of 60 Earth radii. Tides were especially strong very early in the Moon's life, when the Moon was close to the Earth and the Moon had a magma ocean.

We created a coupled thermal-orbital model for the Moon in order to explain two lunar mysteries: 1) the nonhydrostatic shape and 2) the discrepancy between the radiogenic ages of lunar zircons and the time that simple magma ocean cooling models predict. We use a Mignard orbital model and a thermal model that includes a conductive plagioclase lid over a convective magma ocean. We assume that all the tidal heating occurs in the lid. We find that large eccentricities can be obtained. Warm temperatures in the plagioclase lid persist long enough to solve the zircon discrepancy, if the zircons originated at depths of 25 km or more.

Garrrick-Bethell et al. (2006) found that the nonhydrostatic shape of the Moon

could be explained if the Moon froze in its shape under one of two conditions: in synchronous rotation when the orbit had a semimajor axis of 22.9 Earth radii and an eccentricity of 0.49 or in a 3:2 spin-orbit resonance with a semimajor axis of 24.8 Earth radii and an orbital eccentricity of 0.17. As the Moon’s evolution is currently understood, the Moon entered into synchronous rotation very early on in its lifetime, so we try to match the synchronous shape solution of Garrick-Bethell et al. (2006).

We find that our model can only produce an orbit that matches the shape solution if we stretch the dissipation in the Earth to unphysical values. To meet the shape solution, we require a time lag of 123 minutes with a completely fluid Love number for the Earth. The maximum time lag that is physically meaningful in the Mignard tidal model corresponds to a 45° phase lag, which is equivalent to a 37 minute time lag for our assumed initial rotation rate of the Earth. Using this maximum time lag, we find that a maximum eccentricity of 0.31 is physically realistic in our model.

We are nevertheless able to conclude that the shape solution of Garrick-Bethell et al. (2006) is unable to explain the nonhydrostatic shape of the Moon. A simple energy calculation can distinguish whether the shape can be maintained from the time of Garrick-Bethell’s shape solution to the present. If we assume that the Moon has the current shape at the semimajor axis and eccentricity given by the synchronous shape solution, as the orbit continues to evolve, that shape will no longer be the shape that corresponds to hydrostatic equilibrium. If the Moon maintains the shape as the orbit continues to change, energy will be stored as gravitational potential energy because the shape is no longer in hydrostatic equilibrium. Conversely, if the Moon loses the shape, energy will be stored as elastic energy in the deformed mantle. If we assume that the Moon will choose the lowest energy configuration, we can conclude that the Moon will deform immediately after the orbit evolves past the shape solution of Garrick-Bethell et al. (2006). Thus, a different explanation of the Moon’s nonhydrostatic shape is required.

Chapter Six describes the history of the precession of the lunar core and the consequences for a lunar dynamo, as published by Meyer & Wisdom (2011). The paleomagnetic signatures of Apollo samples are yet another lunar puzzle, best ex-

plained by a dynamo early on the Moon’s history. Dwyer & Stevenson (2005) have argued that the only plausible mechanism to power a lunar dynamo is mechanical stirring due to precession. This stirring requires relative motion between the spin axis of the core and the spin axis of the mantle, i.e. that the core and mantle do not precess together. Goldreich (1967) showed that a lunar core of low viscosity would not precess with the mantle today. But in the past when the Moon was closer to the Earth, the core-mantle boundary would be more elliptical and inertial coupling could act to lock the core spin axis to the mantle spin axis.

We studied the ellipticity of the core-mantle boundary over the course of the Moon’s history to determine when inertial coupling would be effective at preventing a lunar dynamo. We find that the transition from locked to unlocked core precession occurred between 26.0 and 29.0 Earth radii. Before the Moon reached these semimajor axes, a lunar dynamo would be precluded by inertial coupling. These semimajor axes were reached very quickly. In addition, we note that the Cassini transition occurs at about 34 Earth radii, after the transition to an unlocked core. During the Cassini transition, the mantle spin axis undergoes a dramatic reorientation and because the core spin axis will not be forced to follow, enormous amounts of stirring in the liquid core will result. The Cassini transition may be the best chance for a powerful lunar dynamo.

Chapter Seven describes a new formulation of solid body tides that models tidal displacements as a sum of excited elastic modes, analogous to the modeling of stellar tides as excited internal modes. The classical expressions for tidal heating, semimajor axis evolution, eccentricity evolution, and despinning are derived using a constant time lag tidal model, where a tide is raised by an imaginary perturber displaced by a constant time lag along the orbit from the real perturber. This model assumes that the tidally distorted body is synchronously rotating, completely elastic and incompressible, small enough for the relationship between the Love numbers $h_2 = 5/3k_2$ to hold, and that Q is inversely proportional to frequency, so that the tidal bulge is offset by a constant time offset Δt , not a constant angle offset.

This list of assumptions is both long and not necessarily applicable in many physi-

cal situations. One of the most questionable assumptions is the frequency dependence of the dissipation. For instance, while the Earth-Moon system fulfills many of the above criteria such as synchronicity, the measured Q of the Moon is roughly frequency-independent (Williams, 2008) over the limited frequency range studied. Terrestrial geophysicists have studied the Earth over a broader frequency range and have found more complicated frequency dependences, such as described in the Andrade model or Burgers model. Planetary scientists do not understand the frequency dependence of Q , but as far as we do, the constant Δt model seems like a poor choice. The widespread use of the constant time lag model is due to its mathematical tractability, not to any physical evidence in favor of it. Yet, the constant time lag model is the only tidal model with published analytic (not numerical) expressions for tidal heating and orbital decay at high eccentricity (Wisdom, 2008).

Describing tides as excited elastic modes allows us to derive tidal dissipation expressions as sums of terms that include the phase lags as generic functions of frequency. Instead of assuming a constant time lag from the beginning of the derivation, as in the classical derivations, we can derive formulae applicable for any frequency dependence and then insert a phase lag with arbitrary frequency dependence. Our elastic mode formulation is mathematically cleaner than the alternatives and assumptions about the tidal frequency dependence enter into the theory in a more modular way. Here we present the derivation of the tidal formulation and the application to the Kelvin-Voigt rheology that corresponds to the constant time lag tidal model.

Chapter Eight contains our conclusions and directions for future effort.

Chapter 2

Tidal heating of Enceladus

The heating in Enceladus in an equilibrium resonant configuration with other Saturnian satellites can be estimated independently of the physical properties of Enceladus. We find that equilibrium tidal heating cannot account for the heat that is observed to be coming from Enceladus. Equilibrium heating in possible past resonances likewise cannot explain prior resurfacing events.

2.1 Introduction

Enceladus is a puzzle. Cassini observed active plumes emanating from Enceladus (Porco et al., 2006). The plumes consist almost entirely of water vapor, with entrained water ice particles of typical size $1\mu\text{m}$. Models of the plumes suggest the existence of liquid water as close as 7m to the surface (Porco et al., 2006). An alternate model has the water originate in a clathrate reservoir (Kieffer et al., 2006). Both models require substantial energy input to drive the plumes. The plumes originate in the features dubbed the “tiger stripes,” in the south polar terrain. The heat emanating from the south polar terrain has been estimated to be 5.8 ± 1.9 GW (Spencer et al., 2006). Howett et al. (2010) has revised the heat flow upward to 17.0 ± 3.3 GW using the additional data from multiple Cassini flybys. Some heating mechanism provides about 17 GW of energy to the system. The estimated rate of radiogenic heating is 0.32 GW, and the estimated current rate of tidal heating resulting from the small

orbital eccentricity of Enceladus is about 0.12 GW, for an assumed k_2 of 0.0018 and a Q of 20 (Porco et al., 2006). So these sources of heating are inadequate.

Squyres et al. (1983) remark that even if the current rate of tidal heating was sufficient to maintain Enceladus in an active state, much greater heating would be required to initiate the process. They suggest that heating of order 25 GW is necessary to initiate melting, and propose that this might have been obtained by a much larger orbital eccentricity.

Any mechanism for supplying the required energy must pass the “Mimas test” (Squyres et al., 1983). Mimas has an ancient surface, but is closer to Saturn than Enceladus and has a larger orbital eccentricity. Any mechanism that is proposed to heat Enceladus must not substantially heat Mimas. Using the conventional tidal heating formula (Peale & Cassen, 1978; Peale, 2003), the estimated tidal heating in Mimas is about 30 times the heating in Enceladus, if the rigidity of the two bodies is the same. Thus conventional tidal heating in the current orbital configuration does not pass the test.

One mechanism for heating Enceladus that passes the Mimas test is the secondary spin-orbit libration model (Wisdom, 2004). Fits to the shape of Enceladus from Voyager images indicated that the frequency of small amplitude oscillations about the Saturn-pointing orientation of Enceladus was about 1/3 of the orbital frequency. In the phase-space of the spin-orbit problem near the damped synchronous state the stable equilibrium bifurcates into a period-tripled state. If Enceladus were trapped in this bifurcated state, then there could be several orders of magnitude greater heating than that given by the conventional tidal heating formula. What was special about Enceladus compared to Mimas was its shape. New fits of the shape to Cassini images of Enceladus showed that Enceladus was not near the 3:1 secondary resonance, but, remarkably, was near the 4:1 secondary resonance (Porco et al., 2006). A similar analysis shows that if caught in this secondary resonance, the system could again be subject to several orders of magnitude additional heating. Unfortunately, the predicted libration was not seen. An upper limit placed on the magnitude of the libration was 1.5 degrees, which in turn places an upper limit on the heating from the

secondary resonance mechanism of 0.18 GW (Porco et al., 2006). So if the limits of the libration amplitude are reliable, then the secondary resonance spin-orbit mechanism is ruled out for the present system. It may still be possible that the system was locked in this resonance in the past. Note that the large heating that would result from libration in the secondary resonance would damp the orbital eccentricity, and at sufficiently small eccentricity the secondary resonance becomes unstable. Thus the secondary resonance mechanism could at most produce an episode of heating.

Lissauer et al. (1984) suggested that Enceladus might have recently been involved in a 2:1 mean motion resonance with Janus. Janus is evolving outwards due to torques from Saturn's rings. At present, Janus is just 1000 km outside the resonance. Only a few tens of millions of years ago Janus was at the resonance. If Janus encountered the resonance when the eccentricity of Enceladus was low, the probability of capture into the e -Enceladus resonance would be high. They found that if Janus and Enceladus were trapped in the resonance and were in an equilibrium configuration then Enceladus would be subject to 4.5 GW of heating, which is comparable to the observed heating. But the model has numerous limitations (Peale, 2003). The value of the mass of Janus has been revised downwards, and this leads to smaller tidal heating (see below). The angular momentum in the A-ring is limited, so the resonance could only have persisted for a limited time in the past. More importantly, Enceladus shows evidence of multiple resurfacing episodes. The resonance with Janus could at most explain the most recent activity. In addition, the model has to appeal to an impact to get the system out of the resonance. The alternative escape mechanism suggested is that the Janus resonance became unstable when the Enceladus-Dione resonance was reached. But this seems unlikely, as Enceladus and Dione are not deeply in the resonance and Dione has little effect on the orbital evolution of Enceladus at present (Sinclair, 1983). There may also be a problem damping down the implied equilibrium eccentricity of Enceladus to the present low value of 0.0047 in the short time (tens of millions of years) since the resonance was purportedly disrupted. Actually, the simplest scenario for the encounter of Janus with the 2:1 e -Enceladus Janus-Enceladus resonance is that Janus just passed through the resonance with little effect on the

orbit of Enceladus. In this scenario Janus encounters Enceladus at its current eccentricity, but at this eccentricity the system has a low probability of being captured by the resonance. We find that the capture probability at the current eccentricity of Enceladus is only 0.7%.

There are other possibilities for resonance configurations involving Enceladus in the past (see Figure 2-1). Perhaps tidal heating in these resonances was responsible for past resurfacing events. These resonances include the 3:2 Mimas-Enceladus and the 3:4 Enceladus-Tethys resonances. If the Q of Saturn is sufficiently low, numerous other resonances could have been encountered. Evolution through these has not been studied in detail, but we can estimate the equilibrium tidal heating expected while trapped in the resonances (see below).

Ross & Schubert (1989) investigated tidal heating in Enceladus using multilayered viscoelastic models of the satellite. They found that equilibrium heating in a homogeneous Maxwell model at the current eccentricity can be as large as 920 GW. The heating is proportional to the Love number of the satellite and in the viscoelastic models the dynamic Love number can be orders of magnitude larger than the elastic Love number. They also investigated heating in a two layer model consisting of a conductive elastic lithosphere overlying a Maxwell interior and a three layer model with a liquid water-ammonia layer between the lithosphere and the Maxwell core. These models are tuned to give a heating rate of about 4 GW, similar to that found by Lissauer et al. (1984) in their Janus model. These models require a low conductivity insulating layer. Thus, it appears to be possible for tidal heating to provide enough input energy to account for the observed energy output from Enceladus. The Mimas test is not addressed by these models; it seems likely that if similar viscoelastic models were applied to Mimas then there would also be large tidal heating in Mimas, contradicting its cold inactive state. Nevertheless, viscoelastic enhancement of the Love number has been presented as a simple solution to the problem of heating Enceladus (Spencer et al., 2006; Stevenson, 2006).

In this paper we calculate the equilibrium rates of tidal heating in Enceladus independent of the physical properties of Enceladus, based on conservation of energy

and angular momentum. We find that tidal heating in Enceladus is much less than the observed radiated heat.

2.2 Heating from Torques

One mechanism of heating is tidal dissipation in a synchronously rotating satellite. As a system evolves deeper into an eccentricity-type resonance, the eccentricity grows. As the eccentricity of a satellite grows the rate of energy dissipation in the satellite grows, with the square of the orbital eccentricity. Dissipation of energy in a satellite tends to damp the eccentricity. As tidal torques push the system deeper into resonance, the eccentricity grows, until the rate of growth is balanced by the rate of decay due to the internal dissipation. At equilibrium, the eccentricity no longer changes and there is a steady state rate at which angular momentum is transferred to the outer satellite. The rate of angular momentum transfer is related to the rate of heating in the satellites. The equilibrium rate of heating can be calculated using conservation of energy and angular momentum (Lissauer et al., 1984).

The angular momentum L and energy E of a satellite of mass m in an Keplerian orbit of semimajor axis a about a primary of mass M are

$$L = m\sqrt{GMa(1-e^2)} \quad (2.1)$$

$$E = -GMm/(2a). \quad (2.2)$$

The rate of change of the Keplerian energy can be related to the applied torque. The energy can be written in terms of the angular momentum and eccentricity: $E = \tilde{E}(L, e)$. Let $n = \sqrt{GM/a^3}$; we have

$$\frac{\partial \tilde{E}}{\partial L} = \frac{n}{\sqrt{1-e^2}} \approx n, \quad (2.3)$$

ignoring corrections of order e^2 . The rate of change in angular momentum is the

torque

$$\frac{dL}{dt} = T. \quad (2.4)$$

Ignoring the change in energy due to the change in eccentricity, the rate of change in orbital energy from an applied satellite torque is

$$\frac{dE}{dt} = \frac{\partial \tilde{E}}{\partial L} \frac{dL}{dt} = \frac{nT}{\sqrt{1-e^2}} \approx nT, \quad (2.5)$$

again ignoring corrections of order e^2 .

Assume there are two satellites, and that there is some resonant interaction between the satellites so that angular momentum can be transferred between them.

For the sake of qualitative reasoning, let us ignore contributions to energy changes due to orbital eccentricities. Consider a small impulsive torque that causes a change in the angular momentum of the system ΔL . For simplicity assume that the torque is applied only to the inner satellite. The energy change due to this angular momentum change is approximately $\Delta E = n_0 \Delta L$. This is the energy input to the satellite system. Now let's take into account the exchange of angular momentum between the satellites. The change in angular momentum ΔL is now distributed in some way between the two satellites $\Delta L = \Delta L_0 + \Delta L_1$. The change in energy of the orbits is then $\Delta E = n_0 \Delta L_0 + n_1 \Delta L_1$. Because $n_1 < n_0$, this energy change is less than the energy gained by the satellites. The remaining energy goes into heating the satellites.

The energy input to the system is the sum of the energy inputs for the individual satellites. This presumes there is no cross tidal interaction between the satellites. So the total rate at which energy is transferred to the satellites from the rotation of the planet is $n_0 T_0 + n_1 T_1$, ignoring corrections of order e^2 . This energy changes the orbits and heats at least one of the satellites.

So we can write

$$n_0 T_0 + n_1 T_1 = \frac{d}{dt}(E_0 + E_1) + H, \quad (2.6)$$

where E_i are the Keplerian energies of the satellites, and H is the rate of heating. We have ignored the gravitational interaction energy of the satellites. If most of the

heating is in one satellite, we can take H to be the heating rate of that satellite.

As an eccentricity-type resonance is approached one of the satellite eccentricities grows. Near a $j : (j - 1)$ mean motion resonance, the eccentricity depends on a parameter $\delta = jn_1 + (1 - j)n_0$ that measures how close the system is to resonance. The condition of resonance equilibrium is that the rate of change of δ is zero. This implies

$$j \frac{dn_1}{dt} = (j - 1) \frac{dn_0}{dt}. \quad (2.7)$$

Close to resonance the parameter δ is small, so $jn_1 \approx (j - 1)n_0$. Dividing these, we find that

$$\frac{1}{n_0} \frac{dn_0}{dt} \approx \frac{1}{n_1} \frac{dn_1}{dt}, \quad (2.8)$$

which in turn implies

$$\frac{1}{a_0} \frac{da_0}{dt} \approx \frac{1}{a_1} \frac{da_1}{dt}. \quad (2.9)$$

Following Lissauer et al. (1984), let us assume that $T_0 \gg T_1$. Conservation of the angular momentum of the system requires

$$\frac{d}{dt}(L_0 + L_1) = T_0 + T_1 \approx T_0. \quad (2.10)$$

Using eq. (2.1) at small e , we find

$$\frac{1}{2} \frac{L_0}{a_0} \frac{da_0}{dt} + \frac{1}{2} \frac{L_1}{a_1} \frac{da_1}{dt} = T_0. \quad (2.11)$$

Using the equilibrium condition, eq. (2.9), we find

$$T_0 = \frac{1}{2a_0} \frac{da_0}{dt} (L_0 + L_1). \quad (2.12)$$

Using eq. (2.6), assuming $n_0 T_0 \gg n_1 T_1$, the rate of change in energy of the system is equal to

$$n_0 T_0 = \frac{d}{dt}(E_0 + E_1) + H. \quad (2.13)$$

Using this equation, eq. (2.12), and the equilibrium condition again, we derive

$$H = n_0 T_0 - \frac{T_0}{L_0 + L_1} \left(\frac{GMm_0}{a_0} + \frac{GMm_1}{a_1} \right). \quad (2.14)$$

Again ignoring corrections of order e^2 , we derive

$$H = n_0 T_0 \left(1 - \frac{1 + m_1 a_0 / (m_0 a_1)}{1 + (m_1 / m_0) \sqrt{a_1 / a_0}} \right). \quad (2.15)$$

Lissauer et al. (1984) generalize this formula to three satellites in equilibrium.

For the torque on each satellite we use the formula

$$T = \frac{3}{2} \frac{G m^2 R_S^5 k_{2S}}{a^6 Q_S}, \quad (2.16)$$

where k_{2S} and Q_S are the potential Love number and Q of Saturn, m is the mass of the satellite, R_S is the radius of Saturn, and a is the orbit semimajor axis (Schubert et al., 1986). For k_{2S} we use the value 0.341 (Gavrilov & Zharkov, 1977). The minimum Q_S for Saturn may be determined by the condition that Mimas be outside the synchronous orbit at the beginning of the solar system—this gives about $Q_S \geq 18,000$. A maximum can be placed on Q_S if we adopt the tidal origin of the Mimas-Tethys resonance. The age of the Mimas-Tethys resonance for a Q_S of 18,000 is 2×10^8 yrs (Sinclair, 1983). Placing the origin of the Mimas-Tethys resonance at the beginning of the solar system limits the Q_S of Saturn to be less than 4×10^5 .

The principal resonances that exist now or might have been operative in the recent past that involve Enceladus are: 2:1 Enceladus-Dione, 3:2 Mimas-Enceladus, 3:4 Enceladus-Tethys, and the 2:1 Janus-Enceladus resonances. For each of these we can calculate the equilibrium tidal heating given the torque on the inner body. This torque is tidal for all but Janus, for which it is a ring torque. Applying the equilibrium heating rate formula to each of these resonances we find, for $Q_S = 18,000$: 2.4 GW for the 2:1 Enceladus-Dione resonance, 0.71 GW for the 3:2 Mimas-Enceladus resonance, 1.2 GW for the 4:3 Enceladus-Tethys resonance, and 0.81 GW for the 2:1 Janus-Enceladus resonance. For the Janus-Enceladus resonance Lissauer et al. (1984)

found 4.5 GW, but they used the larger mass of Janus determined through Voyager observations. Peale (2003) found 0.95 GW using the pre-Cassini mass of Janus, 2.0×10^{18} kg, determined by Yoder et al. (1989). Keep in mind that Enceladus and Dione may not be in an equilibrium configuration (see below). Also, the assumption that one torque dominates is invalid.

If the torque to the innermost satellite does not dominate then the formula needs to be generalized. Beginning with eq. (2.6), we use the resonance condition, eq. (2.9), to get

$$H = \frac{n_0 T_0}{\sqrt{1-e_0^2}} + \frac{n_1 T_1}{\sqrt{1-e_1^2}} - \frac{T_0 + T_1}{L_0 + L_1} \left(\frac{GMm_0}{a_0} + \frac{GMm_1}{a_1} \right). \quad (2.17)$$

The formula readily generalizes to an equilibrium of three satellites, by adding an additional term to each of the sums. And this formula reduces to that of Lissauer et al. (1984) at small eccentricity if T_1 is set to zero.

Using this formula we recalculate the equilibrium heating rates for each of the resonances given above, assuming $Q_S = 18,000$. We find: 1.1 GW for the 2:1 Enceladus-Dione resonance, 0.48 GW for the 3:2 Mimas-Enceladus resonance, and 0.75 GW for the 2:1 Janus-Enceladus resonance. The implied heating of the Enceladus-Tethys resonance is negative; this resonance has no equilibrium as the orbits are diverging. Adding the torque on the outer satellite has reduced the heating for all resonances.

For the Enceladus-Dione and Mimas-Enceladus resonances these are upper limits to the heating rates because we have used the lower bound of 18,000 for the Q of Saturn. For larger Q_S , the torques and heating rates will be proportionally lower (see Figure 2-3).

The nonsolar radiated power from Enceladus is estimated to be 5.8 ± 1.9 GW (Spencer et al., 2006). This is larger than all the equilibrium heating rates.

2.3 Equilibrium Eccentricity

The equilibrium heating rate corresponds to an equilibrium eccentricity of Enceladus. We can derive the equilibrium eccentricity by requiring that the equilibrium heating rate be equal to the heating rate in a synchronously rotating satellite in an eccentric

orbit (Peale & Cassen, 1978; Peale, 2003):

$$H = \frac{21}{2} \frac{k_{2E}}{Q_E} \frac{GM_S^2 R_E^5 n}{a^6} e^2, \quad (2.18)$$

where k_{2E} and Q_E are the potential Love number and Q of Enceladus, and e is the eccentricity. Using eq. (2.16) and eq. (2.17), we find

$$e^2 = \frac{1}{7D} \left\{ 1 - \frac{1 + m_1 a_0 / (m_0 a_1)}{1 + (m_1 / m_0) \sqrt{a_1 / a_0}} + \left(\frac{m_1}{m_0} \right)^2 \left(\frac{a_0}{a_1} \right)^6 \left[\frac{n_1}{n_0} - \frac{1 + m_1 a_0 / (m_0 a_1)}{1 + (m_1 / m_0) \sqrt{a_1 / a_0}} \right] \right\}, \quad (2.19)$$

where D is a measure of the relative strength of tides in Enceladus versus tides in Saturn:

$$D = \frac{k_{2E}}{Q_E} \frac{Q_S}{k_{2S}} \left(\frac{M_S}{m_E} \right)^2 \left(\frac{R_E}{R_S} \right)^5. \quad (2.20)$$

Thus the equilibrium value of the eccentricity depends on the unknown k_{2E}/Q_E of Enceladus and the unknown Q_S . Note that if the torque on the outer body is negligible then the term with square brackets in Eq. (2.19) can be ignored, but for the satellites considered here this is not the case.

We can illustrate the approach to equilibrium and confirm the equilibrium value of the eccentricity by performing numerical integrations of the evolution of the system. Our model is an averaged resonance model that includes terms in the disturbing function up to order e^2 , with dissipative terms that affect both the semimajor axes and eccentricities. We have applied this model to study the evolution into the e_E -type 3:2 resonance between Mimas and Enceladus. For this resonance, Eq. (2.19) becomes $e^2 \approx (59.5D)^{-1}$. For $k_2 = 0.0018$, $Q_E = 100$, and $Q_S = 18,000$, the equilibrium eccentricity is calculated to be 0.022. The simulated evolution is shown in Figure 2-2. We see the eccentricity of Enceladus approach the predicted value.

For Enceladus and Dione in the current e_E -type 2:1 resonance, the equilibrium eccentricity is $e^2 \approx (30.69D)^{-1}$. The value of D depends upon the unknown k_2 and

Q of the satellite. Conventionally, Kelvin’s formula (Love, 1944) ,

$$k_2 = \frac{3/2}{1 + \frac{19\mu}{2\rho g R}}, \quad (2.21)$$

has been used to estimate Love numbers of small satellites, where μ is the rigidity, ρ the density, g the surface acceleration, and R the radius. For Enceladus, taking $\mu = 4 \times 10^9 \text{Nm}^{-2}$, we find $k_2 = 0.0018$. With an assumed Q_E of Enceladus of 20, the equilibrium eccentricity of Enceladus is 0.014. This is above the current eccentricity of 0.0047; so in this approximation, Enceladus is not in equilibrium and is still evolving deeper into resonance. Note that if the eccentricity is below the equilibrium eccentricity, and if the heat flow is steady, then the heating rate is lower than the equilibrium heating rate.

However, Ross & Schubert (1989) have shown that the dynamic Love number can be much larger than this conventional estimate. If the dynamic Love number is large enough then, in principle, Enceladus could be at a tidal equilibrium today. If Enceladus is at the equilibrium, then the estimates of the last section apply, and the heating in Enceladus is 1.1 GW for a $Q_S = 18,000$. If Q_S is larger than this then the heating is proportionally smaller. Thus even with an enhanced dynamic k_2 the equilibrium heating rate is lower than the observed heat flux.

For which parameter values is the current Enceladus-Dione system at equilibrium? Given the current eccentricity of 0.0047, and a value for Q_S , we can determine the required value of k_{2E}/Q_E for equilibrium. This is the solid curve shown in Figure 2-3. Above this curve, the current eccentricity is above the equilibrium value and below this curve it is below the equilibrium value. The horizontal line shows the k_{2E}/Q_E for Kelvin’s estimate of the Love number (calculated above) and for $Q_E = 20$. We see that for this value the current system is at an equilibrium for $Q_S = 159,000$. The equilibrium heating rate for the 2:1 Enceladus-Dione resonance as a function of Q_S is also shown in Figure 2-3.

Keep the “Mimas test” in mind. If k_{2E} is significantly enhanced over the Kelvin value because of the viscoelastic properties of ice, then one might expect this also to

be the case for Mimas.

2.4 Conclusion

The rate of heating of Enceladus in an equilibrium resonant configuration with other Saturnian satellites can be estimated independently of the physical properties of Enceladus. Our results update the values obtained for the equilibrium tidal heating found by Lissauer et al. (1984) and Peale (2003). We find that equilibrium tidal heating cannot account for the heat that is observed to be coming from Enceladus, and current heating rates are even less for conventional estimates of k_{2E} . Even allowing a dynamic k_{2E} much larger than the conventional k_{2E} , as can occur for viscoelastic models (Ross & Schubert, 1989), the equilibrium tidal heating is less than the heat observed to be coming from Enceladus.

One resolution is that the tidal equilibrium is unstable and that the system oscillates about equilibrium. Yoder & Peale (1981) suggested that Enceladus might oscillate about equilibrium if the Q of Enceladus is stress dependent. An alternate suggestion was made by Ojakangas & Stevenson (1986), who emphasized the possible temperature dependence of Q . In these models Enceladus would now be releasing heat stored during a recent high eccentricity phase. There may be other mechanisms to produce episodic behavior. For instance, perhaps Enceladus could just store the tidal heat as the system evolves monotonically and release it episodically. These mechanisms may be consistent with the episodic character of the resurfacing events as suggested by spacecraft images. But it is curious that one has to appeal to nonequilibrium tidal oscillations or episodic activity to heat both Io and Enceladus (Ojakangas & Stevenson, 1986). If the fraction of time spent in an active state is, say, of order 20%, for each satellite, then the probability that both are found in an active state today is only 4%.

Other low-order resonance configurations are possible for the Saturnian satellites in the past. These include the 3:2 Mimas-Enceladus and the 3:4 Enceladus-Tethys resonances. The latter resonance has no equilibrium because the orbits are diverging,

and the former has an equilibrium heating of only 0.48 GW. So equilibrium heating at past resonances is no more successful at explaining past resurfacing events than equilibrium heating is at explaining the present activity.

Enceladus remains a puzzle.

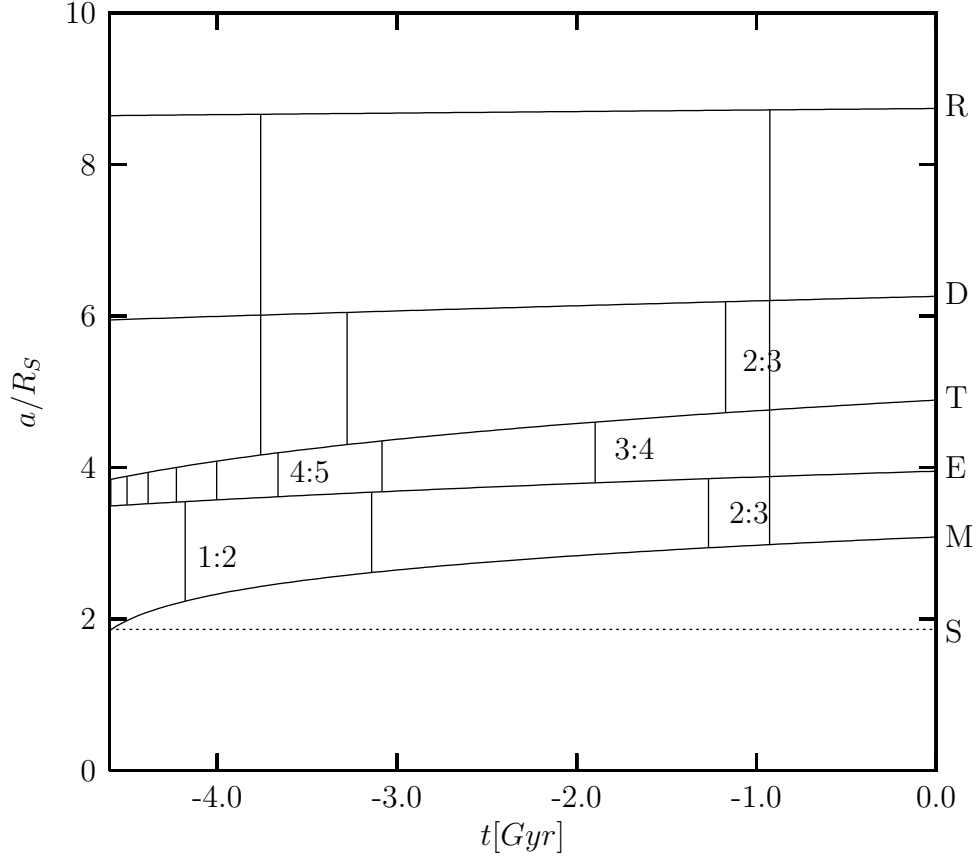


Figure 2-1: The approximate locations of the first-order resonances among the Saturnian satellites are shown for $Q_S = 18,000$. The shift of position of the resonances due to Saturn's oblateness has been ignored. Also shown are the tidally evolved orbits as a function of time. The dotted line shows the synchronous radius. The minimum Q_S is determined by placing Mimas at the synchronous radius at the beginning of the solar system. The current 2:1 and 4:2 resonances between Enceladus-Dione and Mimas-Tethys are not shown.

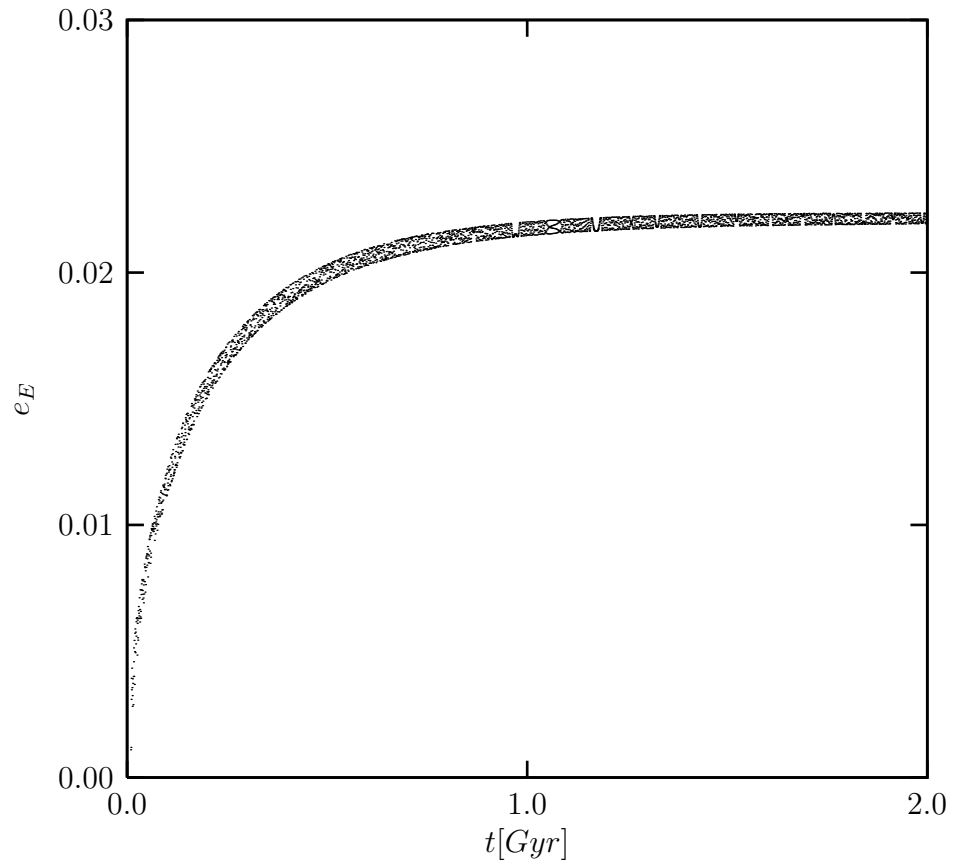


Figure 2-2: The eccentricity of Enceladus approaches an equilibrium value as the system evolves into the e -Enceladus 3:2 Mimas-Enceladus resonance.

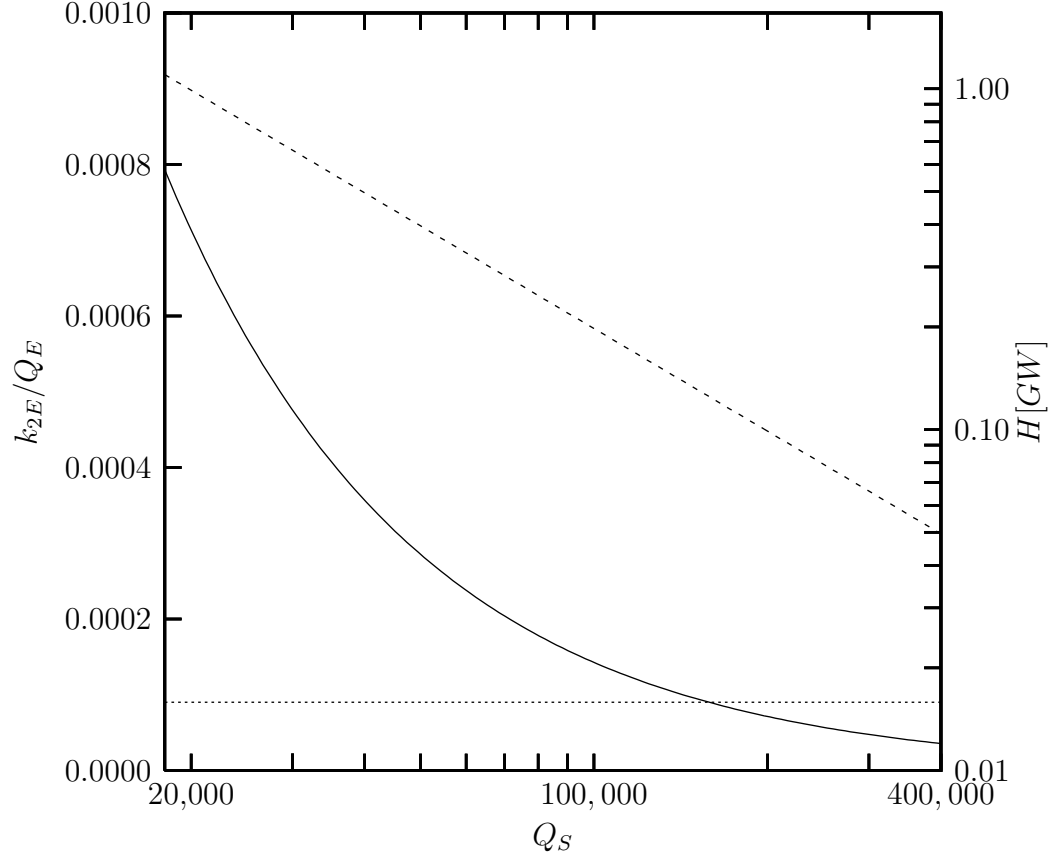


Figure 2-3: The solid line shows the k_{2E}/Q_E for which the current configuration of Enceladus (with eccentricity 0.0047) and Dione is a tidal equilibrium for the given value of Q_S . The dotted line shows the value of k_{2E}/Q_E using Kelvin's formula for the Love number, using a rigidity of $4 \times 10^9 \text{N/m}^2$, and a Q of 20. The dashed line gives the equilibrium heating rate H in Enceladus as a function of Q_S .

Chapter 3

Tidal evolution of Mimas, Enceladus, and Dione

The tidal evolution through several resonances involving Mimas, Enceladus, and/or Dione is studied numerically with an averaged resonance model. We find that, in the Enceladus-Dione 2:1 e -Enceladus type resonance, Enceladus evolves chaotically in the future for some values of k_2/Q . Past evolution of the system is marked by temporary capture into the Enceladus-Dione 4:2 ee' -mixed resonance. We find that the free libration of the Enceladus-Dione 2:1 e -Enceladus resonance angle of 0.5° can be explained by a recent passage of the system through a secondary resonance. In simulations with passage through the secondary resonance, the system enters the current Enceladus-Dione resonance close to tidal equilibrium and thus the equilibrium value of tidal heating of $1.1(18,000/Q_S)$ GW applies.

We find that the current anomalously large eccentricity of Mimas can be explained by passage through several past resonances. In all cases, escape from the resonance occurs by unstable growth of the libration angle, sometimes with the help of a secondary resonance. Explanation of the current eccentricity of Mimas by evolution through these resonances implies that the Q of Saturn is below 100,000. Though the eccentricity of Enceladus can be excited to moderate values by capture in the Mimas-Enceladus 3:2 e -Enceladus resonance, the libration amplitude damps and the system does not escape. Thus past occupancy of this resonance and consequent tidal heating

of Enceladus is excluded. The construction of a coherent history places constraints on the allowed values of k_2/Q for the satellites.

3.1 Introduction

Enceladus poses a problem. Cassini observed active plumes emanating from Enceladus (Porco et al., 2006). The heat emanating from the south polar terrain is estimated to be 17.0 ± 3.3 GW (Howett et al., 2010), increased from 5.8 ± 1.9 GW (Spencer et al., 2006). Radiogenic heating is estimated to account for only 0.32 GW (Porco et al., 2006). The secondary spin-orbit model (Wisdom, 2004) could account for the heating, but the system was not found to be librating (Porco et al., 2006). The only remaining source of heating is tidal heating. Tidal heating in an equilibrium configuration, one in which the eccentricities no longer change as the semimajor axes continue to tidally evolve, can be estimated independent of satellite physical properties using conservation of angular momentum and energy. Equilibrium tidal heating can account for at most $1.1(18000/Q_S)$ GW of heating in Enceladus, where Q_S is the Q of Saturn (Meyer & Wisdom, 2007).

One possibility for higher heat flow is that Enceladus is oscillating about the tidal equilibrium (Ojakangas & Stevenson, 1986). However, Meyer & Wisdom (2008a) have shown that for the physical parameters of Enceladus, the Ojakangas and Stevenson model does not oscillate. Another possibility is that the resonance is dynamically unstable. If the system exhibited a, perhaps temporary, episode of chaotic variations in the eccentricity then the heating rate could exceed the equilibrium heating rate. We have therefore undertaken a systematic exploration of the dynamics of the Saturnian satellite system, focusing on the evolution of Enceladus. In particular, we study the evolution of Enceladus and Dione in the current 2:1 e -Enceladus type mean motion resonance. We also study the evolution of Mimas and Enceladus through the several 3:2 mean motion resonances.

Though our study was primarily motivated by Enceladus, the free eccentricity of 0.02 of Mimas also poses a problem. If primordial, it should have damped in the age

of the solar system. What excited it? To address this problem we have extended our study to include the Mimas-Dione 3:1 multiplet of resonances.

3.2 Model

Our model is an averaged resonance model for a mean-motion commensurability between two coplanar satellites. We include all terms, both resonant and secular, in the disturbing function up to second order in the eccentricities of both satellites. We also model the oblateness of the planet, including J_2 , J_4 and J_2^2 contributions. We include tidal evolution of the orbits and tidal damping of the eccentricities. The physical parameters, such as the Q s of Saturn and the satellites, are all assumed to be constant in time. Details of the model are presented in Appendix A. We use the Bulirsch-Stoer algorithm to integrate the differential equations (Bulirsch & Stoer, 1966).

3.3 Equilibrium Eccentricity

As a satellite system tidally evolves regularly into resonance, the eccentricity of one (or both) of the satellites grows because of the resonance interaction. As the eccentricity grows the dissipation grows with the square of the orbital eccentricity. Dissipation within a satellite tends to damp the orbital eccentricity. An equilibrium is possible: the satellites evolve deeper into the resonance, until the increase of eccentricity due to the evolution deeper into the resonance is balanced by the decrease of eccentricity due to internal dissipation.

When only the eccentricity of the interior satellite is excited the equilibrium eccentricity can be calculated (Meyer & Wisdom, 2007):

$$e_0^2 = \frac{1}{7D_0} \left\{ 1 - \frac{1 + m_1 a_0 / (m_0 a_1)}{1 + (m_1 / m_0) \sqrt{a_1 / a_0}} + \left(\frac{m_1}{m_0} \right)^2 \left(\frac{a_0}{a_1} \right)^6 \left[\frac{n_1}{n_0} - \frac{1 + m_1 a_0 / (m_0 a_1)}{1 + (m_1 / m_0) \sqrt{a_1 / a_0}} \right] \right\}, \quad (3.1)$$

where a_i , m_i , and n_i are the semimajor axes, the masses, and the mean motions of

the satellites (0 for interior, 1 for exterior), and where D_0 is a measure of the relative strength of tides in the interior satellite versus tides in Saturn:

$$D_0 = \frac{k_{2,0}}{Q_0} \frac{Q_S}{k_{2S}} \left(\frac{M_S}{m_0} \right)^2 \left(\frac{R_0}{R_S} \right)^5. \quad (3.2)$$

Here $k_{2,0}$ and k_{2S} are the Love numbers, Q_0 and Q_S are the tidal dissipation factors, m_0 and M_S are the masses, and R_0 and R_S are the radii, of the interior satellite and Saturn, respectively. When only the eccentricity of the exterior satellite is excited then the equilibrium eccentricity is given by the same formula with the 0s and 1s interchanged.

As the equilibrium eccentricity is approached, the amplitude of libration in the resonance can either decrease or increase. It is either stable or unstable. In the case of Io in the Io-Europa 2:1 e -Io resonance, the libration amplitude damps and the equilibrium resonance configuration is stable. In the case of the evection resonance in the evolution of the Earth-Moon system, the libration amplitude grows as the equilibrium eccentricity is approached (Touma & Wisdom, 1998). This allows a natural escape from the resonance with an eccentricity near the equilibrium eccentricity. In our studies of the evolution of Mimas, Enceladus, and Dione, we found that sometimes the amplitude of libration damped and sometimes it grew, depending on the resonance and the physical parameters. Sometimes, as mentioned below, the escape from resonance is assisted by temporary capture into a secondary resonance, as occurred for Miranda (Tittlemore & Wisdom, 1989).

After escape from resonance, the eccentricity decays with the timescale (Squyres et al., 1983)

$$\tau = \frac{2ma^5}{21nMR^5} \frac{Q}{k_2}, \quad (3.3)$$

where m is the satellite mass, a is the semimajor axis, n the mean motion, M the planet mass, R the satellite radius, Q the dissipation factor, and k_2 the satellite potential Love number. Note that the k_2/Q for the satellite affects both the equilibrium eccentricity (through the factor D_0) and the timescale for eccentricity damping.

3.4 Enceladus-Dione 2:1 *e*-Enceladus Resonance— Future

Enceladus and Dione are currently in the Enceladus-Dione 2:1 *e*-Enceladus resonance.¹ Enceladus has a forced eccentricity of about 0.0047. The system has a free libration of about 1.5° (Sinclair, 1972). We decided to explore the future evolution of the system, with the primary goal of verifying the analytic predictions of the equilibrium eccentricity for various parameters. To our surprise, we found that the system exhibits complicated, sometimes (apparently) chaotic behavior.

The behavior we found depends on the assumed k_2/Q of Enceladus, which is unknown. So we made a systematic survey varying this parameter. We explored the range of k_2/Q between 1.8×10^{-5} to 9.4×10^{-4} . The lower bound corresponds to a Kelvin² $k_2 = 0.0018$ with a Q of 100. The upper bound corresponds roughly to a k_2 that is 10 times the Kelvin value with a Q of 20.

For $1.8 \times 10^{-5} < k_2/Q < 7.8 \times 10^{-5}$ the system tends toward the expected equilibrium, but as the eccentricity approaches the equilibrium eccentricity the libration amplitude increases. Eventually, the system escapes the resonance whereupon the eccentricity decays.

For $7.8 \times 10^{-5} < k_2/Q < 9.4 \times 10^{-5}$, the system exhibits an unexpected and interesting behavior. As in the previous case, the system tends toward equilibrium while the libration amplitude increases. Then the system enters a phase with large chaotic variations in the eccentricity while the resonance angle alternates between circulation and libration. Eventually the system escapes resonance and the eccentricity decays. After the system leaves the resonance the libration angle decays toward π .

¹The resonant argument of the Enceladus-Dione 2:1 *e*-Enceladus resonance is $\lambda_E - 2\lambda_D + \varpi_E$, where λ_E and λ_D are the mean longitudes of Enceladus and Dione, and ϖ_E is the longitude of pericenter of Enceladus. For this resonance the eccentricity of Enceladus is excited.

²That is, using Kelvin's formula

$$k_2 = \frac{3/2}{1 + 19\mu/(2\rho gR)}$$

for the Love number of a homogeneous satellite of density ρ , radius R , surface gravity g , and rigidity μ . We chose $\mu = 4 \times 10^9 \text{ N m}^{-2}$.

An example of this behavior is shown in Figure 3-1.

For $9.4 \times 10^{-5} < k_2/Q < 1.76 \times 10^{-4}$, the system exhibits similar chaotic behavior to systems in the previous range of k_2/Q values, but the system ultimately does not escape the resonance. It settles into a finite amplitude librational equilibrium about the equilibrium eccentricity, as shown in Figures 3-2 to 3-4. For larger values of k_2/Q , the chaotic phase is more brief. The fact that the evolution of the system settles on a limit cycle is interesting. We are unaware of other examples in which the endpoint of tidal evolution is a limit cycle.

For $1.76 \times 10^{-4} < k_2/Q < 2.80 \times 10^{-4}$, the chaotic phase disappears, leaving a system that grows into stable finite amplitude libration about the equilibrium eccentricity.

For $k_2/Q > 2.80 \times 10^{-4}$, the eccentricity reaches a stable equilibrium and the libration amplitude damps to zero, as shown in Figure 3-5. This behavior was observed up to $k_2/Q = 9.4 \times 10^{-4}$, but presumably extends beyond the studied range.

We have seen that a diverse range of behavior is possible for the future of the Enceladus-Dione resonance, depending on the unknown k_2/Q . In some of these scenarios, Enceladus has an exciting future.

3.5 Mimas-Enceladus 3:2 *e*-Enceladus Resonance

One possible mechanism for heating Enceladus beyond the equilibrium limit is for Enceladus to evolve chaotically. The Enceladus-Dione 2:1 resonance exhibited such behavior in the future. The most recent first-order resonance that the system has passed through is the Mimas-Enceladus 3:2 *e*-Enceladus resonance, which was exited 1.16 Gyr ago (for a minimum Q_S of 18,000).³ So we explored this resonance for similar chaotic behavior. However, we found regular evolution into equilibrium, with no excursions above equilibrium, chaotic or otherwise.

We examined the system for a range of k_2/Q of Enceladus of 6.0×10^{-6} to 9.4×10^{-4} .

³Using a constant Q_S model, Mimas would be at the synchronous radius at the beginning of the solar system for approximately $Q_S = 18,000$ (Meyer & Wisdom, 2007).

In order to assure capture into the e -Enceladus resonance,⁴ we chose semimajor axes corresponding to a location just before the resonance and set the eccentricity of Enceladus to be 0.0011 so the capture probability was high. In every case, the system was captured into the e -Enceladus resonance and reached equilibrium. The libration amplitude damped. No escape or chaotic behavior was observed. We conclude that Enceladus was not captured into this resonance because we found no natural mechanism for escape.

3.6 Mimas-Enceladus 6:4 ee' Resonance

The eccentricity of Mimas is relatively high (0.020) and has a short timescale for tidal decay. For a Q of 100 and a Kelvin k_2 of 0.00058, the timescale for decay of eccentricity is about 325 Myr. Thus, either the eccentricity of Mimas started at a much higher value, perhaps with a larger Q , or the eccentricity has been recently excited. The most recent first-order commensurability involving the eccentricity of Mimas is the Mimas-Enceladus 3:2 mean-motion commensurability.

One of the resonances at the 3:2 mean-motion commensurability is the Mimas-Enceladus 6:4 ee' mixed resonance, which was exited 1.15 Gyr ago (for Q_S of 18,000).⁵ We examined evolution through this resonance as a possible explanation for Mimas's free eccentricity. We succeeded in explaining the current free eccentricity if Mimas's k_2/Q is 1.3×10^{-6} . The evolution of the eccentricities of Mimas and Enceladus is shown in Figure 3-6.

The time of exit from the resonance depends upon the Q of Saturn, which is here taken to be the minimum $Q_S = 18,000$. For larger Q_S the required k_2/Q of Mimas would be smaller.

⁴The resonant argument of the Mimas-Enceladus 3:2 e -Enceladus resonance is $2\lambda_M - 3\lambda_E + \varpi_E$. For this resonance the eccentricity of Enceladus is excited.

⁵The resonant argument of the Mimas-Enceladus 6:4 ee' -mixed resonance is $4\lambda_M - 6\lambda_E + \varpi_M + \varpi_E$. For this resonance the eccentricities of both Mimas and Enceladus are excited.

3.7 Mimas-Enceladus 3:2 *e*-Mimas Resonance

Another of the multiplet of resonances at this mean-motion commensurability is the Mimas-Enceladus 3:2 *e*-Mimas resonance,⁶ which was exited 1.14 Gyr ago (for a minimum Q of Saturn of $Q_S = 18,000$).

We also examined evolution through this resonance to see whether Mimas's eccentricity can be explained. We found that Mimas's eccentricity could be explained and that there exists an intrinsic dynamical mechanism of escape from the resonance. In particular, the libration amplitude grows until the amplitude of the libration reaches π whereupon the system falls out of resonance.

For a k_2/Q of 1.42×10^{-6} for Mimas, Figure 3-7 shows the evolution of eccentricity toward an equilibrium value of 0.052, followed by a period in which the variations of the eccentricity grow larger, and then as the system escapes from the resonance the eccentricity decays to the present value at the current time. This particular k_2/Q was chosen so that Mimas's eccentricity would damp to the current value at the present from the equilibrium eccentricity at the time at which the system left the resonance. This exit time depends upon the Q of Saturn, which is here taken to be the minimum $Q_S = 18,000$. For larger Q_S the required k_2/Q of Mimas would be smaller.

Figure 3-8 shows the resonance angle for this resonance. The libration amplitude shows a sudden increase as the system is caught in a 3-fold secondary resonance, between the libration frequency and the frequency of circulation of σ_1 . This is similar to the mechanism that took Miranda out of resonance at an inclination near 4° (Tittlemore & Wisdom, 1989).

Mimas's eccentricity can be explained either by passage through the 3:2 *e*-Mimas resonance, or the 6:4 *ee'* mixed resonance. Placing these resonances at the birth of the solar system limits the time-averaged Q of Saturn to be below 70,000.⁷

⁶The resonant argument of the Mimas-Enceladus 3:2 *e*-Mimas resonance is $2\lambda_M - 3\lambda_E + \varpi_M$. For this resonance the eccentricity of Mimas is excited.

⁷ Q_S may be non-constant—our calculations place limits on only the integrated evolution.

3.8 Mimas-Dione 3:1 Resonance

As discussed in the following section on the past evolution into the Enceladus-Dione 2:1 resonance, the eccentricity of Dione is required to exceed 0.001 at the time the system encounters the Enceladus-Dione 2:1 e -Dione resonance. The most likely mechanism for exciting the eccentricity of Dione is temporary capture into the Mimas-Dione 3:1 ee' -mixed resonance. In addition, capture into this resonance is another possible explanation for the current free eccentricity of Mimas. Passage through this resonance occurred 0.75 Gyr ago, for a Q_S of 18,000, after passage through the Mimas-Enceladus 3:2 resonance.

Another possible explanation of Mimas's free eccentricity is the Mimas-Dione 3:1 e^2 -Mimas resonance, which occurred 0.70 Gyr ago, for a Q_S of 18,000. Evolution of Mimas's eccentricity is shown in Figure 3-9. In this resonance, the eccentricity of Dione is not excited. The former explanation of the eccentricity of Mimas is preferred because it also excites the eccentricity of Dione.

Explaining Mimas's eccentricity via either of these resonances places an upper limit on the Q of Saturn of 100,000 (placing this resonance at the birth of the solar system). To reach the current eccentricity of Mimas at the present time requires a k_2/Q of Mimas of 3.0×10^{-6} in the e^2 -Mimas resonance or a k_2/Q of Mimas of 2.6×10^{-6} in the ee' -mixed resonance.

3.9 Enceladus-Dione 2:1 e -Enceladus Resonance— Past

For an isolated first order e -type resonance, the tidal evolution into the resonance is simple. But when more than one resonance is present, the evolution can be more complicated, even though the multiplet of resonances associated with a commensurability are split due to the oblateness of the planet. The evolution of Enceladus and Dione through the multiplet of resonances associated with the 2:1 commensurability has been the subject of some discussion (Sinclair, 1983, Peale, 1986). Here we study

the evolution numerically.

We have carried out an extensive survey of the evolution of the system through the multiplet of eccentricity-type resonances associated with the 2:1 commensurability between Enceladus and Dione. We found that the evolution of the system was more complicated than expected. In particular, we found that it was rather difficult for the system to pass through the other resonances of the multiplet before being finally captured in the current resonance. The third-order Enceladus-Dione 6:3 $ee'e'$ mixed resonance⁸ is surprisingly important in the evolution. Also important is the Enceladus-Dione 4:2 ee' mixed resonance.⁹

In our simulations the system was initially captured by the Enceladus-Dione 2:1 e -Enceladus resonance, before any of the other resonances of the multiplet were encountered. As the system subsequently passed through the Enceladus-Dione e -Dione resonance, it was occasionally captured. However, once captured, the libration amplitude damps and precludes a natural escape from the resonance; we conclude that the system was not captured into this resonance. The next resonance encountered (in our model) is the third order $ee'e'$ resonance. We found that the system was easily captured into this resonance, and that once captured the system had no natural mechanism for escape. In rare cases, when the eccentricity of Dione was near the critical value for certain capture, the system did escape this resonance by unstable growth of the libration amplitude. But it is likely that this resonance was avoided by the actual system. We found that in order to avoid capture into this resonance the eccentricity of Dione had to exceed about 0.001 at the time of e -Dione resonance encounter. (For one mechanism to explain this eccentricity, see above.) We also found that successful passage through the third order resonance required that k_2/Q of Dione be in certain ranges, depending on the eccentricity of Dione at the time of the e -Dione resonance encounter. For $e_D = 0.001$, we found k_2/Q needs to be smaller than about 1.4×10^{-5} . For $e_D = 0.003$, we found that k_2/Q for Dione needs to be less than 8.8×10^{-5} .

Once the system avoids the third order resonance, then in our simulations it is

⁸The resonant argument of the Enceladus-Dione 6:3 $ee'e'$ mixed resonance is $3\lambda_E - 6\lambda_D + \varpi_E + 2\varpi_D$.

⁹The resonant argument of the Enceladus-Dione 4:2 ee' mixed resonance is $2\lambda_E - 4\lambda_D + \varpi_E + \varpi_D$.

almost always captured by the ee' mixed resonance (in only one case out of hundreds the system passed through the mixed resonance without being captured). However, unlike the third-order resonance, in this resonance the libration amplitude is always unstable and the system naturally escapes. As it escapes we found that it falls directly into the e -Enceladus resonance.

As the system falls into the e -Enceladus resonance the system exhibits all the behavior catalogued in section 4. But the limiting behavior happens right away; the system does not fall out of the resonance with an eccentricity much below the equilibrium value. In a survey of the possible behavior as a function of the k_2/Q for Enceladus, we only found a behavior consistent with the current state of the system if k_2/Q was at or just below the equilibrium value of k_2/Q .¹⁰ The equilibrium value is 8×10^{-4} ; we found values as low as 4.8×10^{-4} also passed through the current state of the system. But usually, we found the system escaped near the equilibrium value for a given k_2/Q . These results suggest that k_2/Q for Enceladus is closer to the equilibrium value than the Kelvin value (even with a Q as low as 20). For values of k_2/Q near the equilibrium value, the libration amplitude damps in a few tens of millions of years once it enters the e -Enceladus resonance. Since the eccentricity of Dione needs to decay to its current value, this rapid decay of the libration amplitude may be inconsistent with the current state of the system.

However, we found that once the system is in the e -Enceladus resonance, it is often temporarily captured in a 2:1 secondary resonance between the libration frequency and the frequency of circulation of the e -Dione resonance angle (σ_1).¹¹ The system escapes the secondary resonance by unstable growth of the secondary resonance libration angle. Once out of the secondary resonance, the libration amplitude in the e -Enceladus resonance damps. The current libration amplitude is probably evidence that the system has recently passed through this secondary resonance. This allows time for the eccentricity of Dione to damp to its current value.

¹⁰By “equilibrium value” of k_2/Q we mean the value such that the current state of the system is at a tidal equilibrium, that is, the eccentricity is no longer changing. See Meyer & Wisdom (2007).

¹¹After this work was nearly complete we learned of the work of Callegari & Yokoyama (2007), who noted the existence of secondary resonances in this system.

The evolution of the eccentricities of Enceladus and Dione as the system evolves through the Enceladus-Dione 2:1 multiplet of resonances are shown in Figures 3-10 and 3-11, respectively. In this simulation, the k_2/Q of Enceladus is 8.0×10^{-4} , the value for which the current eccentricity is the equilibrium eccentricity. The k_2/Q of Dione is 1.24×10^{-4} . The event marked ‘a’ shows passage through the e -Dione resonance. Event ‘b’ is capture into the ee' -mixed resonance. Escape from the ee' -mixed resonance (‘c’) is quickly followed by capture into the 2:1 secondary resonance (‘d’).

3.10 Discussion

The values of k_2/Q for the satellites in the above sections were calculated for a minimum Q_S of 18,000. For a maximum Q_S that places the resonances at the beginning of the solar system, the values of k_2/Q are smaller. We can estimate the required values of k_2/Q by assuming that the eccentricity upon exiting the resonance is approximately the equilibrium eccentricity. We then constrain k_2/Q for each satellite by the requirement that the eccentricity decay to the present value at the present time. Figure 3-12 shows the values of k_2/Q , determined in this way, for Mimas as a function of Q_S , for the Mimas-Enceladus 3:2 e -Mimas resonance and for the Mimas-Dione 3:1 e^2 -Mimas resonance.

We see that, as expected, a larger Q_S requires a smaller k_2/Q for Mimas. Basically, this is because the time since exiting the resonance is longer for a larger Q_S and to slow the decay of the eccentricity k_2/Q must be smaller. The k_2/Q for Mimas in the Mimas-Enceladus 3:2 resonance is smaller than that in the Mimas-Dione 3:1 resonance. The 3:1 resonance occurs closer to the present time, so the eccentricity must damp more quickly, and also the 3:1 equilibrium eccentricity is larger than the 3:2 equilibrium eccentricity.

The interpretation of these values of k_2/Q depends on the assumed rigidity through the Love number k_2 . The rigidity of ice (and rock) at the conditions of Mimas is uncertain. In computing the Kelvin value of the Love number presented above, we

used a rigidity of $4 \times 10^9 \text{ N m}^{-2}$. With this rigidity, the Kelvin k_2 of Mimas is 5.8×10^{-4} . Thus the required Q of Mimas for the free eccentricity of Mimas to be explained by passage through the Mimas-Dione 3:1 e^2 -Mimas resonance ranges from about 190 (for Q_S of 18,000) to about 1000 (for $Q_S = 100,000$). The required Q for Mimas for the Mimas-Dione 3:1 ee' -mixed resonance ranges from about 220 (for Q_S of 18,000) to about 1050 (for Q_S of 100,000). The required Q for Mimas for the Mimas-Enceladus 3:2 resonance ranges from about 420 (for Q_S of 18,000) to about 1600 (for Q_S of 70,000). But these values of Q are uncertain because of uncertainties in the Love number. First, the rigidity assumed may be uncertain by up to a factor of 3 in both directions (Moore, 2004). Then there may be viscoelastic modification of the “dynamic” Love number (Ross & Schubert, 1989). With these uncertainties, the required values of Q should not be taken too literally. Nevertheless, some may be uncomfortable with the large Q of Mimas required at the larger Q_S end of the allowed range. This might suggest that Q_S is closer to 18,000 than 100,000.

3.11 Conclusion

We have numerically explored tidal evolution through several resonances, including the multiplets of the Enceladus-Dione 2:1 resonance, the Mimas-Enceladus 3:2 resonance, and the Mimas-Dione 3:1 resonance.

Enceladus may have an interesting future in the Enceladus-Dione 2:1 e -Enceladus resonance. For a range of k_2/Q , we found that the system exhibits complicated and sometimes chaotic behavior. Unfortunately, we only found this interesting behavior in the future. Therefore, such chaotic episodes cannot explain the current heating of Enceladus.

We then investigated the past Mimas-Enceladus 3:2 e -Enceladus resonance to see if similar chaotic episodes occurred. We found no chaotic behavior and moreover, no natural dynamical mechanism for escape. If the system had been captured in this resonance, it would have remained in the resonance until the present time, contrary to its observed state.

We found multiple possible explanations for the large free eccentricity of Mimas. The Mimas-Enceladus 6:4 ee' mixed resonance can explain Mimas's current free eccentricity of 0.020 for a k_2/Q of Mimas of about 1.3×10^{-6} . Escape from this resonance is by growth of the libration amplitude.

In addition, the Mimas-Enceladus 3:2 e -Mimas resonance can excite Mimas's eccentricity to large values, and for a k_2/Q of about 1.42×10^{-6} , the eccentricity can decay from values near the equilibrium value of 0.052 to the current value in the 1.14 Gyr since the resonance was exited (for $Q_S = 18,000$). The system escapes as the libration amplitude grows to π , sometimes with the help of temporary capture in a secondary resonance.

If Mimas's eccentricity is explained by either of the above mechanisms, the time-averaged Q of Saturn is constrained to be less than 70,000 so that the Mimas-Enceladus 3:2 resonance multiplet occurs after the birth of the solar system.

Mimas's eccentricity could also be explained via excitation in the Mimas-Dione 3:1 e^2 -Mimas resonance for a k_2/Q of Mimas of 3.0×10^{-6} or the Mimas-Dione 3:1 ee' -mixed resonance for a k_2/Q of Mimas of 2.6×10^{-6} . In these cases, the time-averaged Q of Saturn is constrained to be less than 100,000.

Of the Mimas-Enceladus 6:4 ee' mixed resonance, the Mimas-Enceladus 3:2 e -Mimas resonance, the Mimas-Dione 3:1 e^2 -Mimas resonance, and the Mimas-Dione 3:1 ee' -mixed resonance, the Mimas-Enceladus 6:4 ee' mixed resonance is encountered first as Mimas tidally evolves. If it is captured then the eccentricity of Mimas will be large after escape, so subsequent capture into the Mimas-Enceladus 3:2 e -Mimas resonance will be unlikely (we estimate 1.4% using the formulae of Borderies and Goldreich, 1984). If the eccentricity decays sufficiently, then there is a chance that the system will be subsequently captured into the Mimas-Dione 3:1 e^2 -Mimas resonance or the Mimas-Dione 3:1 ee' -mixed resonance. For a maximum k_2/Q for Mimas of 3×10^{-6} we estimate the probability of this capture in the 3:1 resonance at 4.5%. Alternatively, the system may pass through the Mimas-Enceladus 6:4 ee' mixed resonance, and be captured into the Mimas-Enceladus 3:2 e -Mimas resonance. After escape, the system again has a small chance of being captured by one of the

Mimas-Dione 3:1 resonances. Capture into the Mimas-Dione 3:1 ee' -mixed resonance is preferred because the scenario requires lower (perhaps more realistic) Q of Mimas and also excites the eccentricity of Dione to the level required for successful passage through the Enceladus-Dione 2:1 multiplet.

The evolution into the current Enceladus-Dione 2:1 e -Enceladus resonance is surprisingly complicated. The system is first captured into the e -Enceladus resonance, well before the point of exact commensurability. Subsequent evolution is marked by passage through or past the e -Dione, $ee'e'$, and ee' -mixed resonances. In order to successfully arrive at the current state of the system, the e -Dione and $ee'e'$ resonances must be avoided because once captured, escape is unlikely. In our simulations, we found that this requires that the eccentricity of Dione must exceed 0.001 when it encounters the e -Dione resonance. A likely mechanism for exciting the eccentricity of Dione is capture into the Mimas-Dione 3:1 ee' -mixed resonance.

Once the system has passed the e -Dione and $ee'e'$ -mixed resonances, the system is usually captured into the Enceladus-Dione 2:1 ee' -mixed resonance and this phase of the evolution shows large variations in the eccentricity of Enceladus. However, these variations are unfortunately not large enough to substantially enhance the heating rate over the equilibrium rate. The system naturally escapes the ee' -mixed resonance by growth of the libration amplitude, and then is immediately captured back into the e -Enceladus resonance.

After leaving the ee' -mixed resonance, the system usually is caught in a 2:1 secondary resonance between the libration frequency in the e -Enceladus resonance and the circulation frequency of the e -Dione resonance angle. This secondary resonance temporarily increases the libration amplitude of the e -Enceladus resonance angle. In some of our simulations, the e -Enceladus libration amplitude damped to the current observed value of 1.5° as the eccentricity of Dione damped to its observed value of 0.0022.

Since the system always escapes this secondary resonance close to equilibrium, we are able to conclude that Enceladus is probably near its equilibrium eccentricity. Therefore the equilibrium heating rate of $1.1(18,000/Q_S)$ GW (Meyer & Wisdom,

2007) due to the Enceladus-Dione 2:1 *e*-Enceladus resonance applies. To exceed this rate of heating requires some other form of non-equilibrium behavior.

3.12 Acknowledgements

Some of the numerical simulations for this research were performed on Caltech's Division of Geological and Planetary Sciences Dell cluster. This research was supported in part by the NASA Planetary Geology and Geophysics Program.

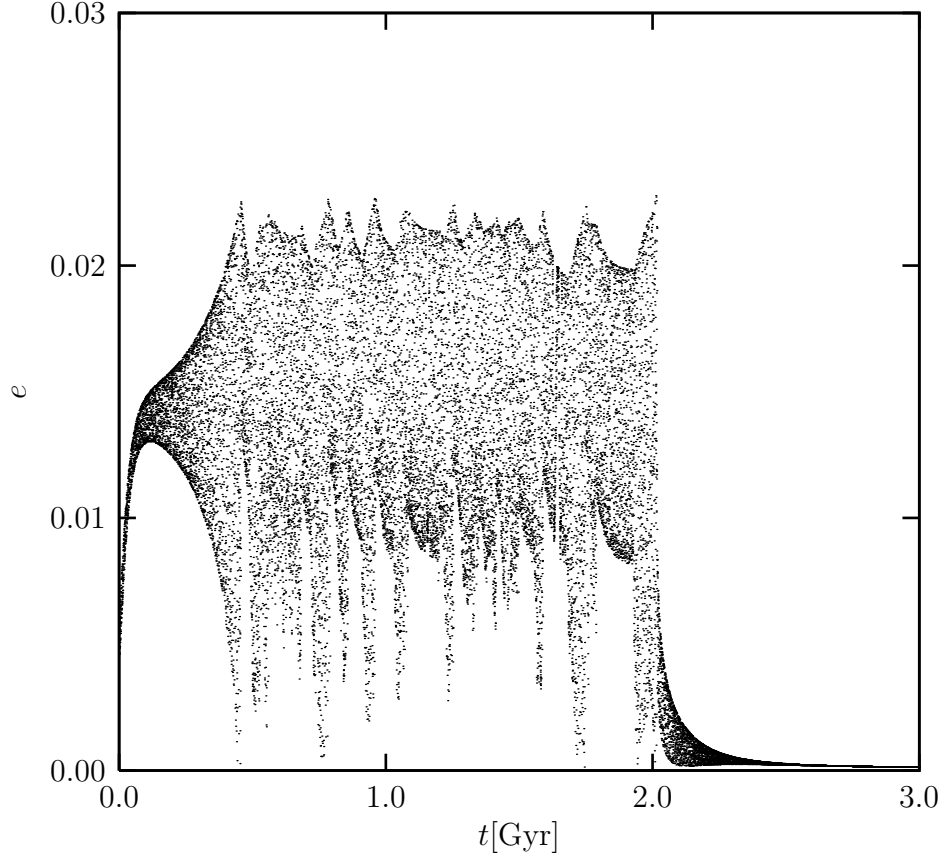


Figure 3-1: The future evolution of Enceladus's eccentricity as it evolves deeper into the Enceladus-Dione 2:1 e -Enceladus resonance. The system approaches equilibrium, but the libration amplitude is unstable and the eccentricity enters a chaotic phase with large variations in amplitude. Eventually the system falls out of resonance. Here k_2/Q of Enceladus is 8.6×10^{-5} .

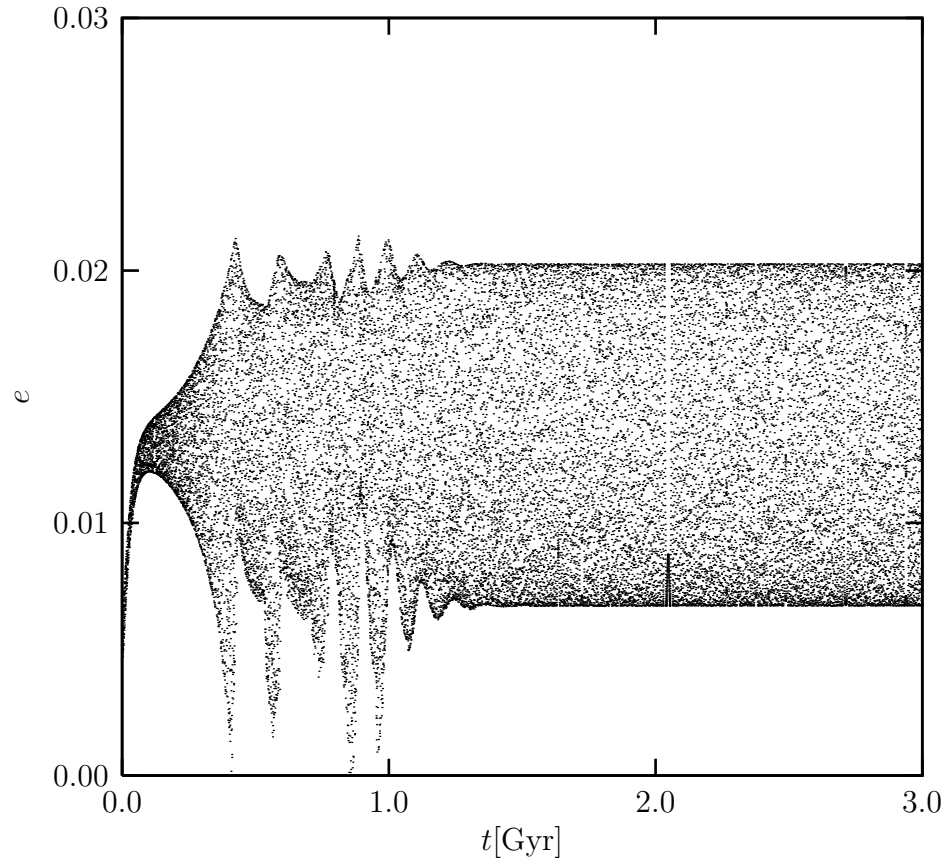


Figure 3-2: The future evolution of Enceladus's eccentricity in the Enceladus-Dione 2:1 e -Enceladus type resonance for $k_2/Q = 1.0 \times 10^{-4}$. After the chaotic phase the system enters a limit cycle in which the eccentricity oscillates.

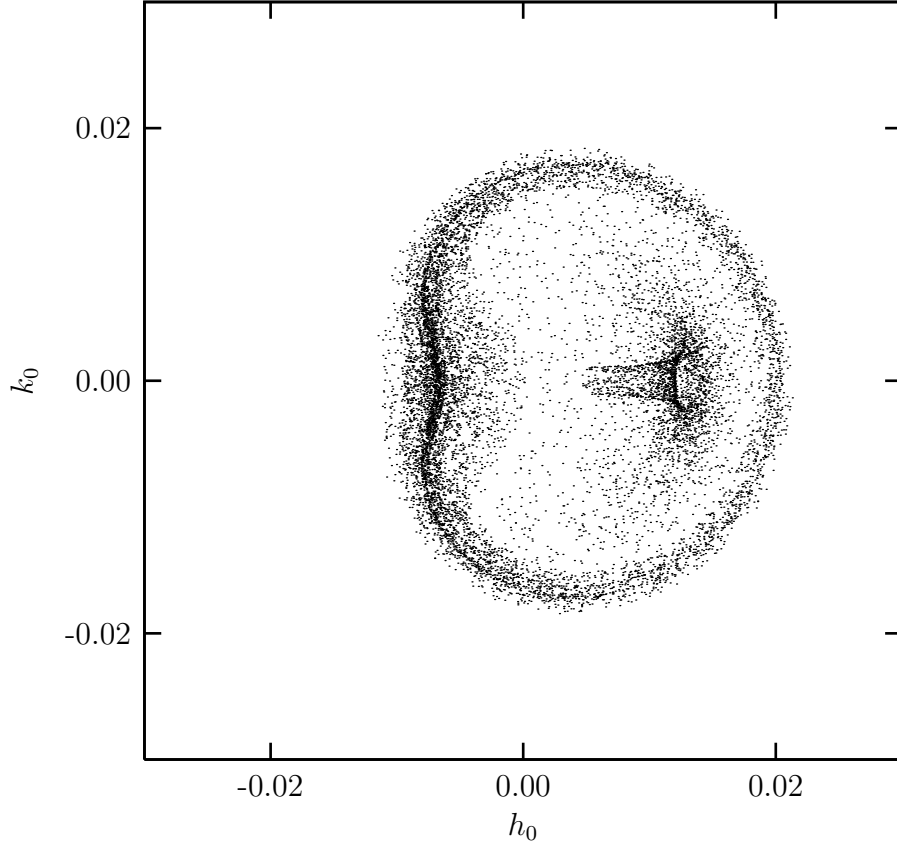


Figure 3-3: The initial evolution, spanning 1.3 Gyr, for $k_2/Q = 1.0 \times 10^{-4}$ is shown in the phase plane $h_0 = e_0 \sin \sigma_0$ versus $k_0 = e_0 \cos \sigma_0$. The evolution begins with a libration near $\sigma_0 = 0$, the amplitude increases as the eccentricity increases. There is a chaotic transient which makes a splatter of points on the phase plane. The system eventually settles down on a limit cycle (see Figure 3-4).

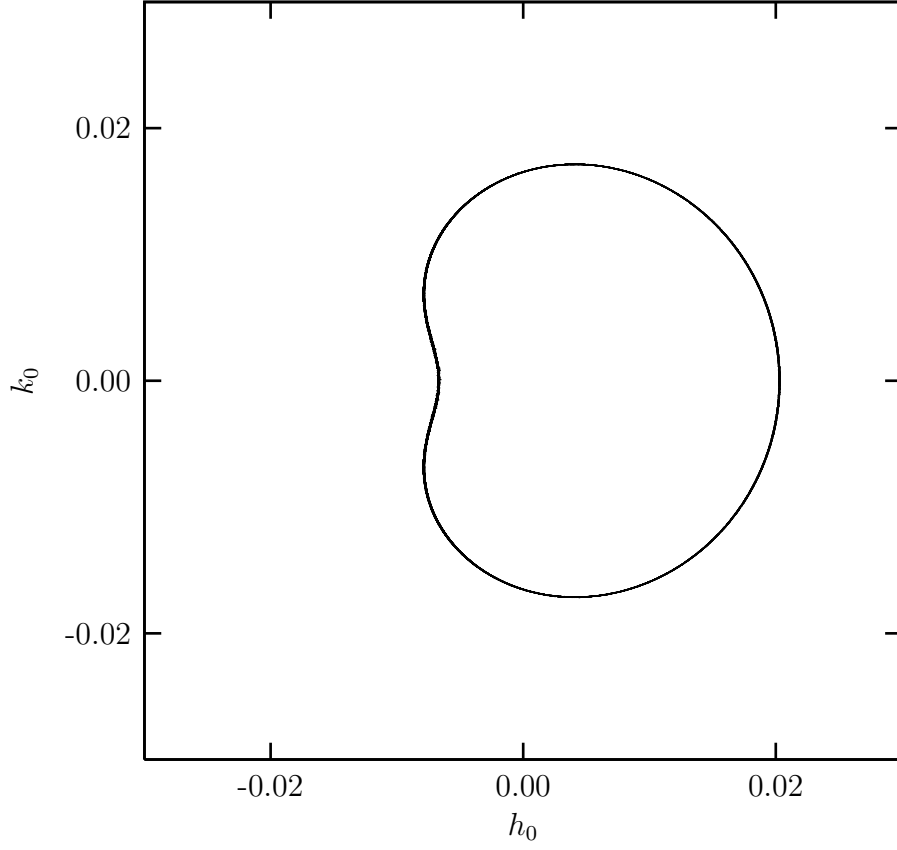


Figure 3-4: The evolution of Enceladus in the Enceladus-Dione 2:1 e -Enceladus type resonance for $k_2/Q = 1.0 \times 10^{-4}$ eventually settles on a limit cycle, shown here in the phase plane $h_0 = e_0 \sin \sigma_0$ versus $k_0 = e_0 \cos \sigma_0$. The plotted segment of the orbit spans 3 Gyr.

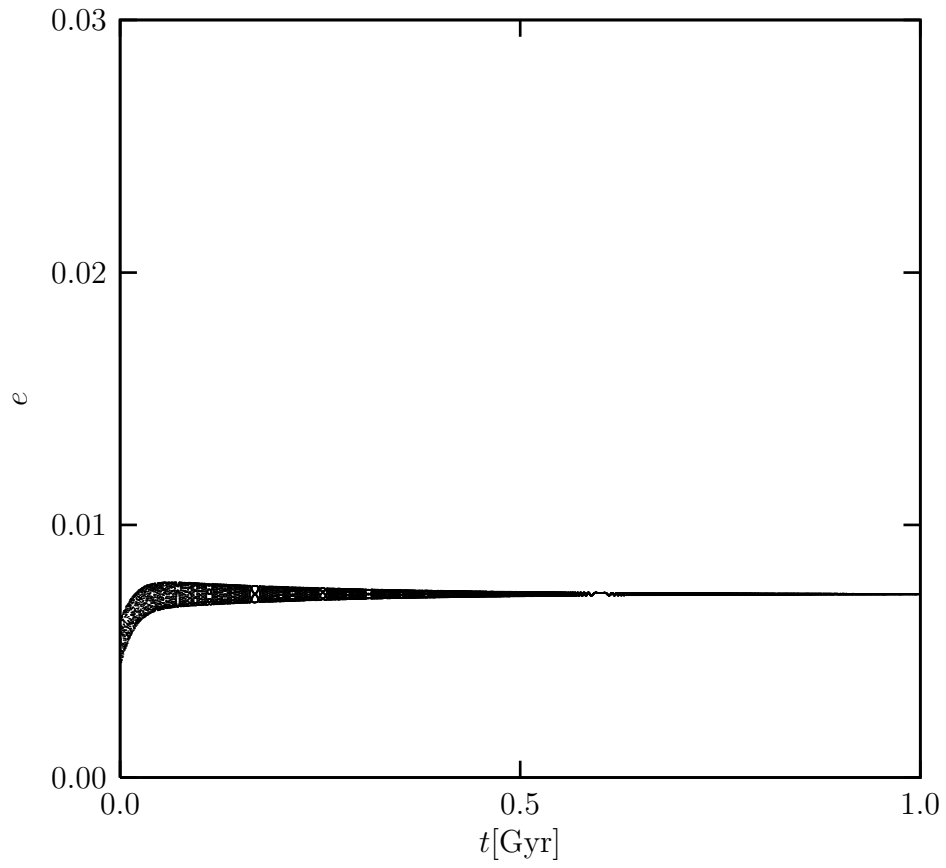


Figure 3-5: The eccentricity of Enceladus in the Enceladus-Dione 2:1 e -Enceladus type resonance for $k_2/Q = 3.3 \times 10^{-4}$ reaches a stable equilibrium. The libration amplitude damps to zero.

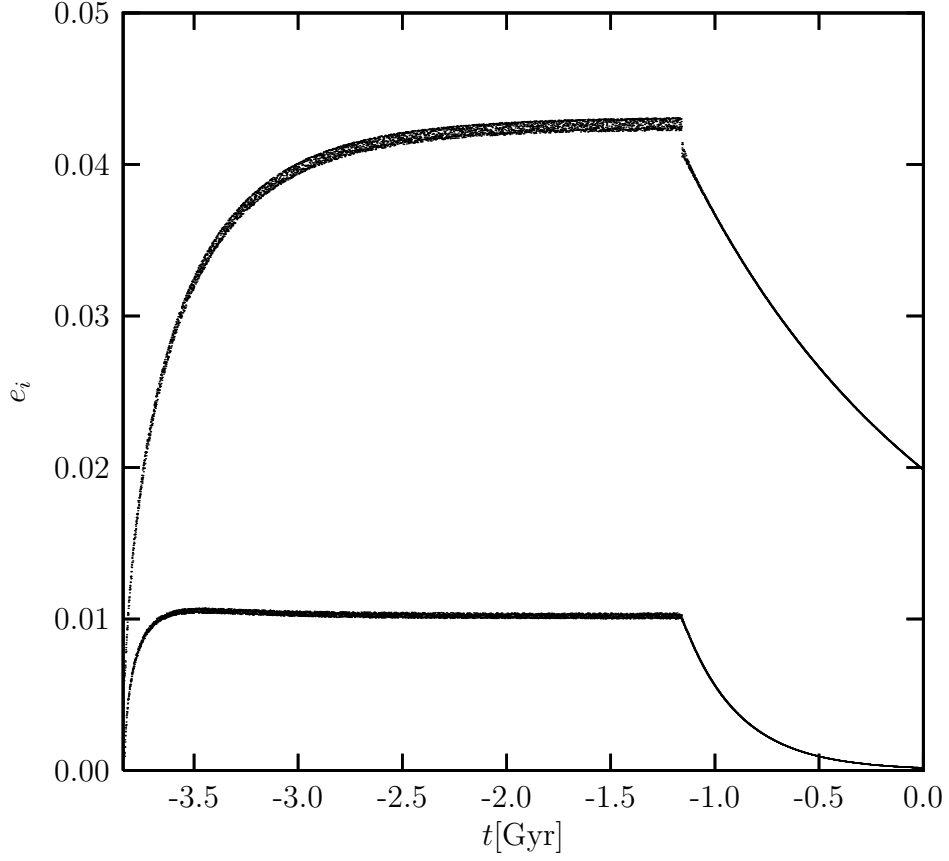


Figure 3-6: The upper trace shows the evolution of the eccentricity of Mimas in the Mimas-Enceladus 6:4 mixed ee' resonance. The lower trace shows the evolution of the eccentricity of Enceladus. After leaving the resonance at -1.15 Gyr (for $Q_S = 18,000$), the eccentricity of Mimas decays to the current free eccentricity. Here k_2/Q for Mimas is 1.3×10^{-6} , and k_2/Q for Enceladus is 4.1×10^{-5} .

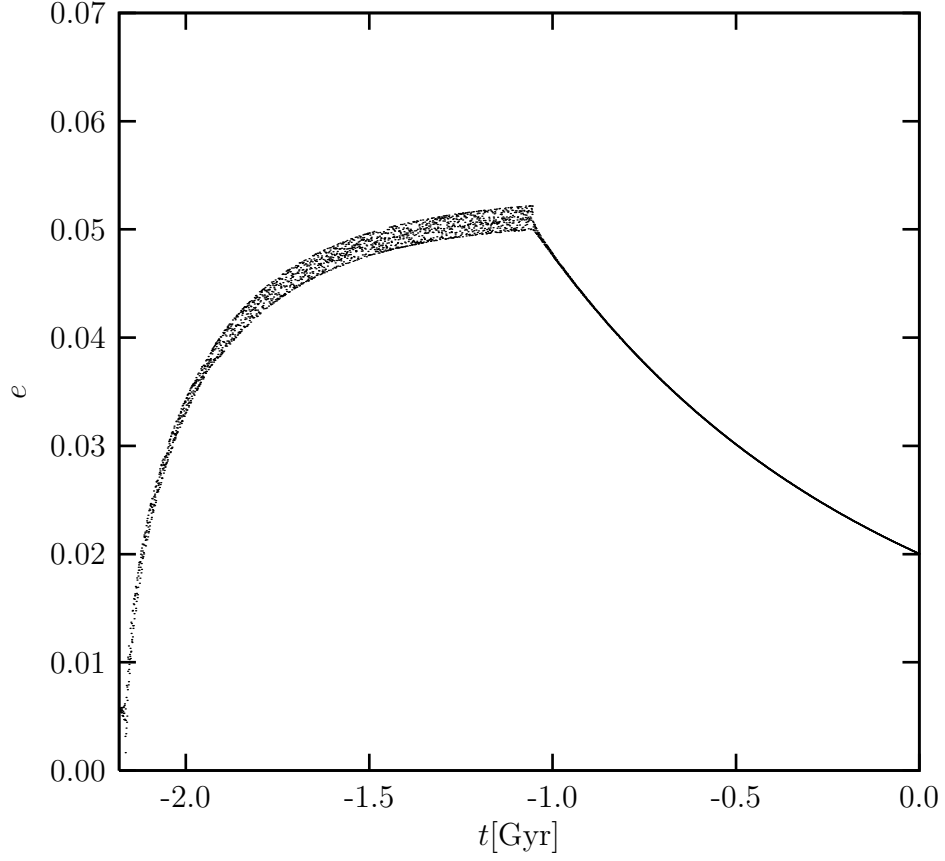


Figure 3-7: The evolution of the eccentricity of Mimas as it encounters the Mimas-Enceladus 3:2 e -Mimas resonance. The eccentricity approaches an equilibrium value of 0.052, but as it reaches equilibrium, the libration amplitude grows. Eventually the system escapes from the resonance and the eccentricity decays to the current value at the present. Here k_2/Q of Mimas is 1.42×10^{-6} and the timescale for eccentricity decay is about 1.3 Gyr.

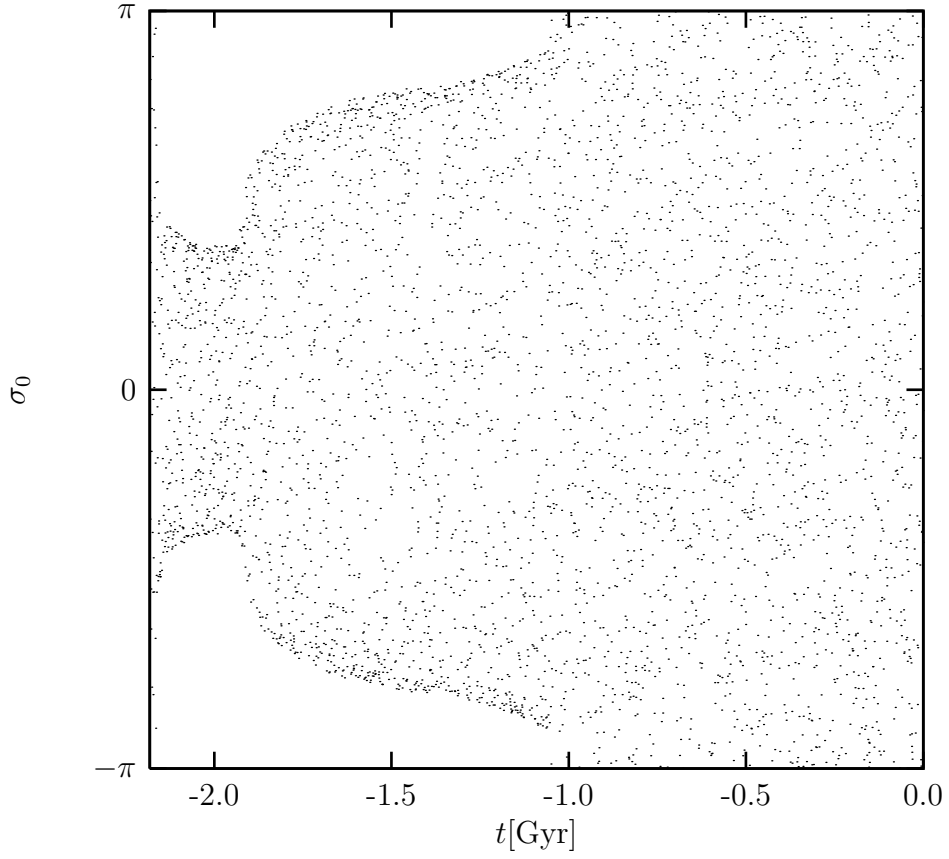


Figure 3-8: The resonance angle of the Mimas-Enceladus 3:2 *e*-Mimas resonance versus time. There is a sudden growth in the libration amplitude because the system was captured by a 3-fold secondary resonance. When the amplitude reaches π , the system falls out of resonance. This figure corresponds to Figure 3-7.

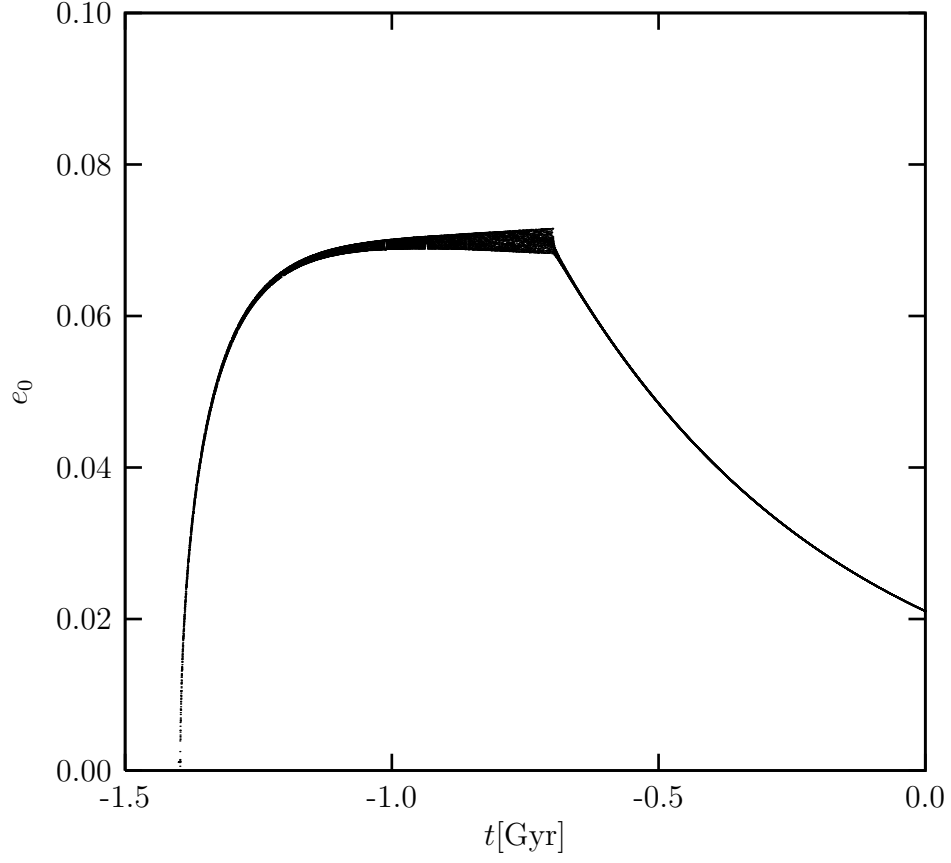


Figure 3-9: The evolution of the eccentricity of Mimas as it encounters the Mimas-Dione 3:1 e^2 -Mimas resonance. The eccentricity grows to an equilibrium value of 0.07 before escaping the resonance and decaying to the present value of 0.02. Escape from the resonance occurs via unstable growth of the libration amplitude. Here k_2/Q for Mimas is 3.0×10^{-6} .

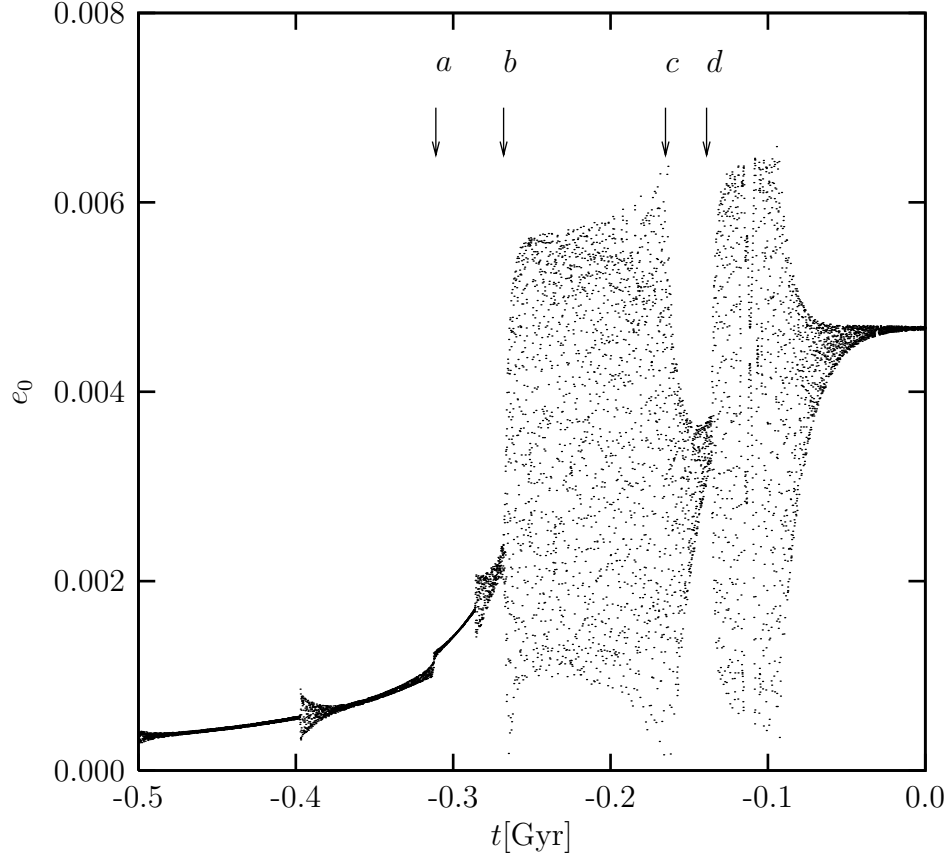


Figure 3-10: The past evolution of the eccentricity of Enceladus in the Enceladus-Dione 2:1 multiplet of resonances. Feature ‘b’ shows the entrance into the ee' resonance and feature ‘d’ shows capture into a 2:1 secondary resonance. In this simulation, the k_2/Q of Enceladus is the equilibrium value of 8.0×10^{-4} , so the constant equilibrium eccentricity of Enceladus, which it achieves shortly after it leaves the secondary resonance, is the current value of 0.0047.

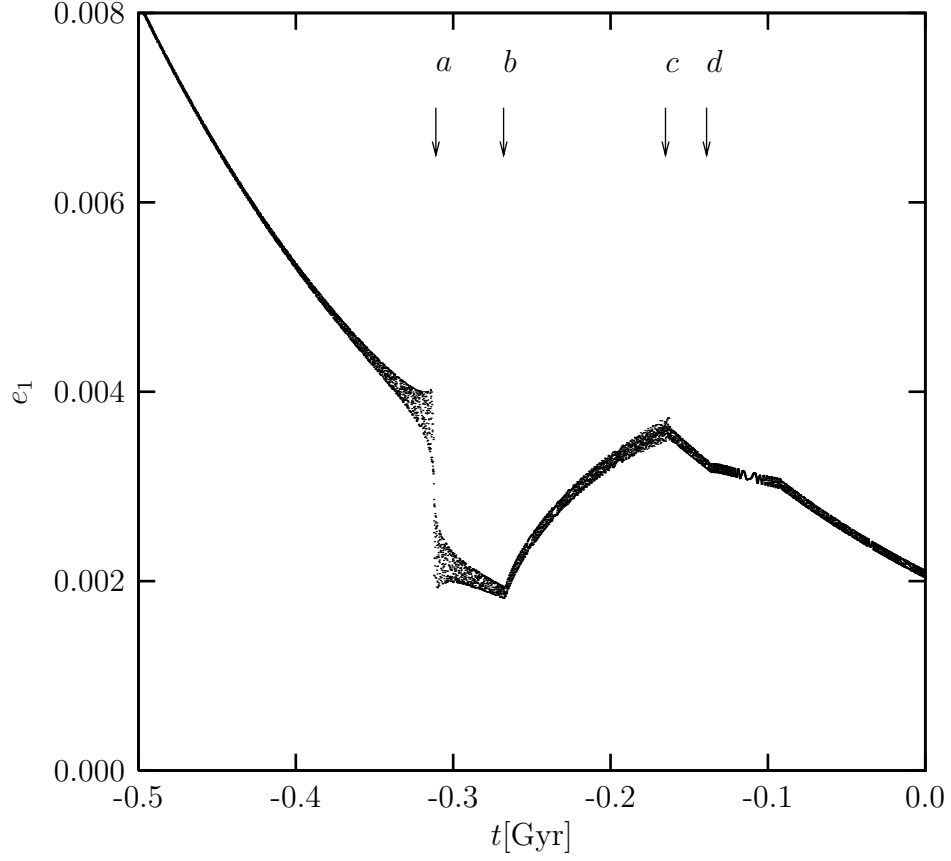


Figure 3-11: The past evolution of the eccentricity of Dione in the Enceladus-Dione 2:1 multiplet of resonances. Feature ‘a’ shows passage through the e -Dione resonance. The rise in eccentricity between events ‘b’ and ‘c’ is due to the ee' -mixed resonance. The value of k_2/Q of Dione is 1.24×10^{-4} .

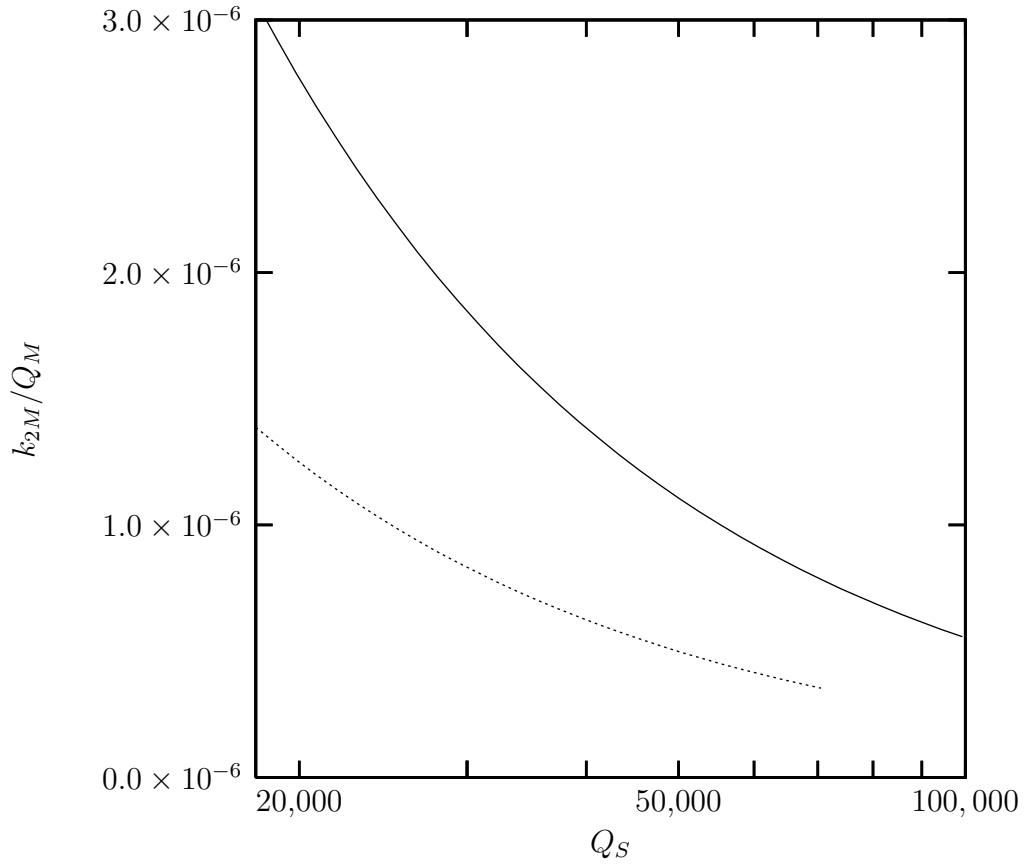


Figure 3-12: The solid line shows the k_2/Q for Mimas for which the eccentricity of Mimas will decay to the current value for a given Q_S if the system was caught in the Mimas-Dione 3:1 e^2 -Mimas resonance. The dotted line shows the k_2/Q for Mimas for which the eccentricity of Mimas will decay to the current value for a given Q_S if the system was caught in the Mimas-Enceladus 3:2 e -Mimas resonance.

Chapter 4

Episodic Volcanism on Enceladus: Application of the Ojakangas-Stevenson Model

The main equations in the paper “Episodic Volcanism of Tidally Heated Satellites with Application to Io” by Ojakangas & Stevenson (1986) are presented; numerical integration of these equations confirms the results of Ojakangas & Stevenson (1986) for Io. Application to Enceladus is considered. It is shown that Enceladus does not oscillate about the tidal equilibrium in this model by both new nonlinear stability analysis and numerical integration of the model equations.

4.1 Introduction

We have shown that equilibrium tidal heating in Enceladus cannot account for the non-solar heat emanating from Enceladus (Meyer & Wisdom, 2007): equilibrium tidal heating can account for only $1.1(18000/Q_S)$ GW of the observed 17.0 ± 3.3 GW (Howett et al., 2010), increased from 5.8 ± 1.9 GW (Spencer et al., 2006). Provided the origin of the observed heating is tidal heating, it is possible that Enceladus is oscillating about equilibrium. A model for oscillation about equilibrium has been presented for Io by Ojakangas & Stevenson (1986). Fischer & Spohn (1990) pre-

sented similar oscillation models for Io, emphasizing different rheologies. Ojakangas & Stevenson (1986) mentioned the possible application of their model to Enceladus.

The Ojakangas & Stevenson (1986) model would only apply to Enceladus if heat transport is mainly by convection. Squyres et al. (1983) discuss whether convection occurs in Enceladus. They consider a convecting region overlain by a nonconvecting, conductive crustal ice layer. They find that for crustal thicknesses larger than 30km, heat transport is dominated by convection. Here we assume convection occurs and that the Ojakangas & Stevenson (1986) model is applicable to Enceladus.

We first review the Ojakangas & Stevenson (1986) model. We carry out a new linear stability analysis for their full model. We show that, in fact, Enceladus does not oscillate about the tidal equilibrium within the Ojakangas & Stevenson (1986) model.

4.2 Ojakangas and Stevenson Evolution Equations

Consider the thermal evolution of a satellite, with index 0, in resonance with another satellite, with index 1, exterior to it. Let m_i be the mass of the satellite i , and n_i be the mean motion. The semimajor axis of the inner satellite is a and its orbital eccentricity is e .

The physical parameters of the inner satellite are the heat capacity C_p , the temperature T , the radius R , the density ρ , the thermal diffusivity K , the surface gravitational acceleration g , the thermal expansion coefficient α_T , the kinematic viscosity $\nu(T)$, the critical Rayleigh number Ra_c , and the Love number $k(T)$ and the tidal quality factor $Q(T)$. The values adopted for these physical parameters are listed in table 4.1.

The basic equation for the thermal state states that the rate of change of the thermal energy in the satellite is a balance between tidal heating and loss from thermal convection:

$$m_0 C_p \frac{dT}{dt} = \frac{21}{2} \frac{GM_p^2 R^5 n_0}{a^6} \left(\frac{k(T)e^2}{Q(T)} \right) - 4\pi R^2 \rho C_p K T \left(\frac{g \alpha_T T}{\nu(T) K Ra_c} \right)^{1/3}. \quad (4.1)$$

The temperature dependence of the factor Q/k is unknown, but approximated by a power law near the solidus and a constant at low temperature. A form that interpolates these characteristics is

$$\frac{Q(T)}{k(T)} = f(T/T_m) = \left[\left(\frac{Q}{k} \right)_0^{-1} + A \left(\frac{T}{T_m} \right)^n \right]^{-1}, \quad (4.2)$$

with

$$A = \left(\frac{Q}{k} \right)_{min}^{-1} - \left(\frac{Q}{k} \right)_0^{-1}, \quad (4.3)$$

where T_m is the melting temperature, $(Q/k)_0$ is the value of Q/k at low temperature, and $(Q/k)_{min}$ is the minimum value of Q/k that is reached near the melting temperature. The viscosity is taken as a power law

$$\nu(T) = \nu_{TM}(T/T_m)^{-L}, \quad (4.4)$$

where, in silicates, $20 < L < 30$, and $\nu_{TM} = 10^{12}$ - 10^{13} m²s⁻¹. In water ice, $35 < L < 37$, and $\nu_{TM} = 10^{10}$ m²s⁻¹ (Durham et al., 1997).

The equilibrium value of the temperature is

$$T_0 = \left[\frac{7}{2\beta} \frac{k_p}{Q_p} \frac{Gm_0 R R_p^5 n_0}{C_p a^6} \left(\frac{\nu_{TM} T_m^L R a_c}{g \alpha_T K^2} \right)^{1/3} \right]^{1/m}, \quad (4.5)$$

where $m = (L + 4)/3$, and $\beta = 13$ for Io in the Io-Europa-Ganymede resonance and $\beta = 30.69$ for Enceladus in the Enceladus-Dione resonance (Meyer and Wisdom, 2007). The equilibrium value of the square of the eccentricity is

$$e_0^2 = \frac{m_0^2 R_p^5 k_p}{\beta M_p^2 R^5 Q_p} f(T_0/T_m). \quad (4.6)$$

The convective cooling timescale is

$$\tau_{th} = \frac{R}{3} \left(\frac{\nu_{TM} T_m^L R a_c}{g \alpha_T K^2} \right)^{1/3} T_0^{1-m}. \quad (4.7)$$

The characteristic timescale for the equilibration of eccentricity near equilibrium is

$$\tau_e = \frac{m_1 \alpha |C(\alpha)|}{2M_p \gamma c_0 e_0}, \quad (4.8)$$

where α is the semimajor axis ratio a_0/a_1 , $C(\alpha)$ is about -1.19 for a $2 : 1$ mean motion resonance,

$$c_0 = \frac{9}{2} \left(\frac{R_p}{R} \right)^5 \frac{m_0}{M_p} n_0 \frac{k_p}{Q_p}, \quad (4.9)$$

and γ is about 0.32 for the Io-Europa-Ganymede resonance. For a two-body $j : j - 1$ resonance,

$$\gamma = j - 1 - j \frac{m_1}{m_0} \left(\frac{a_0}{a_1} \right)^8. \quad (4.10)$$

For the Enceladus-Dione 2:1 resonance, $\gamma = 0.49$.

Let

$$p = \frac{\tau_{th}}{\tau_e} = \frac{6\beta}{7} \frac{C_p a \gamma}{G m_1 \alpha |C(\alpha)|} e_0 T_0. \quad (4.11)$$

For Io this constant is about 3.

Define the non-dimensional temperature $T_N = T/T_0$, the scaled eccentricity $e_N = e/e_0$, and the non-dimensional time $t_N = t/\tau_{th}$. With these definitions the non-dimensionalized evolution equations are

$$\frac{dT_N}{dt_N} = \left[\frac{f(T_0/T_m)}{f(T_N T_0/T_m)} \right] e_N^2 - T_N^m \quad (4.12)$$

$$\frac{de_N}{dt_N} = e_N^2 \frac{p}{2} \left[1 - \frac{f(T_0/T_m)}{f(T_N T_0/T_m)} e_N^2 \right] \quad (4.13)$$

The equilibrium heat flow is

$$q_0 = \frac{m_0 C_p T_0}{4\pi R^2 \tau_{th}} \quad (4.14)$$

$$= \frac{7}{2\beta} \frac{k_p}{Q_p} \frac{G m_0 R R_p^5 n_0 \rho}{a^6}, \quad (4.15)$$

which is $0.53(100,000/Q_J)$ W m⁻² for Io, and $1.48(18,000/Q_S)$ mW m⁻² for Enceladus. The latter corresponds to a total power of $1.1(18,000/Q_S)$ GW emanating from Enceladus.

In integrating the evolution equations, several assumptions have to be made. The temperature T does not rise above T_m . During an interval in which $T = T_m$, the tidal heating rate is greater than the convective cooling rate, and the excess energy is assumed to be released through volcanism. The interval of $T = T_m$ is terminated when the rate of tidal heating falls (due to the declining eccentricity) below the rate of convective cooling. The heat flow during an interval in which $T < T_m$ is given by the convective cooling term; the heat flow during an interval in which $T = T_m$ is given by the tidal heating term.

The eccentricity and heat flow of Io as functions of time are shown in Figure 4-1. We confirm the oscillatory behavior found by Ojakangas & Stevenson (1986). The same plot for Enceladus (Figure 4-2) shows no evidence of oscillatory behavior.

4.3 Stability Analysis

Ojakangas & Stevenson (1986) carry out a linear stability analysis for their simplified model in which $Q(T)/k(T)$ is a power law. They then introduce a more realistic form for $Q(T)/k(T)$ that approaches a constant for small T (see eq. 4.2). However, they do not carry out the stability analysis for this case. Here we describe how the results of the linear stability analysis are modified for their more realistic model.

For the simplified model they found that the equilibrium state, $e_N = T_N = 1$, was unstable if $n > m + p$. Further, they found that there were linear oscillations (either growing or decaying) provided

$$m^2 + n^2 + p^2 - 2mp - 2mn - 2np < 0. \quad (4.16)$$

When the tidal equilibrium is linearly unstable, the nonlinear system oscillates.

We have carried out a linear stability analysis for the more realistic model in which $Q(T)/k(T)$ is given by eq. (4.2). We find that the results of their analysis for the simplified model continue to hold in the more realistic model if n is replaced by

$$n' = nA(T_0/T_m)^n f(T_0/T_m) \quad (4.17)$$

Thus the equilibrium is linearly unstable if $n' > m+p$, and there are linear oscillations (growing or decaying) if

$$m^2 + (n')^2 + p^2 - 2mp - 2mn' - 2n'p < 0. \quad (4.18)$$

For Io, $n' \approx n$, for n in the range of interest $20 < n < 30$, and $T_0/T_m \approx 0.94$. The system is linearly unstable and develops nonlinear oscillation at moderate $n \approx n'$.

For Enceladus, T_0/T_m is smaller ($T_0/T_m \approx 0.70$) so the dropoff in n' at large n is more rapid. In fact, the peak of n' is about 5, for n about 8. At this n , $p \approx 51.2$. Figure 4-3 shows a graph of n' and $m+p$ as a function of n . Enceladus is not in the unstable region for any n ; instability requires $n' > m+p$. This criterion cannot be fulfilled for Enceladus for two reasons: the large value of p requires a large value for n' for instability, and the maximum value of n' as a function of n is small. Thus for any n the state of Enceladus damps down to the equilibrium state. This conclusion is insensitive to the values we have adopted for the physical parameters.

4.4 Conclusion

We have shown that Enceladus does not oscillate about the tidal equilibrium within the Ojakangas & Stevenson (1986) model. If Enceladus is oscillating about equilibrium, then another model must be developed to describe those oscillations. One possibility is the idea expressed by Yoder & Peale (1981) that there might be oscillations about equilibrium if the Q of Enceladus was stress dependent, but this idea has not been developed.

	Io	Enceladus
$M_p [10^{24} \text{ kg}]$	1898.8	568.5
$m_0 [10^{20} \text{ kg}]$	893.3	1.08
$m_1 [10^{20} \text{ kg}]$	479.7	10.95
$R_p [\text{km}]$	71492	60330
Q_p	10^5	1.8×10^4
$a [\text{km}]$	421769	238400
$R [\text{km}]$	1821.3	252.3
k_{2p}	0.38	0.341
Ra_c	800	800
$\alpha_T [\text{K}^{-1}]$	3.0×10^{-5}	5.1×10^{-5}
$K [\text{m}^2 \text{ s}^{-1}]$	1.0×10^{-6}	1.35×10^{-7}
$C_p [\text{J kg}^{-1} \text{ K}^{-1}]$	800	2100
$T_m [\text{K}]$	1400	273
$\rho [\text{kg m}^{-3}]$	3500	1602
$g [\text{m s}^{-2}]$	1.8	0.11
k_2	0.027	0.0018
$\nu_{TM} [\text{m}^2 \text{ s}^{-1}]$	$10^{12}\text{-}10^{13}$	10^{10}
β	13	30.7
γ	0.32	0.49
n	20-30	?
m	8-12	13
L	20-30	35-37

Table 4.1: The adopted physical parameters for Io and Enceladus are presented.

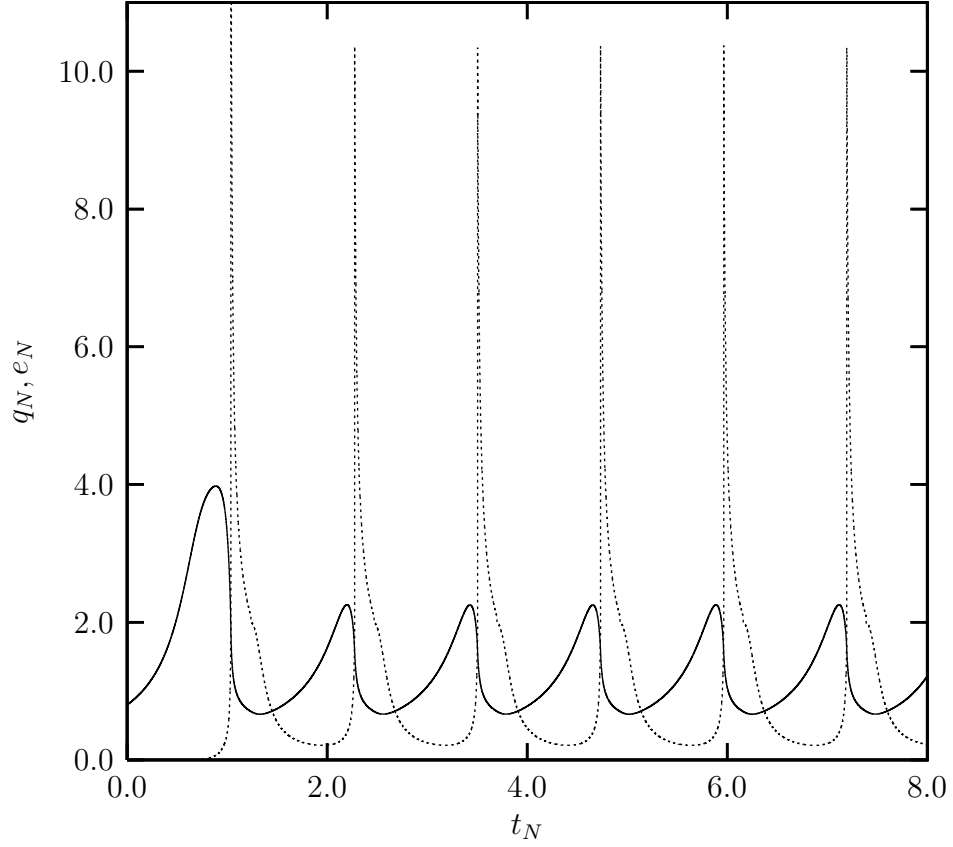


Figure 4-1: The scaled eccentricity e_N (solid) and the non-dimensional heat flow q_N (dotted) are plotted versus the non-dimensional time for Io. The timescale τ_{th} is about 135Myr, the scale for the heatflow is 0.53 W m^{-2} , and the scale for the eccentricity is 0.0052. Here $m = 12$, $n = 25$, $(Q/k)_0 = 200/0.027$, $(Q/k)_{min} = 3/0.027$, and $Q_J = 10^5$.

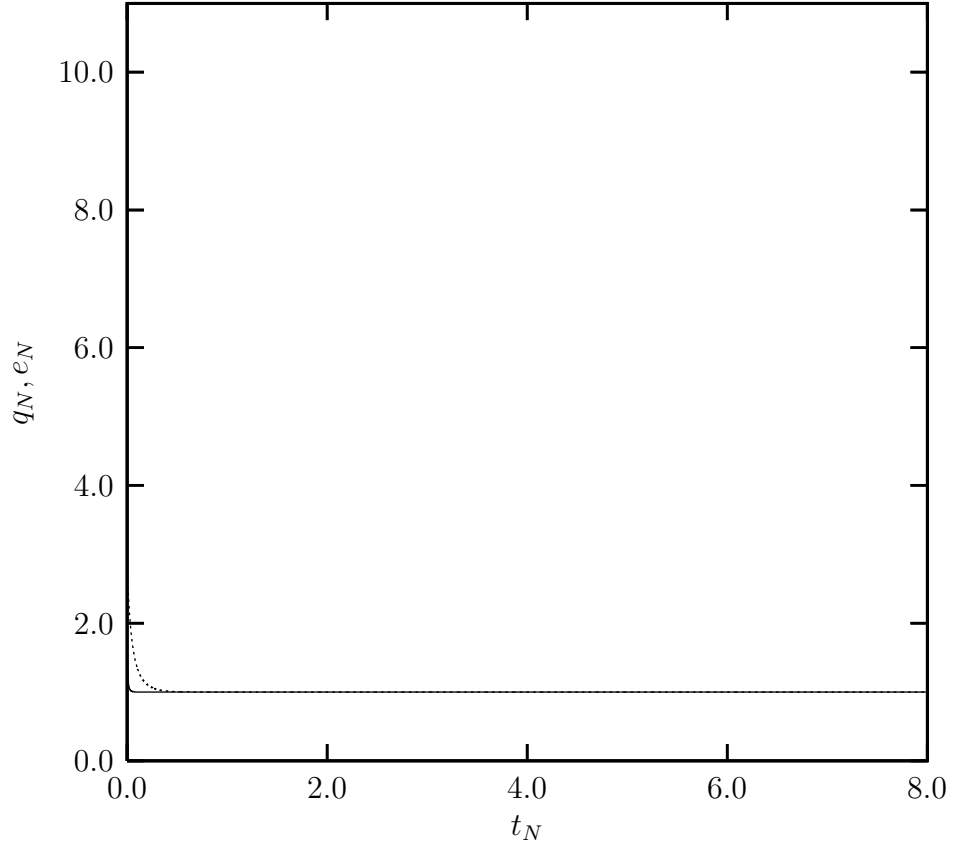


Figure 4-2: The scaled eccentricity e_N (solid) and the non-dimensional heat flow q_N (dotted) for Enceladus are plotted versus the non-dimensional time.

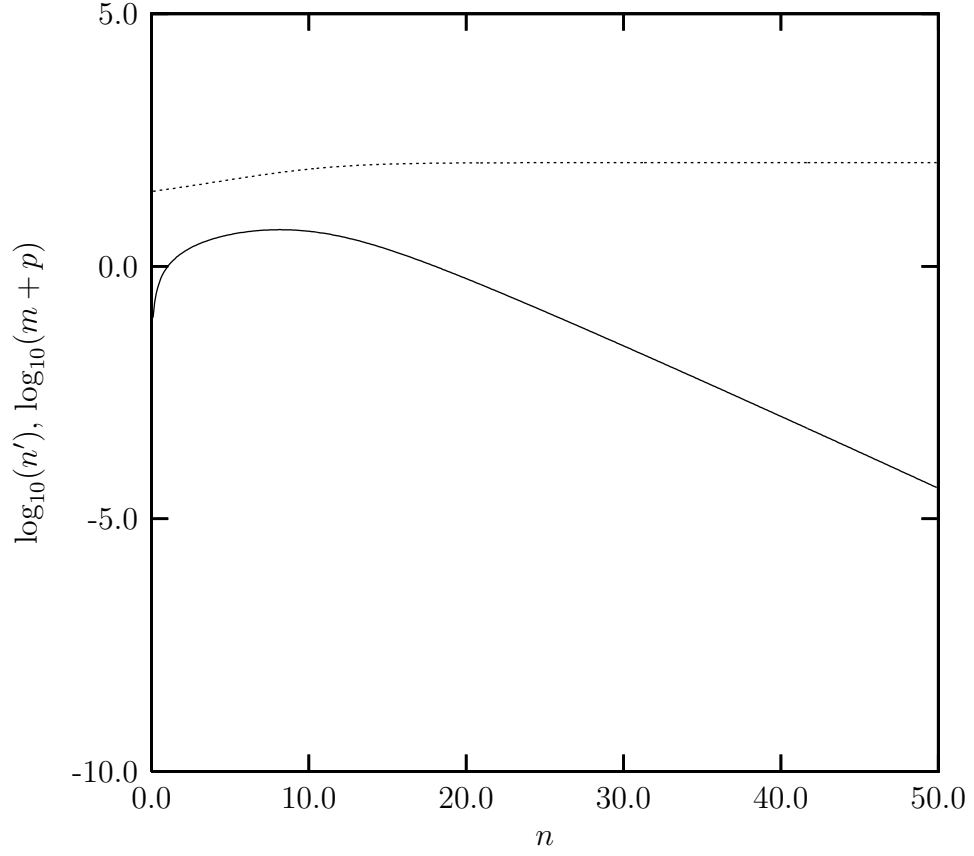


Figure 4-3: The parameter n' (solid) is plotted as a function of n , for Enceladus. This is to be compared with $m+p$ (dotted) plotted as a function of n . For $n' < m+p$ the system damps to the equilibrium state. The system is stable for all n . Here $(Q/k)_0$ is 100/0.0018; $(Q/k)_{min}$ is 3/0.0018; $T_0/T_m = 0.70$; and $m = 13$.

Chapter 5

Coupled Thermal-Orbital Evolution of the Early Moon

Coupled thermal-orbital histories of early lunar evolution are considered in a simple model. We consider a plagioclase lid, overlying a magma ocean, overlying a solid mantle. Tidal dissipation occurs in the plagioclase lid and heat transport is by conduction and melt migration. We find that large orbital eccentricities can be obtained in this model. We discuss possible consequences of this phase of large eccentricities for the shape of the Moon and geochronology of lunar samples. We find that the orbit can pass through the shape solution of Garrick-Bethell et al. (2006), but we argue that the shape cannot be maintained against elastic deformation as the orbit continues to evolve.

5.1 Introduction

Garrick-Bethell et al. (2006) argued that the shape of the Moon could be explained if the Moon froze in its shape while its orbit was eccentric and the rotation state was either synchronous or in the 3:2 commensurate state (as is Mercury). For synchronous rotation the implied orbit is $a = 22.9R_E$, $e = 0.49$, and for the 3:2 spin-orbit state the orbit is $a = 24.8R_E$, $e = 0.17$, where a is the semimajor axis of the lunar orbit and e is the orbital eccentricity. There are two questions to be addressed by this hypothesis:

can evolutionary scenarios be generated such that the lunar orbit passes through the shape solutions, and can the shape of the Moon be frozen in at this epoch?

Past studies of the evolution of the lunar orbit have largely ignored the evolution of the eccentricity, and focused instead on the evolution of the orbital inclination (Goldreich, 1966; Touma & Wisdom, 1994). One exception is Touma & Wisdom (1998), in which the evolution of the lunar orbit through the evection and eviction resonances was studied. Large eccentricities were obtained, but at an earlier epoch (and smaller semimajor axis) in the evolution of the lunar orbit than suggested by the shape solutions. In this paper we explore an evolutionary scenario that reaches moderately large eccentricities during the epoch indicated by the shape results. A key element of our scenario is that the orbital evolution is coupled to the thermal evolution; in this model large eccentricities can be obtained during the shape epoch and still decay sufficiently to connect to the current configuration of the lunar orbit.

We present a coupled thermal model for the evolution of the lunar orbit. We expect that in a lid decoupled from the mantle by a magma ocean tidal heating will be enhanced in the lid (Peale et al., 1979) and dominate that in the mantle. Here we assume dissipation occurs entirely in the lid and that heat transport in the lid is by conduction and melt migration. The model is limited, and there are many unknown parameters. Our goal is not to explore evolutions for all possible parameters, but to determine whether a high eccentricity orbital phase passing through the shape solution and consistent with today's orbit can be obtained.

In the next section we review aspects of lunar geochronology. Then we recall the Mignard evolutionary equations, correcting a number of typographical errors. This is followed by a presentation of the dissipative lid thermal model, a discussion of the elastic stability of the shape, and our conclusions. In Appendix B, we present in detail the two layer model for tidal dissipation developed by Peale & Cassen (1978) in their classic study of tidal dissipation in the Moon, correcting a number of typographical errors and making the results explicit.

5.2 Geochronology Constraints

At the beginning of magma ocean solidification the iron- and magnesium-rich phases crystallizing from the cooling magma sink to the bottom of the magma ocean. When approximately 80% of the lunar magma ocean has solidified, plagioclase will begin to crystallize and float; plagioclase will continue to be added to this flotation crust until the last dregs of the magma ocean solidify (Snyder et al., 1992). The ages of the plagioclase in the anorthosite flotation crust, therefore, could span the range from about 80% solidification to the age when the last plagioclase cools below its closure temperature. Here we stress that though geochronological anorthosite ages have often been interpreted as recording the time of magma ocean solidification, the two are actually decoupled. Anorthosite begins to form long before the magma ocean is solidified, greatly prolongs the remaining solidification process, and may record ages younger than the time of magma ocean solidification if cooled slowly or reheated later.

The short half-life of the tungsten-hafnium (W-Hf) decay system allows dating of the time of separation of the metallic core of a planet from its silicate mantle. Recent work by Touboul et al. (2007) indicates that both the Moon and Earth differentiated primarily after the W-Hf system was extinct, that is, at $60 - 10/+90$ Myr or more after solidification of the first solar system materials. Earlier measurements using the same system lead Yin et al. (2002) to conclude that the giant Moon-forming impact occurred at 29 Myr after solar system formation.

Using 4.567 Gyr as the formation time of the oldest solar system materials (Connelly et al., 2008) and both the W-Hf dates described here, the earliest age that the Earth and Moon likely differentiated is between 4.538 and 4.507 Gyr. This age for the putative Moon-forming giant impact marks the beginning of the geochemically-determined timeline of formation and cooling of the Moon.

The oldest surface materials on the Moon are assumed to be the anorthositic highlands, formed by flotation in the lunar magma ocean (Wood et al., 1970; Smith et al., 1970). Though there have been a number of geochronological ages determined

using the Sm-Nd system, it has inherent difficulties that are improved upon by using the more precise U-Pb system. Nemchin et al. (2009) dated a single zircon crystal from a lunar crustal breccia and obtained an age of $4.417 \pm .06$ Gyr. This zircon was likely the product of crystallization of a small pocket of melt, and implies that this portion of the crust recorded an age of 90 to 121 million years after lunar formation.

Planets with a magma surface should cool extremely quickly (Abe, 1993, 1997; Elkins-Tanton, 2008). A plagioclase flotation crust will slow the cooling of the planet significantly in comparison to the cooling of a magma ocean with a liquid surface. Calculations based on techniques from Elkins-Tanton (2008) indicate that the lunar magma ocean may have solidified to 80% in less than 10^4 years, and perhaps as little as 10^3 years. After this near-instantaneous interval plagioclase will begin to form and float. Once sufficient anorthosite has floated to cover the surface of the Moon, cooling will slow substantially; conductive heat loss through the anorthosite lid is the rate-limiting step in cooling.

The anorthosite will record the age at which it cooled past its closure temperature. When the minerals making up the lid are heated, they are prone to losing their radiogenic daughter products through increased diffusion. The closure temperature below which radiogenic ages are preserved through lack of diffusion depends upon mineral type, mineral composition, cooling rate, and absolute temperature. Zircon would lose its original lead composition when subjected to moderate thermal events, on the order of 1000°C , for even short periods. A 0.1 mm zircon that is heated to 1000°C for 20,000 years will lose its lead and be geochronologically reset (Cherniak & Watson, 2003). Therefore, no matter when the anorthosite originally formed, if it remains hot or is again heated, the age will record that event. The mineral geochronology is effectively measuring the time of cooling of the tidally heated lid, and not its time of formation.

5.3 The Orbital and Rotational Model

Mignard (1979, 1980, 1981) has derived approximate averaged equations governing

the evolution of the lunar eccentricity and inclination. The equations of motion are averaged over the orbital period and the period of precession of the lunar orbit. Solar perturbations are included. We use these here, but we allow the relative amount of dissipation in the Moon to that in the Earth (the Mignard A parameter) to change with the thermal state of the Moon.

The Mignard evolutionary equations are:

$$\frac{dX}{dt} = \frac{C_X}{X^7} \left[-\frac{f_0}{\beta^{15}}(1+A) + \left(UX^{3/2} \cos i + A \frac{\omega'}{n} \cos(I') \right) \frac{f_1}{\beta^{12}} \right] \quad (5.1)$$

$$\frac{de}{dt} = \frac{C_e}{X^8} \left[-\frac{f_3}{\beta^{13}}(1+A) + \left(UX^{3/2} \cos i + A \frac{\omega'}{n} \cos(I') \right) \frac{f_4}{\beta^{10}} \right] \quad (5.2)$$

$$\frac{di}{dt} = -\frac{C_i}{X^{13/2}} \sin i \left(U + \frac{A}{X^{3/2}} \right) \frac{f_2}{\beta^{10}} \quad (5.3)$$

$$\begin{aligned} \frac{dU}{dt} = & -C_{U,0} \left[U - \frac{n_\odot}{n_G} \right] + C_{U,1} \frac{1}{X^{15/2}} \left[\frac{f_1}{\beta^{12}} - UX^{3/2} \cos i \frac{f_2}{\beta^9} \right] \cos i \\ & - C_{U,2} U (\sin i)^2 \frac{1}{X^6} \frac{f_2}{\beta^9} \end{aligned} \quad (5.4)$$

$$\begin{aligned} \frac{d(\omega/n_G)}{dt} = & \frac{C_{\omega,0}}{X^6} \left[-\frac{f_2}{\beta^9} \left[\left(\frac{\omega}{n_G} \right)^2 \frac{2 + (\sin i)^2}{2} + U^2 \frac{3(\cos i)^2 - 1}{2} \right] \right. \\ & \left. + 2U \cos i \frac{f_1}{\beta^{12}} \frac{1}{X^{3/2}} \right] + C_{\omega,1} \left[2 \frac{n_\odot}{n_G} U - \left(\frac{\omega}{n_G} \right)^2 - U^2 \right] \end{aligned} \quad (5.5)$$

where $\beta = \sqrt{1 - e^2}$, $U = (\omega/n_G) \cos(I)$, the grazing mean motion $n_G = \sqrt{GM/R_E^3}$, G is Newton's constant, $X = a/R_E$, with R_E the radius of the Earth, a is the semimajor axis of the lunar orbit, e the orbital eccentricity, n is the orbital mean motion of the Moon around the Earth, n_\odot is the orbital mean motion of the Earth around the Sun, i is the orbital inclination to the ecliptic, I is obliquity, ω is rotation rate, m is the mass of the Moon, M is the mass of the Earth, $\mu = (1/m + 1/M)^{-1}$ is the reduced mass, and unless otherwise stated primed variables refer to the Moon and unprimed variables refer to the Earth. We also define

$$C_X = 6\gamma \frac{m}{M} \frac{m}{\mu} \quad (5.6)$$

$$C_e = 3\gamma \frac{m}{M} \frac{m}{\mu} \quad (5.7)$$

$$C_i = \frac{3}{2} \frac{\gamma}{\alpha} \left(\frac{m}{M} \right)^2 \quad (5.8)$$

$$C_{U,0} = 3 \frac{\gamma}{\alpha} \left(\frac{M_\odot}{M} \right)^2 \left(\frac{R_E}{a_E} \right)^6 \quad (5.9)$$

$$C_{U,1} = 3 \frac{\gamma}{\alpha} \left(\frac{m}{\mu} \right)^{1/2} \left(\frac{m}{M} \right)^2 \quad (5.10)$$

$$C_{U,2} = \frac{3}{2} \frac{\gamma}{\alpha} \left(\frac{m}{M} \right)^2 \quad (5.11)$$

$$C_{\omega,0} = 3 \frac{\gamma}{\alpha} \left(\frac{m}{M} \right)^2 \frac{m}{\mu} \quad (5.12)$$

$$C_{\omega,1} = 3 \frac{\gamma}{\alpha} \frac{m}{\mu} \left(\frac{M_\odot}{M} \right)^2 \left(\frac{R_E}{a_E} \right)^6 \quad (5.13)$$

where $\gamma = k_2 n^2 \Delta t$ and

$$\begin{aligned} f_0(e) &= 1 + \frac{31}{2}e^2 + \frac{255}{8}e^4 + \frac{185}{16}e^6 + \frac{25}{64}e^8 \\ f_1(e) &= 1 + \frac{15}{2}e^2 + \frac{45}{8}e^4 + \frac{5}{16}e^6 \\ f_2(e) &= 1 + 3e^2 + \frac{3}{8}e^4 \end{aligned} \quad (5.14)$$

$$f_3(e) = 9e + \frac{135}{4}e^3 + \frac{135}{8}e^5 + \frac{45}{64}e^7 \quad (5.15)$$

$$f_4(e) = \frac{11}{2}e + \frac{33}{4}e^3 + \frac{11}{16}e^5, \quad (5.16)$$

and

$$A = \frac{k'_2}{k_2} \frac{\Delta t'}{\Delta t} \left(\frac{M}{m} \right)^2 \left(\frac{R}{R_E} \right)^5 = \frac{k'_2}{Q'} \frac{Q}{k_2} \left(\frac{M}{m} \right)^2 \left(\frac{R}{R_E} \right)^5 \quad (5.17)$$

is a measure of the relative amount of dissipation in the Moon to the dissipation in the Earth, where k_2 is the potential Love number, Q is the tidal dissipation factor, and R is the radius of the Moon, 1738 km. The moment of inertia ratio for the Earth is $\alpha = C_E/(MR_E^2)$. We take $\alpha = 0.33$.

The Mignard model is limited. The doubly averaged equations cannot follow the precession of the lunar orbit. Furthermore, they use only a single tidal model (the constant Δt Mignard model). The current lunar laser ranging results indicate that the frequency dependence of tidal dissipation might be better described by a more complicated model (Williams, 2008; Efroimsky & Williams, 2009). However, the physical

state of the Earth and Moon in the situation under consideration is so different than at present it is not clear that the same frequency dependence would apply. We assume here that Q is temperature dependent, but ignore possible frequency dependence. A more complicated model does not seem warranted.

The obliquity of the Moon varies substantially as the orbit evolves (Ward 1975; Wisdom 2006); in particular large obliquities are obtained during the “Cassini transition” at around $a = 33R_E$, and the rate of tidal dissipation depends on the obliquity (Peale and Cassen 1978; Wisdom 2008). However, Peale and Cassen (1978) showed that the tidal heating due to the high obliquities during the Cassini transition did not substantially affect the thermal evolution of the Moon. Here, we are focusing on an earlier epoch during which the obliquity is likely to be close to zero. We take the lunar obliquity $I' = 0$ throughout the evolution.

In our simplified model we assume that the Mignard A parameter varies primarily due to variation in the k_2/Q of the Moon. This assumes that the change in dissipation in the Moon dominates that in the Earth. The reason for this is that the Moon has a lid, which makes the magma ocean last longer than that of the Earth. We define

$$A = C_A(k'_2/Q') \quad (5.18)$$

where $C_A = A_0/(k'_2/Q')_0$, where A_0 and $(k'_2/Q')_0$ are the initial values of these parameters.

The current value of the A parameter is about 0.3 (Williams et al., 2001), but the value of A early in the evolution of the Earth-Moon system is very uncertain. The Q of the Earth is currently dominated by the Earth’s oceans; the Earth’s solid body Q is estimated to be 280 (Ray et al., 2001). But the Q of the early Earth, which may have had a magma ocean, may be very different—perhaps ranging from 1 to 300. The k_2 of the early Earth might be more like the fluid Love number of the Earth (0.97) than its current value (0.299). The Q of the Moon has similar uncertainties—perhaps also ranging from 1 to 300. The k_2 of the Moon is presently dominated by rigidity (0.025); the k_2 of an early Moon might be closer to the fluid value of $3/2$ for a homogeneous

fluid body. Taking account of these uncertainties, the A parameter appropriate for the early Earth-Moon system might range from roughly $0.01 < A < 1000$. We will focus on an initial A parameter of about 1.0, roughly in the middle of this range. For larger values of A_0 the eccentricity plummets to values that are not easy to reconcile with the current eccentricity; for smaller values of A_0 the eccentricity does not get low enough.

The initial rotation state of the Moon is not known. Here we consider only the possibilities that the Moon's rotation was initially synchronous or initially nonsynchronous and asymptotic (Peale & Gold, 1965; Hut, 1981). We did not explore an initial 3:2 rotation state, because we think the synchronous solution is more plausible. For the 3:2 solution one must satisfactorily explain how the Moon was captured into the resonance and then explain how it escaped. For a constant Δt (Mignard) tidal model, the expression for the asymptotic rotation rate is (Levrard et al., 2007)

$$\frac{\omega'}{n} = \frac{N(e)}{\Omega(e)} \frac{2x}{1+x^2}, \quad (5.19)$$

where $x = \cos I'$, for the obliquity of the Moon I' , $N(e) = f_1(e)/\beta^{12}$, and $\Omega(e) = f_2(e)/\beta^9$. If the Moon's initial rotation was nonsynchronous and asymptotic, then when the Moon's rotation rate is close enough to synchronous the rotation rate becomes locked to synchronous. Here we assume that locking occurs if

$$\left| \frac{\omega'}{n} - 1 \right| < \frac{5}{8}\epsilon, \quad (5.20)$$

where $\epsilon = (3(B - A)/C)^{1/2}$ is the out-of-roundness parameter, and $A < B < C$ are the principal moments of inertia of the Moon. We do not know the value of ϵ when capture might have occurred; here we take the critical $(5/8)\epsilon$ to be 0.01. The evolution is not sensitive to this choice, because once the eccentricity begins to decrease, it decreases rapidly to small values.

The initial eccentricity of the Moon is also unknown. We presume here that the Moon formed from a giant impact with the Earth, and that the Moon formed roughly in the equatorial plane of the Earth with only moderate eccentricity. The

Moon-forming n -body simulations of Kokubo et al. (2000) found that the eccentricity of the initial lunar orbit ranged from 0.00 to 0.15. We think that these results should not be taken too literally since the physical state of the Moon-forming disk is not likely to be well represented by a collection of cold point particles. Instead it is likely that the Moon-forming disk was largely molten (Thompson & Stevenson, 1988), and that the Moon formed from cooler material being lost from the outer edge of the disk. But the orbit of the Moon in this formation scenario has not been studied, so there are no other hints as to the initial eccentricity of the lunar orbit. Another process may play a role in setting the initial orbital eccentricity: passage through the evection resonance. Even if the dance of the lunar orbit through the evection and eviction resonances as described in Touma & Wisdom (1998) does not occur (perhaps because the rate of tidal evolution is too large for capture to occur) it is likely that the eccentricity will suffer a non-adiabatic change on passing through the strong evection resonance. Touma & Wisdom (1998) found non-adiabatic eccentricities from 0.00 to 0.08 in this case. We assume $e = 0.05$ at $X = a/R_E = 6$, initially. We assume the initial inclination at this point is 10° , the initial rotation period of the Earth is 5 hours, and the initial obliquity of the Earth is 10° (Touma & Wisdom, 1994).

5.4 The Dissipative Lid Model

The model Moon consists of a plagioclase lid with initial thickness 10 km, above a magma ocean with initial thickness 200 km, above a solid interior. We assume that the magma ocean is convecting and the adiabatic temperature profile is characterized by a constant temperature T_f (the temperature at the top of the magma ocean). We take the initial value $T_f = 1573$ K. Tidal heating occurs solely in the lid and the temperature profile of the lid is modeled. The temperature at the surface of the lid is fixed at the equilibrium temperature, assumed to be 280 K. The temperature at the base of the lid is fixed to match the temperature of the magma ocean, T_f . We assume an initial thermal profile that is linear between these two values. The temperature profile in the lid evolves according to Fourier’s law of heat conduction.

As the temperatures in the interior of the lid evolve to above the solidus of plagioclase, heat is advected to the layers above by rising plagioclase liquid. The solidus of plagioclase is assumed to be $T_p = 1823$ K (Deer et al., 1996).

The thermal evolution in the lid is described by

$$\frac{\partial T}{\partial t} = \frac{2\kappa}{r} \frac{\partial T}{\partial r} + \frac{\partial}{\partial r} \left(\kappa \frac{\partial T}{\partial r} \right) + \frac{H}{\rho_l C_p} + \frac{\partial T}{\partial t} \Big|_{melt} \quad (5.21)$$

where r is the radius and t is the time, H is the local volumetric tidal heating rate, $\kappa = k/(\rho_l C_p)$ is the thermal diffusivity, C_p is the specific heat capacity, and k is the thermal conductivity. The density in the lid ρ_l is 2730 kg/m^3 . We use $C_p = 1256 \text{ J kg}^{-1} \text{ K}^{-1}$ and $\kappa = 10^{-6} \text{ m}^2 \text{ s}^{-1}$. This equation is just Fourier's law written in spherical coordinates, with the approximation that the heating and temperature are spherically symmetric (do not depend on angles).

The tidal heating rate in a homogeneous satellite at arbitrary eccentricity and obliquity was determined by Wisdom (2008). There it was shown that the tidal heating at large eccentricity can be dramatically larger than the conventional (e^2) formula gives. That calculation assumes a specific tidal model where the tidal bulge is delayed by a constant time lag (the Mignard model). For other tidal models presumably the form of the dissipation is somewhat different, but considering other uncertainties this form should be adequate. The heating rate is

$$\frac{dE}{dt} \Big|_{Tidal} = \frac{21}{2} \frac{k_2}{Q} \frac{GM^2 R^5 n}{a^6} \zeta(e, I'), \quad (5.22)$$

where k_2 and Q are the satellite's potential Love number and tidal dissipation factors, respectively, M is the mass of the Earth, R is the radius of the (homogeneous) Moon, n is the orbital mean motion, a is the semimajor axis of the orbit, e is the orbital eccentricity, I' is the obliquity of the satellite to the orbit, and

$$\zeta(e, I') = \frac{2}{7} \frac{f_0(e)}{\beta^{15}} - \frac{4}{7} \frac{f_1(e)}{\beta^{12}} \cos I' + \frac{1}{7} \frac{f_2(e)}{\beta^9} (1 + (\cos I')^2) \quad (5.23)$$

where $\beta = (1 - e^2)^{1/2}$.

We use the two-layer model from Peale & Cassen (1978) described and corrected in Appendix B to estimate the tidal heating as a function of radius in the lid. The local heating rate, averaged over angles, is given by:

$$H = \frac{\mu_L G^2 M^2 k_2^2 R^2 n \zeta(e, I')}{a^6 Q g^2} \left(-126(\alpha'_1)^2 + \frac{252}{5} \alpha'_1 \alpha'_2 - \frac{42}{5} (\alpha'_2)^2 - \frac{21}{5} (\alpha'_0)^2 - \frac{252}{5} (\alpha'_3)^2 \right). \quad (5.24)$$

where the surface acceleration on the Moon is $g = 1.62 \text{ m s}^{-2}$ and where μ_L is the rigidity of the lid, which we assume constant. We use $6.5 \times 10^9 \text{ N/m}^2$. This is a factor of 10 smaller than that used by Peale & Cassen (1978) based on seismic velocities in today's cold Moon; we use a lower rigidity because of the high temperatures in the lid during the early epoch. To some extent the choice of rigidity is arbitrary and offset by the uncertainty in the values of the tidal Q s of the early Earth and Moon. The temperature dependence of the rigidity of the plagioclase lid is ignored and the α'_i and k_2 functions are given in Appendix B.

The lid is varying in thickness δ_l and we parametrize depth in the lid using y which varies from 0 (at the surface) to 1 (at the base). Let $T(t, r) = T'(t, y)$, with $r = R - \delta_l y$ where R is the radius of the Moon, then the heat equation becomes

$$\frac{\partial T'}{\partial t} = -\frac{2\kappa}{\delta_l r} \frac{\partial T'}{\partial y} + \frac{\kappa}{\delta_l^2} \frac{\partial^2 T'}{\partial y^2} + \frac{\partial T'}{\partial y} \frac{y \dot{\delta}_l}{\delta_l} + \frac{H}{\rho_l C_p} + \frac{\partial T'}{\partial t} \Big|_{\text{melt}} \quad (5.25)$$

We introduce a discretization of the lid by dividing it into N spherical shells of thickness $\Delta r = \delta_l \Delta y$. Let T^i be the temperature in the i th shell corresponding to $y^i = i \Delta y$, where i runs from 0 at the surface to N at the base of the lid. Then Eq. 5.25 becomes

$$\frac{dT^i}{dt} = -\frac{2\kappa}{\delta_l r} \left(\frac{T^{i+1} - T^{i-1}}{2\Delta y} \right) + \frac{\kappa}{\delta_l^2} \left(\frac{T^{i+1} - 2T^i + T^{i-1}}{\Delta y^2} \right) + \left(\frac{T^{i+1} - T^{i-1}}{2\Delta y} \right) \frac{y \dot{\delta}_l}{\delta_l} + \frac{H}{\rho_l C_p}. \quad (5.26)$$

The melt migration term is handled separately.

As layers of the lid reach their melting temperature, portions of these layers begin to melt as heat continues to be added. The amount of melt mass depends on the latent heat of melting, $L = 5 \times 10^5 \text{ J/kg}$. These melted portions rise to the surface,

due to their positive buoyancy, bringing heat and mass with them. We model the ascent of this melt using a leaky dike model, where the melt loses a fraction of its heat and mass to each layer that it rises through. We varied the leak fraction from 0 to 1. The qualitative behavior is insensitive to this parameter; for the runs reported here we use 0.02 (for $N = 100$). Any heat remaining when the melt reaches the surface is assumed to be instantaneously radiated away. The remaining mass is deposited at the surface and the layers are redefined to account for the new mass distribution. As the melt is removed from a layer and redeposited in other layers or at the surface, the layers are redefined so that they remain equal in mass to the original layers. The temperature of the redefined layer is the mass-weighted average of the temperatures of the original layers that were incorporated into each layer.

The thermal evolution of the magma ocean is described by two equations. First,

$$4\pi(R - \delta_l)^2 k \left. \frac{dT}{dr} \right|_{base} + \dot{E}_r = -4\pi(R - \delta_l)^2 k \frac{1}{\delta_l} \left. \frac{dT}{dy} \right|_{base} + \dot{E}_r = C_p \rho_f (\dot{V}_f T_f + \dot{T}_f V_f) \quad (5.27)$$

where the left-hand side is heat conducted out of the magma ocean into the lid plus radiogenic heating \dot{E}_r , and the right-hand side is the change in heat content as a result of changing the volume V_f by both melting/freezing and changing the temperature in the magma ocean. We take $\rho_f = 3000 \text{ kg m}^{-3}$. We compute the radiogenic heating by extrapolating the chondritic abundances of ^{235}U , ^{238}U , ^{40}K , and ^{232}Th back to the time of formation of the Moon. We then multiply by the heat production per mass, the density, and the volume of the magma ocean and sum over the four isotopes. The half-lives, current abundances, and specific heat productions are given by Turcotte & Schubert (2002).

Second,

$$\frac{\dot{T}_f}{T_{sol}} f = -\frac{\dot{V}_l}{V_{fi}} = -4\pi(R - \delta_l)^2 \frac{\dot{\delta}_l}{V_{fi}} \quad (5.28)$$

which describes the fractional crystallization of the magma ocean. Here V_f is the volume of the magma ocean and V_l is the volume of the lid. We are assuming fractional solidification is linear between the magma ocean solidus and liquidus. Here, $T_{sol} = T_{fi} - T_s$ is the difference between the initial temperature in the magma ocean and the

solidus, and V_{fi} is the initial volume of the magma ocean. Each fractional increment in temperature change between those values, $\Delta T_f/T_{sol}$, results in a similar fractional change in the solid to liquid ratio of the magma ocean $\Delta V_f/V_{fi}$. The factor f is the proportion of plagioclase in the solidified portion of the melt; this is added to the base of the lid. We assume $f = 0.2$ (Snyder et al., 1992; Warren, 1986). As the magma ocean crystallizes, f gives the fraction of material that joins the lid and $1 - f$ gives the fraction that joins the solid interior at the base of the magma ocean.

The solidus of the fractionally solidifying magma ocean, T_s , is parameterized to fit the bulk lunar mantle solidus of Longhi (2003). As crystallization proceeds and solidification moves to shallower depths, the solidus moves to lower temperatures than the Longhi (2003) results as the remaining liquid composition evolves. This evolution is expressed in the final term of the solidus expression, calibrated to match temperatures calculated from the MELTS program (Ghiorso & Sack, 1995). We use

$$T_s = 2134 - 0.1724\epsilon - 1.3714 \times 10^{-4}\epsilon^2 - \frac{4.4}{0.2V_f/V_{fi} + 0.01}, \quad (5.29)$$

where T_s is the solidus in Kelvin and ϵ is the radius of the base of the lid in km.

The change in magma ocean depth δ_f can be related to the change in lid thickness using $\dot{V}_l = -f\dot{V}_f$:

$$\dot{\delta}_f = \frac{(1 - 1/f)(R - \delta_l)^2 - (R - \delta_l - \delta_f)^2}{(R - \delta_l - \delta_f)^2} \dot{\delta}_l = A_1 \dot{\delta}_l. \quad (5.30)$$

Then we can relate the rate of change in magma ocean volume \dot{V}_f to the rate of change of the lid thickness $\dot{\delta}_l$. The volume of the magma ocean is

$$V_f = \frac{4}{3}\pi(R - \delta_l)^3 - \frac{4}{3}\pi(R - \delta_l - \delta_f)^3 \quad (5.31)$$

and so

$$\dot{V}_f = -4\pi(R - \delta_l)^2 \dot{\delta}_l + 4\pi(R - \delta_l - \delta_f)^2 (\dot{\delta}_l + \dot{\delta}_f) = A_2 \dot{\delta}_l + A_3 \dot{\delta}_f. \quad (5.32)$$

Solving the above equations, we find that

$$\dot{\delta}_l = \frac{-4\pi(R - \delta_l)^2 \kappa \left. \frac{1}{\delta_l} \frac{dT}{dy} \right|_{base} + \dot{E}_r}{-4\pi(1/f)(V_f/V_{fi})(R - \delta_l)^2 T_{sol} + T_f(A_2 + A_1 A_3)} \quad (5.33)$$

and

$$\dot{T}_f = -\frac{T_{sol}}{f} \frac{4\pi(R - \delta_l)^2}{V_{fi}} \dot{\delta}_l. \quad (5.34)$$

Upon discretization, Eq. 5.33 becomes

$$\dot{\delta}_l = \frac{-4\pi(R - \delta_l)^2 \kappa (T^{N-1} - T^{N-2})/(\Delta y \delta_l) + \dot{E}_r}{-4\pi(1/f)(V_f/V_{fi})(R - \delta_l)^2 T_{sol} + T_f(A_2 + A_1 A_3)}. \quad (5.35)$$

We choose an effective $1/Q$ of the lid by averaging the $1/Q$ of the individual layers, as given in terms of the temperature of each layer by the Ojakangas-Stevenson formula,

$$\frac{1}{Q}(T_i) = \frac{1}{Q_{max}} + \left[\frac{1}{Q_{min}} - \frac{1}{Q_{max}} \right] \left(\frac{T_i}{T_p} \right)^n. \quad (5.36)$$

We set $Q_{max} = 100$, and let Q_{min} vary with the run. Experimentally, the parameter n ranges from 20 to 30 (Ojakangas & Stevenson, 1986); we use 25. We integrate Eqns. (5.26) and (5.35) as well as the equations for $\dot{\delta}_f$ and \dot{T}_f using the Bulirsch-Stoer algorithm, which has automatic step-size control. We carry out melt migration every 1 year. In our simulations we usually set the number of layers $N = 100$, but varied this parameter (and the corresponding leak fraction) to check that our results were insensitive to it.

Figure 5-1 shows the eccentricity of the lunar orbit versus the semimajor axis for a run in which $A_0 = 1.0$, the Earth's phase lag $\Delta t = 123$ minutes (with $k_2 = 0.97$), and the lunar $Q_{min} = 0.35$. These parameters were chosen to give a peak eccentricity near that required by the shape solution. There is considerable flexibility in the peak eccentricity; generally, increasing the dissipation in the Earth (larger Δt) gives a larger e_{max} , but this must be compensated by a smaller Q_{min} to match the current eccentricity of the lunar orbit. A more complete model would allow the Earth's k_2 and Q to vary with time, and would probably give different constraints on Q_{min} for the

Moon. Thus the very low value of Q_{min} should not be taken too seriously. We reduced Δt to 2.6 minutes (with $k_2 = 0.299$) when the orbit reached $30R_E$ to approximate the changes in these parameters, and so that the evolution to $60 R_E$ would take about 4.6 Gyr.

Figure 5-2 shows the tidal heating in the lid and compares it to the radiogenic heating in the magma ocean. Tidal heating peaks when the eccentricity is at a maximum and remains higher than the radiogenic heating rate until the eccentricity becomes small.

Figure 5-3 shows the evolution of the depth of the lid and the depth of the magma ocean as a function of time. In this model, the magma ocean solidifies at 272 Myr. The lid reaches a final thickness of 46 km. Radiogenic heating prolongs the magma ocean by about 55 Myr.

Figure 5-4 shows the temperature at four layers in the lid versus the logarithm of the time for this same run. The temperature at 10 km depth decreases below the closure temperature of 1000°C for zircons (Cherniak & Watson, 2003) at a time of about 9.1 Myr, at 15 km depth at a time of 32.5 Myr, at 20 km depth at a time of 63.2 Myr, at 25 km depth at a time of 100.2 Myr, and at 30 km depth at a time of 142.0 Myr. Our model cannot follow the temperatures in the lid once the magma ocean solidifies, so the graphs of the temperatures are terminated at this point. As discussed above, the closure time needs to be 90 to 121 Myr after lunar formation to match the zircon dates. Our model suggests that the dated zircon originates from a depth of approximately 25 km.

Figure 5-5 shows the temperature at four layers in the lid versus the logarithm of the time for a run in which the eccentricity and consequently the tidal heating has been set to zero. The thermal evolution is decoupled from the orbital evolution. We see that tidal heating affects the temperature of the shallowest layer, but not at depth. Thus even without tidal heating the dated zircon must originate at a depth of approximately 25 km. So the geochronology is consistent with our model if we focus on closure times at depth instead of solidification times of surface materials. Therefore, the age of the lunar breccias is not evidence for a high-eccentricity phase

of the lunar orbit.

Unfortunately, the above discussion of an evolution that matches the shape solution of Garrick-Bethell et al. (2006) was only achievable by increasing the time lag of the Earth's tidal response to Δt of 123 minutes (for an assumed k_2 of the Earth at that epoch of 0.97, the fluid Love number of the Earth). This is an unphysical value for the time lag. For the tidal model to correspond to a lagged tidal bulge, the time lag cannot exceed an eighth of the rotation period of the host planet (Efroimsky & Williams, 2009). This is because the tidal torque peaks for a 45° delay. The time lag that we chose does not satisfy this constraint. The rotation period of the early Earth was approximately 5.1 hours, when the Moon was at a semimajor axis of $6.8R_e$, where R_e is the radius of the Earth. Thus the tidal time lag is physically constrained to be less than 37 minutes. For this value of Δt , the peak eccentricity is only 0.31. The peak occurs at a semimajor axis of 16.5 Earth radii. The new evolution is shown in Figure 5-7.

Notice that the new evolution no longer passes through the shape solution of Garrick-Bethell et al. (2006). This means that the coupled thermal-orbital model cannot produce the orbit capable of matching the shape solution, since Figure 5-7 shows the evolution with maximum dissipation. For this maximal time lag, the magma ocean takes 272 Myr to freeze, as shown in Figure 5-8, compared to 217 Myr for the unphysical evolution that matches the shape solution. The calculated depth of the zircon dated by Nemchin et al. (2009) is not substantially modified, as can be seen by comparing Figure 5-9 with Figure 5-4.

5.5 Elastic Stability of the Shape Solution

We have found that a high eccentricity phase of lunar evolution can only carry the Moon through the synchronous shape solution for an unphysical choice of terrestrial dissipation parameters. Even if our model was able to produce an orbit to match the shape solution, as in Figure 5-1, the temperatures in the lid are close to a peak during this phase. So for the shape to record this hypothetical high eccentricity phase, in our

model we must rely on the rapid freezing of the melt as it reaches the surface of the Moon. As a large percentage of the lid is processed as melt during the high eccentricity phase, this may give a way of recording the shape even though tidal heating is also near a peak. Several questions arise, though, concerning the subsequent stability of the shape of this frozen lid. As the orbit continues to evolve to lower eccentricity and larger semimajor axis, the gravitational and centrifugal potentials change and so the lid must develop stress in order to maintain its shape. Is this stress below the breaking stress? Is the lid strong enough so that it can maintain its shape rather than elastically deform to subsequent hydrostatic shapes? We consider these questions in this section.

We follow the method described in Goldreich & Mitchell (2010), Matsuyama & Nimmo (2008), and Vening Meinesz (1947). First, recall (Garrrick-Bethell et al., 2006) that the average tidal and centrifugal potential at orbital eccentricity e and semimajor axis a gives rise to a triaxial distortion of the surface of the Moon with the distortions along the principal axes of

$$\Delta r_a = hcR \left(\frac{3}{4} X_{-3,2,2}(e) + \frac{5}{12} \right) \quad (5.37)$$

$$\Delta r_b = -hcR \left(\frac{3}{4} X_{-3,2,2}(e) - \frac{5}{12} \right) \quad (5.38)$$

$$\Delta r_c = -hcR \left(\frac{1}{2} X_{-3,0,0}(e) + \frac{1}{3} \right) \quad (5.39)$$

where R is the radius of the Moon, $h \approx 5/2$ is the fluid displacement Love number, $X_{i,j,k}$ are Hansen functions (Plummer, 1960), and

$$c = \left(\frac{R}{a} \right)^3 \frac{m_{Earth}}{m_{Moon}}. \quad (5.40)$$

We assume the \hat{a} axis points to the Earth (the Moon rotates synchronously), the \hat{c} axis is perpendicular to the orbit, and the intermediate \hat{b} axis completes a right hand basis set $(\hat{a}, \hat{b}, \hat{c})$. In terms of these principal displacements we calculate the displacement d of the surface of the rigid lid in terms of the colatitude θ measured

from the \hat{c} axis, and the angle γ measured from the \hat{a} axis. (The spherical coordinates are completed by a longitude ϕ measured from the meridian through the \hat{a} axis.) We find

$$d = R [\alpha(\cos^2 \theta - 1/3) + \beta(\cos^2 \gamma - 1/3)], \quad (5.41)$$

with

$$\cos \gamma = \sin \theta \cos \phi \quad (5.42)$$

and where

$$\alpha R = \Delta r_c - \Delta r_b \quad (5.43)$$

$$\beta R = \Delta r_a - \Delta r_b. \quad (5.44)$$

In terms of these, we can express the surface stresses:

$$\sigma_{\theta\theta} = \mathcal{A}\mu [\Delta\alpha (3 \cos^2 \theta + 1) + \Delta\beta (3 \cos^2 \phi (3 - \cos^2 \theta) - 5)], \quad (5.45)$$

$$\sigma_{\phi\phi} = \mathcal{A}\mu [\Delta\alpha (9 \cos^2 \theta - 5) + \Delta\beta (3 \cos^2 \phi (1 - 3 \cos^2 \theta) + 1)], \quad (5.46)$$

$$\sigma_{\theta,\phi} = \mathcal{A}\mu [\Delta\beta (3 \cos \theta \sin \phi \cos \phi)], \quad (5.47)$$

where

$$\mathcal{A} = \frac{2}{3} \left(\frac{1 + \nu}{5 + \nu} \right), \quad (5.48)$$

and where μ is the rigidity, and ν is Poisson's ratio, which we take to be 1/4. In these expressions we have written the stress in terms of $\Delta\alpha$ and $\Delta\beta$ which are the differences between α and β at a given orbit (a, e) minus the values of these parameters at the particular orbit given by the shape solution. We assume the stresses are zero at the shape solution. Other components of the stress are zero.

For a rigidity of $5 \times 10^{10} \text{ N m}^{-2}$, the stresses are approximately 1 kbar. This is approximately the breaking stress for the lunar lithosphere (Solomon, 1986). Thus the lithosphere may break, losing its shape. However, the rigidity is likely to be smaller than given because the temperatures are high. So we may be able to avoid breaking.

The Moon could also elastically respond to these stresses by changing its shape. Now we consider whether this is energetically favorable. Once the Moon's orbit has returned to a low eccentricity, the equilibrium shape will be different. If the Moon does not elastically change its shape to match the equilibrium shape, gravitational potential energy will be stored in the frozen-in shape. If the Moon's shape does change, elastic energy will be stored via the additional stresses in the lithosphere. Since the Moon will tend to the lowest energy configuration, we can judge which of these two outcomes will occur by comparing the stored gravitational energy to the stored elastic energy.

The elastic energy density is given by

$$\mathcal{E} = \frac{1}{2} \sum_{ij} \sigma_{ij} u_{ij} = \frac{1}{2} (\sigma_{\theta\theta} u_{\theta\theta} + \sigma_{\theta\theta} u_{\phi\phi}) + \sigma_{\theta\phi} u_{\theta\phi} \quad (5.49)$$

where the strains are given by

$$u_{\theta\theta} = \frac{\sigma_{\theta\theta} - \nu\sigma_{\phi\phi}}{2\mu(1+\nu)} \quad (5.50)$$

$$u_{\phi\phi} = \frac{\sigma_{\phi\phi} - \nu\sigma_{\theta\theta}}{2\mu(1+\nu)} \quad (5.51)$$

$$u_{\theta\phi} = \frac{\sigma_{\theta\phi}}{2\mu}. \quad (5.52)$$

We integrate over the volume of the lid to find the total elastic energy

$$E_e = \frac{2\pi\delta_l R^2 \mu}{1+\nu} \mathcal{A}^2 \left[(\Delta\alpha)^2 \left(\frac{8}{5}\nu + 8 \right) - \Delta\alpha\Delta\beta \left(\frac{8}{5}\nu + 8 \right) + (\Delta\beta)^2 \left(\frac{19}{40}\nu + \frac{55}{8} \right) \right]. \quad (5.53)$$

Next we compute the gravitational energy. The energy is

$$E_g = \int_V \bar{U}_T \rho r^2 \sin\theta dr d\theta d\phi, \quad (5.54)$$

where V is the volume of the Moon, and the average tidal potential is

$$\bar{U}_T(r, \theta, \phi) = n^2 r^2 \tilde{U}_T(\theta, \phi). \quad (5.55)$$

We find

$$\tilde{U}_T(\theta, \phi) = B_2(e)P_2(\cos \theta) + B_{2,2}(e)P_{2,2}(\cos \theta) \cos 2\phi, \quad (5.56)$$

where $P_2(x) = (3/2)x^2 - 1/2$ and $P_{2,2}(x) = 3(1 - x^2)$ and

$$B_2(e) = \frac{1}{2} + \frac{1}{3}X_{-3,0,0}(e) \quad (5.57)$$

$$B_{2,2}(e) = -\frac{3}{2}X_{-3,2,2}(e). \quad (5.58)$$

The Hansen coefficients are

$$X_{-3,2,2}(e) = 1 - \frac{5}{2}e^2 + \frac{13}{16}e^4 - \frac{35}{288}e^6 + \dots \quad (5.59)$$

$$X_{-3,0,0}(e) = (1 - e^2)^{-3/2}. \quad (5.60)$$

To compute the volume integral we make a change of variables from r to s

$$r = s(R + d(\theta, \phi)), \quad (5.61)$$

to get

$$E_g = n^2 \rho \int_0^1 ds \int_0^\pi d\theta \int_0^{2\pi} d\phi \left[\tilde{U}_T(\theta, \phi) s^4 (R + d(\theta, \phi))^5 \sin \theta \right] \quad (5.62)$$

$$= n^2 \rho R^4 \int_0^\pi d\theta \int_0^{2\pi} d\phi \left[d(\theta, \phi) \tilde{U}_T(\theta, \phi) \sin \theta \right], \quad (5.63)$$

where we have made a small d/R approximation, and used the fact that the angular integral of \tilde{U}_T is zero. Next using

$$d(\theta, \phi) = -h \frac{\bar{U}_T(R, \theta, \phi)}{g_{Moon}} = -\frac{hn^2 R^2}{g_{Moon}} \tilde{U}_T(\theta, \phi), \quad (5.64)$$

then

$$E_g = -\frac{n^4 \rho h R^6}{g_{Moon}} \int_0^\pi d\theta \int_0^{2\pi} d\phi \left[(\tilde{U}_T(\theta, \phi))^2 \sin \theta \right] \quad (5.65)$$

$$= -h c m_{Moon} n^2 R^2 \frac{3}{4\pi} \left[\frac{2}{5} (B_2(e))^2 + \frac{24}{5} (B_{2,2}(e))^2 \right]. \quad (5.66)$$

We compute the difference in the elastic energy from the stress-free shape solution $a = 22.9R_E$, $e = 0.49$, to the elastic energy at $a = 22.9R_e$, $e = 0.0$, and similarly for the gravitational energies. Using $\mu = 5 \times 10^{10}\text{Pa}$, $n = 1.35 \times 10^{-5} \text{ s}^{-1}$ (for $a \approx 20R_e$), $h = 5/2$, $\delta_l = 10^4\text{m}$, $m_{Moon} = 7.35 \times 10^{22}\text{kg}$, $c = 1.4 \times 10^{-4}$, we find that the elastic energy stored in going to zero eccentricity is $9.2 \times 10^{19}\text{J}$. The difference of the gravitational energy between these two orbital configurations is $1.7 \times 10^{21}\text{J}$. The ratio of the change in elastic energy to the change in the gravitational energy is about 0.053. This implies that the shape will deform elastically and lose memory of the shape solution. This elastic change in shape would be essentially instantaneous compared to the timescales of the evolution we are considering. The stresses that develop would then relax on a viscous timescale, which is very uncertain.

5.6 Conclusions

We have developed a simplified model for studying the coupled thermal-orbital evolution of the early Moon. The model assumes tidal heating occurs only in the lid and gives a temperature profile of the lid as a function of time. We assume that the variations of the k_2 and Q of the Moon dominate those of the Earth. Future work should include tidal dissipation and heat transfer in both the mantle and the lid, and model the variation in Earth's k_2 and Q .

The eccentricity of the lunar orbit can reach high values in this model. For small dissipation in the Moon (small Mignard A parameter), an initial eccentricity tends to grow. As the eccentricity grows to large values the tidal heating increases dramatically (Wisdom, 2008). This heats the Moon and causes the Q of the Moon to change due to its strong temperature dependence. With a small Q (large A parameter) the Moon's eccentricity begins to decay.

Parameters can be chosen that cause the orbit to pass close to the values of semi-major axis and eccentricity required by the synchronous shape solution of Garrick-Bethell et al. (2006). The parameters we had to choose are somewhat extreme, particularly the Δt of the Earth. Holding other parameters constant, the value of the

peak eccentricity is larger for larger dissipation in the Earth (larger Δt). To reach the eccentricity of Garrick-Bethell et al. (2006) we had to use a Δt of 123 minutes (for $k_2 = 0.97$). This time lag is larger than the maximal physically realistic value of 37 minutes.

Another severe problem is that the orbit matches the shape solution at a time when tidal heating of the plagioclase lid is at its peak. Garrick-Bethell et al. (2006) demonstrated that this shape does indeed match the current shape of the Moon, but whether it could have been preserved after formation at that eccentricity, while the heating rate is large, remains the question.

During the period capable of creating the crustal shape observed on the Moon today, assuming that the orbit corresponding to the shape solution can be reached, portions of the lunar crust were being melted through tidal dissipative heating, erupted to the surface, and quenched. We find that 89% of the lid is processed as melt in our model. The melt material that is placed on the surface solidifies and cools quickly, and may record the shape of the moon during the time of melt production. The peak of melt production is after the peak eccentricity, so it may be that the recorded shape will reflect a lower eccentricity than the peak. The rigidity of this surface and near-surface crust would be significant.

At the time of melt production, the lid is still underlain by a magma ocean which allows for elastic deformation of the lid. To determine whether the shape would be preserved until the present, we can make a simple energetics argument. If the Moon kept the shape that it froze in at the peak of eccentricity, when the orbit drops to low eccentricity, gravitational potential energy will be stored in the now non-equilibrium shape. If instead the Moon elastically deforms to match the new equilibrium shape, there will be elastic energy stored due to the stresses in the lid. By comparing the elastic and gravitational energies, we determined that the Moon will elastically deform and lose the shape it developed at the peak. So we conclude that if a magma ocean is still present at the high eccentricity phase during which the shape is frozen in (as in our model) then the shape could not be maintained as the orbit evolved to lower eccentricity. If we try to circumvent this conclusion by increasing the rigidity, then

we have shown that the lithosphere would break, again losing its shape.

Though the shape cannot be explained by a high eccentricity phase of the evolution of the lunar orbit, a high eccentricity phase is not excluded. The coupled thermal-orbital model presented here can give high eccentricities which subsequently damp to values low enough to reach the present eccentricity (whether or not some component of the lunar eccentricity is due to passage through the Jovian evection resonance).

At the peak of tidal heating the crust is melted internally and molten anorthosite erupted onto the lunar surface. These materials will cool quickly, so the closure age is roughly the same as the age of crystallization, which is less than 1 Myr after lunar formation. This short time lag is insufficient to explain the young ages measured in lunar rocks.

At depth in the crust materials will have their geochronological ages reset by heating over a far longer time period than the period of active melting. The crust is heated to temperatures below melting but above the zircon closure temperature of 1000 °C (Cherniak & Watson, 2003). If the lunar breccias originate at a range of depths, they will experience varying delays in cooling that could explain the range of ages measured. For the sample dated by Nemchin et al. (2009), we find that an origin at about 25 km depth is consistent with the measured age.

The lunar crust is highly brecciated from impacts, and rocks used for age determination may have originated at depth and been excavated by impacts. Wieczorek & Phillips (1999) estimates that the original excavation depths of the major basins range from 15 to 50 km, making the scenario of mid-crustal origin for these rocks plausible. The zircon dated by Nemchin et al. (2009) is from a melt breccia, sample 72215, and its depth of origin is unknown. However, Garrick-Bethell et al. (2009) demonstrated that sample 76535 was excavated from a depth of about 45 km without being brecciated or melted. This is further evidence that the dated zircon could have originated at large depth.

We find that a moderately high eccentricity phase of the lunar orbit is a robust feature of our model. We are only able to match the synchronous shape solution by stretching the dissipation in the Earth to unphysical values. However, even if the orbit

corresponding to the shape solution could be reached somehow, we conclude that it is unlikely that the Moon's shape during this epoch could persist to the present. Lunar geochronology of crustal breccias can be explained if they originate at depth.

5.7 Acknowledgements

We thank Bill McKinnon, Jonathan Mitchell, Francis Nimmo, Stan Peale, Darin Ragozzine, Dave Stevenson, Ben Weiss, Jim Williams, and Maria Zuber for helpful conversations.

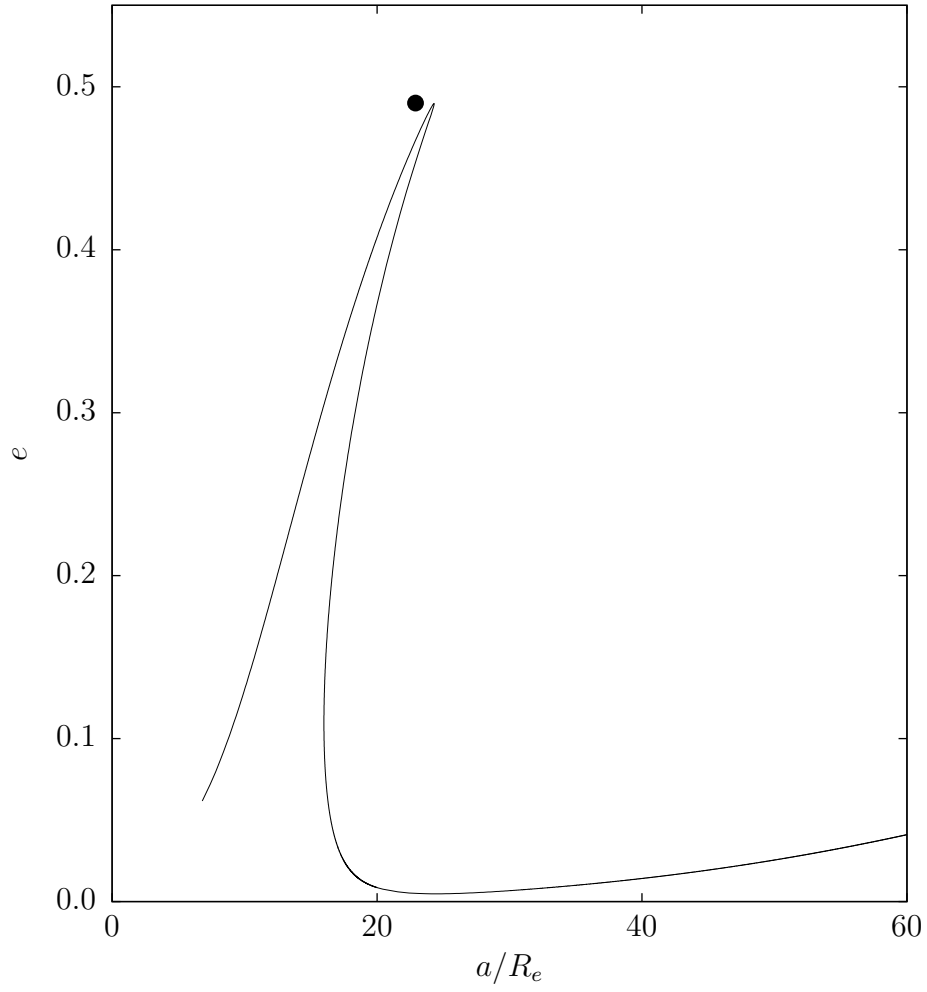


Figure 5-1: The eccentricity of the lunar orbit plotted versus the semimajor axis of the orbit, for the dissipative lid model. For reference, the dot shows the orbit that gives the solution to the shape problem for synchronous rotation.

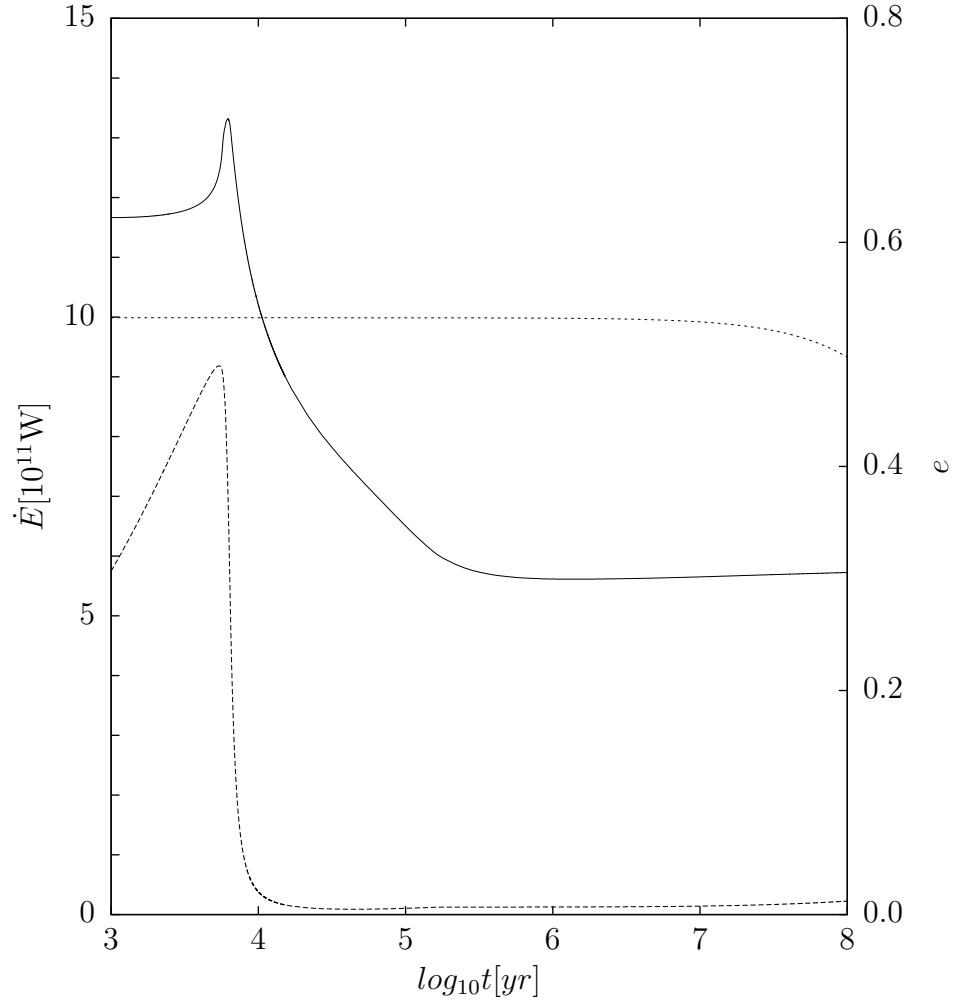


Figure 5-2: The tidal heating rate in the lid plotted versus time (solid line, see left axis). The radiogenic heating rate in the magma ocean is shown as a dotted line. The dashed line shows the orbital eccentricity versus time (see right axis).

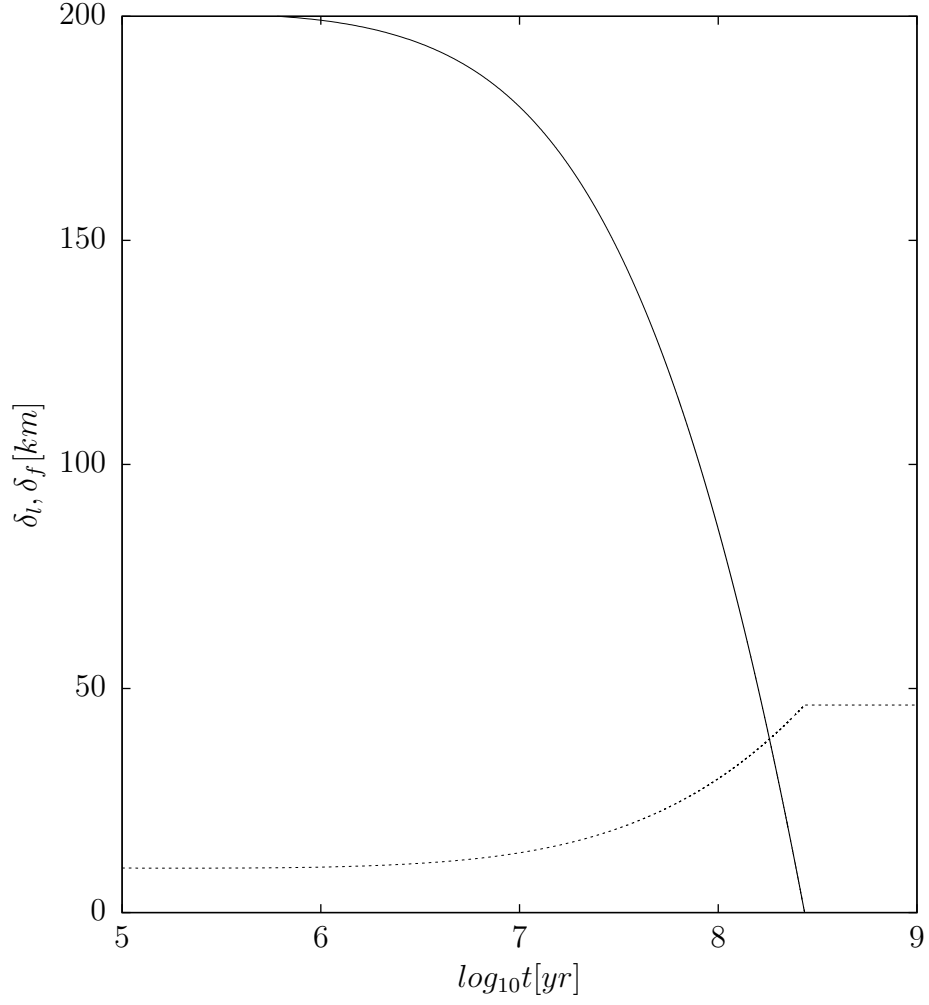


Figure 5-3: The depth of the magma ocean δ_f (solid) and the depth of the lid δ_l (dotted) plotted versus the logarithm of the time. In this model the magma ocean disappears after about 217 Myr and the lid reaches its full depth of about 46.3 km.

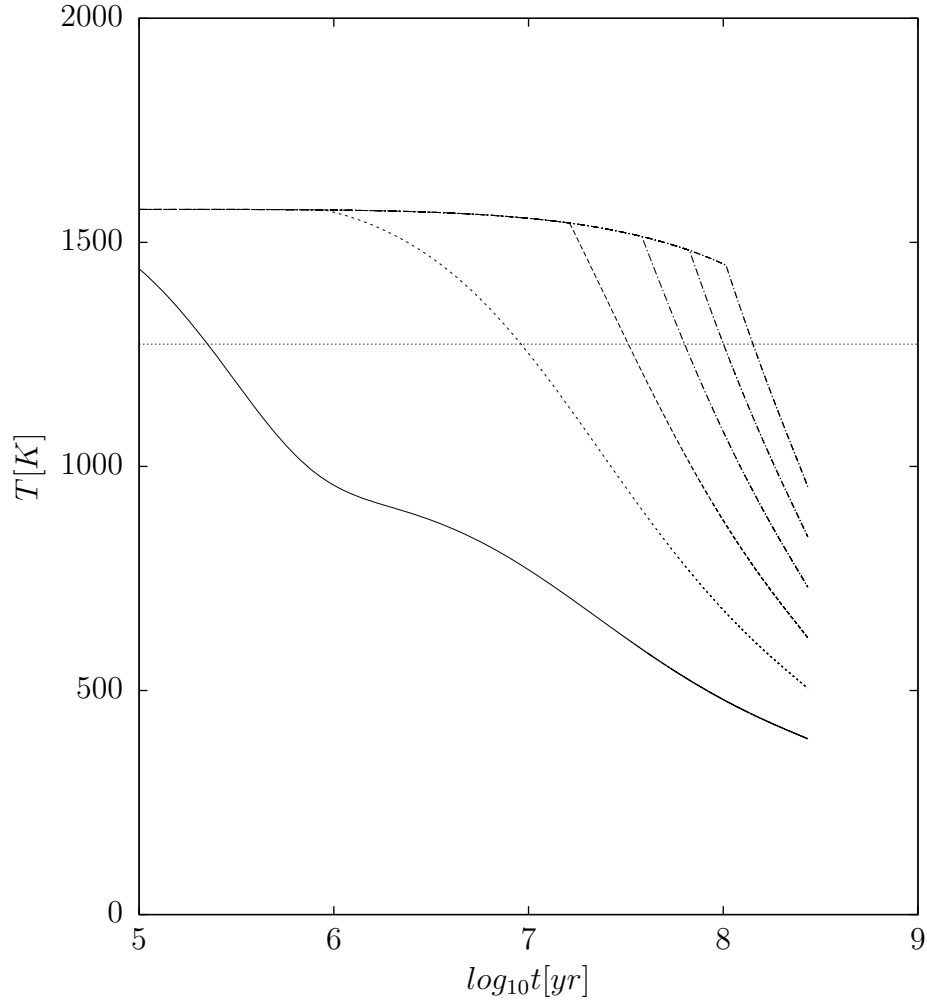


Figure 5-4: The temperature at six layers in the lid plotted versus the logarithm of the time. The eccentricity behavior is as shown in Figure 5-1. The depths of each layer are 5 km, 10 km, 15 km, 20 km, 25 km, and 30 km. The temperature increases with depth. The horizontal line indicates the approximate closure temperature of zircon.

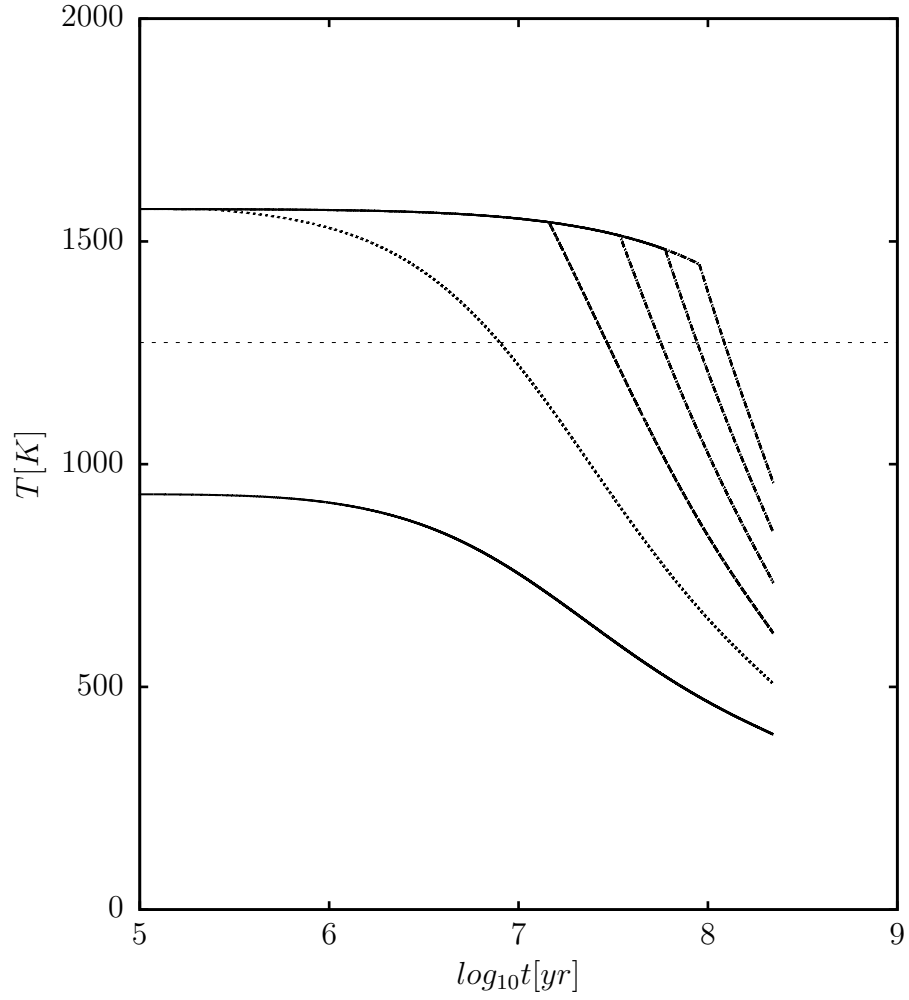


Figure 5-5: The temperature at six layers in the lid plotted versus the logarithm of the time. Here the eccentricity and consequently the tidal heating are set to zero. The depths of each layer are 5 km, 10 km, 15 km, 20 km, 25 km, and 30 km. The temperature increases with depth. The horizontal line indicates the approximate closure temperature of zircon.

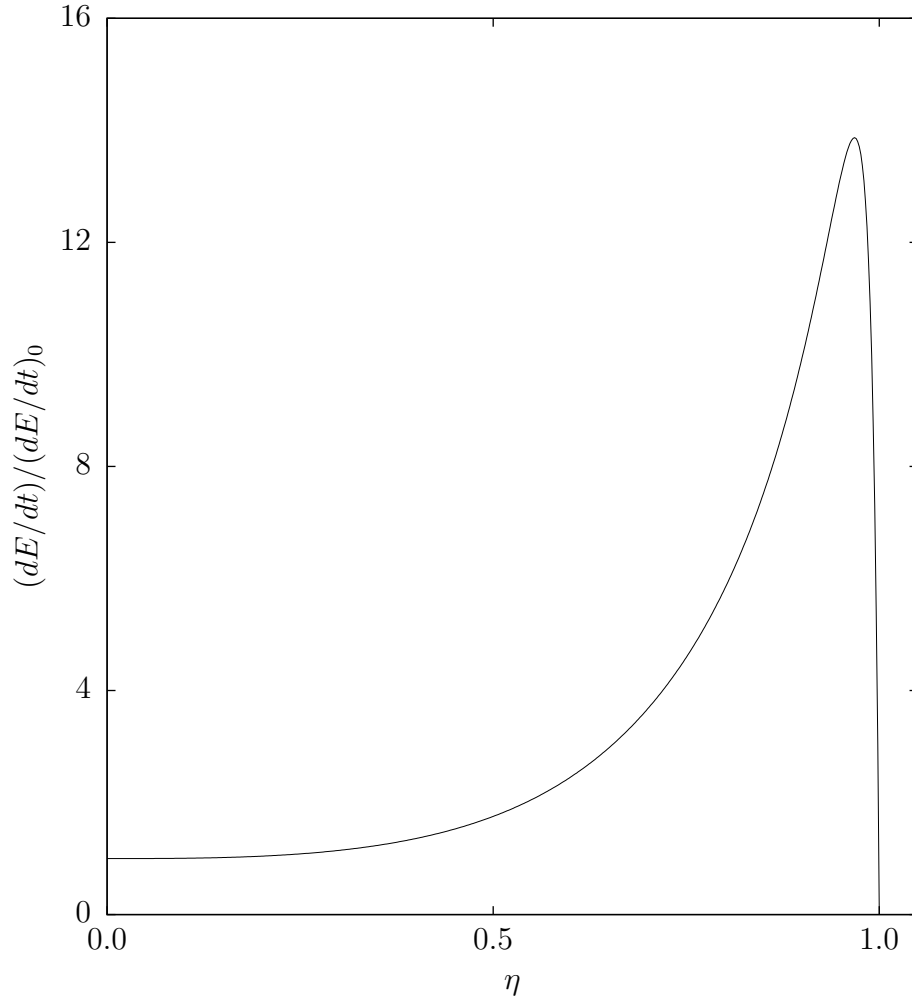


Figure 5-6: Recalculation of Figure 1 from Peale, Cassen, and Reynolds (1979). This shows the ratio of the total dissipation in the two-layer model to the total dissipation in a homogeneous body ($\eta = 0$) plotted versus η , the fractional thickness of the interior.

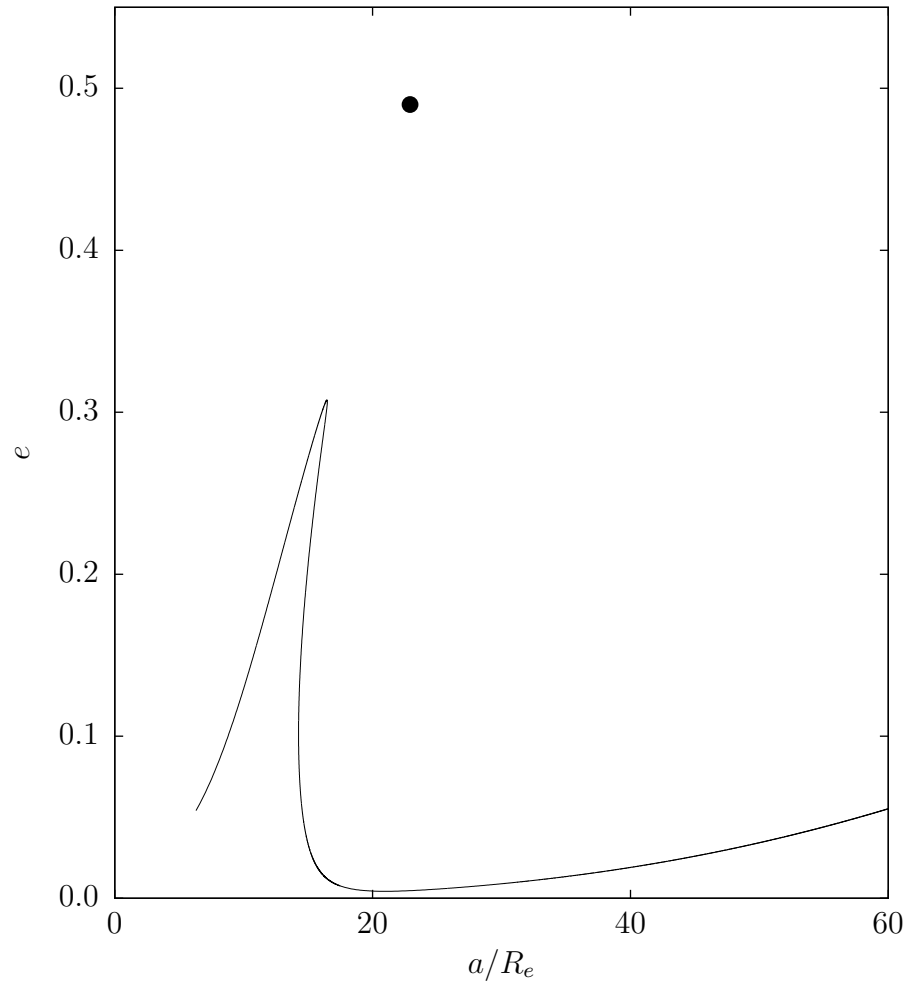


Figure 5-7: The eccentricity of the lunar orbit plotted versus the semimajor axis of the orbit, for maximum realistic dissipation parameters. For reference, the dot shows the orbit that gives the solution to the shape problem for synchronous rotation.

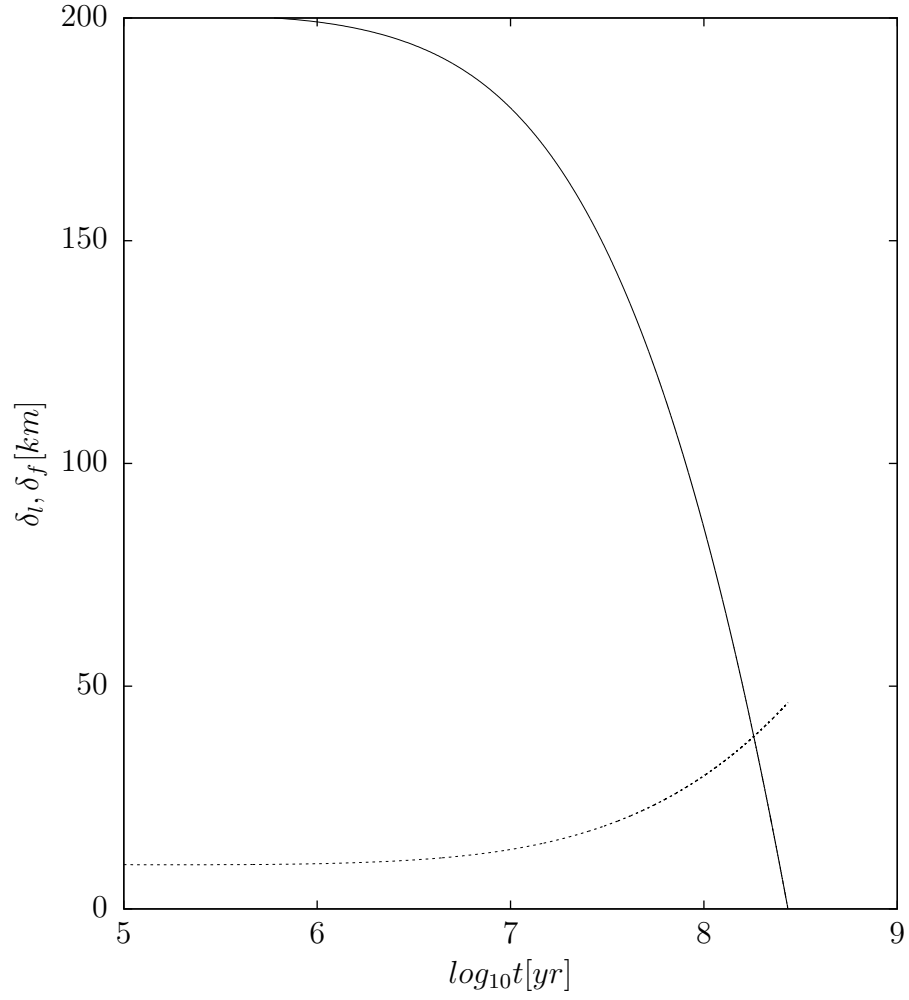


Figure 5-8: The depth of the magma ocean δ_f (solid) and the depth of the lid δ_l (dotted), plotted versus the logarithm of the time using maximum realistic dissipation parameters. The magma ocean disappears after about 272 Myr, and the lid reaches its full depth of about 46.3 km.

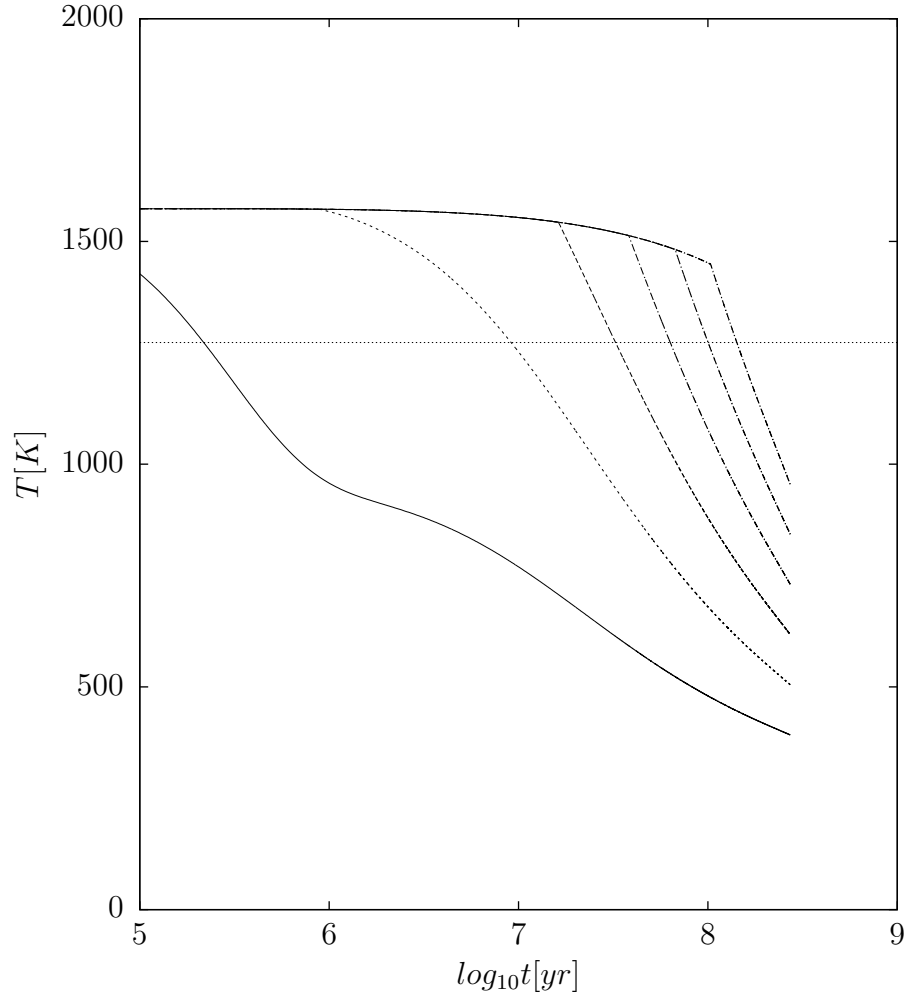


Figure 5-9: The temperature at six layers in the lid plotted versus the logarithm of the time, for maximum realistic dissipation parameters. The depths of each layer are 5 km, 10 km, 15 km, 20 km, 25 km, and 30 km. The temperature increases with depth. The horizontal line indicates the approximate closure temperature of zircon. The temperatures are not significantly different from the temperatures in Figure 5-4.

Chapter 6

Precession of the Lunar Core

Goldreich (1967) showed that a lunar core of low viscosity would not precess with the mantle. We show that this is also the case for much of lunar history. But when the Moon was close to the Earth the Moon's core was forced to follow closely the precessing mantle, in that the rotation axis of the core remained nearly aligned with the symmetry axis of the mantle. The transition from locked to unlocked core precession occurred between 26.0 and 29.0 Earth radii, thus it is likely that the lunar core did not follow the mantle during the Cassini transition. Dwyer & Stevenson (2005) suggested that the lunar dynamo needs mechanical stirring to power it. The stirring is caused by the lack of locked precession of the lunar core. So, we do not expect a lunar dynamo powered by mechanical stirring when the Moon was closer to the Earth than 26.0 to 29.0 Earth radii. A lunar dynamo powered by mechanical stirring might have been strongest near the Cassini transition.

6.1 Introduction

Paleomagnetic measurements of lunar rocks show magnetic remanence most easily explained by a long-lived early lunar dynamo (Garrrick-Bethell et al., 2009). Dwyer & Stevenson (2005) argued that the only plausible driving force for an early lunar dynamo is mechanical stirring of the liquid core due to the relative motion between the core and mantle. This driving mechanism is only an option if the core of the

Moon does not precess along with the mantle.

The orbit of the Moon is inclined by about 5 degrees to the ecliptic and regresses with an 18.6 year period. The rotation of the Moon is synchronous with the orbital motion. The spin axis of the solid Moon is tilted with respect to the ecliptic and its precession is locked to the precession of the orbit: the Moon is in a Cassini state (Peale, 1969). Goldreich (1967) showed that a liquid lunar core of low viscosity would not precess with the mantle; the spin axis of the lunar core is nearly normal to the ecliptic. For the Earth, the core precesses with the mantle because of the inertial coupling mechanism (Poincaré, 1910a; Toomre, 1966). That is, the spin axis of the Earth's fluid core is nearly parallel to the spin axis of the mantle, and both regress with a period of roughly 26,000 years. Goldreich showed that the inertial coupling mechanism fails for the Moon, arguing that the ellipticity of the core-mantle boundary was smaller than required to cause the core to precess with the mantle today. We address here whether the lunar core precessed with the mantle at earlier epochs.

If the core is locked to the mantle (as for the Earth), then the spin axis of the core is nearly aligned with the symmetry axis of the core-mantle boundary. If the spin axis of the core is slightly displaced from this configuration then the spin axis precesses about the symmetry axis with the core precession frequency ω_c (Touma & Wisdom, 2001)

$$\omega_c = \omega f_c (C/C_m), \quad (6.1)$$

where ω is the rotation frequency of the Moon, f_c is the core flattening, and C/C_m , the ratio of the polar moment of inertia of the Moon to that of the mantle (the Moon excluding the core), is approximately 1 for the Moon. The core flattening is given by $f_c = (C_c - A_c)/C_c$ where A_c and C_c are the smallest and largest moments of inertia of the core. If the core is not locked to the mantle, then the spin axis is no longer closely aligned with the core-mantle boundary symmetry axis.

Whether the core is locked to the mantle depends on the relative frequencies of the precession of the core and the mantle (Poincaré, 1910a). If the mantle precesses faster than the core $\omega_m > \omega_c$, as is the case today, the core will not follow the mantle.

However, if the precession frequency of the core is larger than that of the mantle $\omega_c > \omega_m$, the core and mantle will precess together, with the core oscillating around the symmetry axis of the mantle with the frequency ω_c . Since C/C_m is approximately unity, we may restate the condition for locking in terms of the flattening. Locking occurs for core flattening larger than ω_m/ω . In the limit of very small flattening, the rotation axis of the core is perpendicular to the ecliptic plane.

Goldreich argued that the lunar core flattening is too small today for the inertial coupling mechanism to lock the core to the mantle. But earlier in the lunar history, the Moon was closer to the Earth, and rotated more rapidly, so the Moon was subject to greater tidal and centrifugal forces. Thus the lunar core flattening was larger in the past.

Here, we model the past ellipticity of the lunar core-mantle boundary and compare the estimated precession rate of the core to that of the mantle to determine when the lunar core was locked to the mantle.

6.2 Model and Results

We assume that the Moon rotates synchronously with its orbital motion. We take the orbit of the Moon to be circular, as the effect of eccentricity on the precession of the Moon is small (Touma & Wisdom, 1994). The Moon's orbit is inclined and precessing. For the history of the lunar orbit under these assumptions we use the model of Touma & Wisdom (1994). They examined various tidal models and found that the basic evolution did not depend on the tidal model. Here we use the Mignard model from that work. We approximate the density in the Moon by a two layer model, with constant density in the mantle and in the core. The core is presumed to be fluid.

The surface and core-mantle boundary are out of round: we describe these surfaces by the shape functions

$$r_i(\theta, \phi) = a_i(1 + \epsilon_{20}^i P_2(\cos \theta) + \epsilon_{22}^i P_{22}(\cos \theta) \cos(2\phi)), \quad (6.2)$$

where $P_2(x) = (3x^2 - 1)/2$ and $P_{22}(x) = 3(1 - x^2)$, and θ is the colatitude, ϕ is the longitude measured from the sub-Earth point, and a_i is the mean radius. The shape function r_i gives the radius of the surface as a function of colatitude and longitude. The label i is either “ c ” for core or “ s ” for surface. We can relate the flattening to the shape parameter $f_c = -(3/2)\epsilon_{20}^c$. This was derived by performing the integrals for the principal moments.

The origin of the low order shape and moments of the Moon is still discussed. The “fossil bulge” hypothesis asserts that the shape was determined at an early epoch and has been constant since that epoch. Explaining that shape has been difficult however; one possibility is that the shape formed when the Moon was in a moderately eccentric orbit (Garrrick-Bethell et al., 2006), though Meyer et al. (2010) argue against this scenario. We adopt the fossil bulge hypothesis, though it is unclear at what time (what lunar semimajor axis) the fossil bulge was established. At earlier epochs we presume the shape of the mantle of the Moon was approximately hydrostatic.

We consider two simplified models. In one model, the “non-hydrostatic mantle” model, we consider the shape of the mantle (its surface) to be responsible for the low order moments of the Moon, and find the shape of the core-mantle boundary by assuming its shape is hydrostatic, i.e. that the total potential is constant on that surface. In the other model, the “hydrostatic mantle” model, we determine both the shape of the surface and the shape of the core-mantle boundary by assuming they are both hydrostatic. We expect the hydrostatic model to be applicable early in the lunar evolution, and the non-hydrostatic model to be applicable later (presuming the fossil bulge hypothesis), though the point of transition is unclear.

The potential acting on a particular mass element in the Moon with radius r , colatitude θ , and longitude ϕ is given by

$$U = U_{rot} + U_{tidal} + U_m, \quad (6.3)$$

where the rotational (centrifugal) potential is

$$U_{rot} = \frac{1}{3}\omega^2 r^2 P_2(\cos \theta), \quad (6.4)$$

the tidal potential is

$$U_{tidal} = -\frac{GMr^2}{r_p^3} P_2(\cos \alpha), \quad (6.5)$$

and U_m is the potential due to the mass distribution in the Moon, and where α is the angle of the mass element from the Earth-Moon line measured from the center of the Moon, ω is the rotational/orbital frequency of the Moon, G is the gravitational constant, M is the mass of the Earth, and $r_p = a$ is the semimajor axis of the Moon (not to be confused with a_c and a_s).

For a synchronous Moon with zero obliquity in a circular orbit, the angle α is given by $\cos \alpha = \sin \theta \cos \phi$. But the Moon has a small non-zero inclination and obliquity. The tidal potential thus has periodic variations, on an orbital period. The average tidal potential governs the shape, because variations in hydrostatic shape occur on a timescale long compared to the variations in the tidal potential. The average tidal potential differs from that for zero obliquity by terms of second order in the small obliquity. For most of the history of the lunar orbit, these periodic variations in the tidal potential are ignorable. An exception occurs during the Cassini transition, which occurs near $33.4R_e$ (Ward, 1975; Wisdom, 2006), during which the Moon briefly develops large obliquity. Taking account of obliquity, the average tidal potential is

$$U_{tidal} = -\frac{GMr^2}{r_p^3} \left[P_{20}(\cos \theta) \left(-\frac{1}{2} + \frac{3}{4}(\sin \varepsilon)^2 \right) + P_{22}(\cos \theta) \cos(2\phi) \left(\frac{1}{4} - \frac{1}{16}(\sin(\varepsilon))^2 - \frac{1}{4}(\sin(\varepsilon/2))^2 \right) \right] \quad (6.6)$$

where ε is the obliquity of the spin axis to the orbit. This can be derived by first computing $\cos \alpha$ for an arbitrary point in the synchronously rotating but oblique Moon. Then form the potential, average it over time, and reexpress the position in terms of the Legendre polynomials. For the obliquity as a function of semimajor axis we use the results of Wisdom (2006).

For a homogeneous body (uniform density ρ_m) with surface shape function r_s , mean radius a_s , and parameters ϵ_{20}^s and ϵ_{22}^s , the exterior potential is (Jefferys, 1976)

$$U_{ext}^s(r, \theta, \phi) = -\frac{4}{3}\pi G \rho a_s^3 \left(\frac{1}{r} + \frac{3}{5} \frac{a_s^2}{r^3} \epsilon_{20}^s P_2(\cos \theta) + \frac{3}{5} \frac{a_s^2}{r^3} \epsilon_{22}^s P_{22}(\cos \theta) \cos(2\phi) \right), \quad (6.7)$$

and the interior potential is

$$U_{int}^s(r, \theta, \phi) = -\frac{4}{3}\pi G \rho a_s^3 \left(\frac{3a_s^2 - r^2}{2a_s^3} + \frac{3}{5} \frac{r^2}{a_s^3} \epsilon_{20}^s P_2(\cos \theta) + \frac{3}{5} \frac{r^2}{a_s^3} \epsilon_{22}^s P_{22}(\cos \theta) \cos(2\phi) \right), \quad (6.8)$$

These expressions are correct to first order in the shape parameters. Note that at the radius $r = a_s$ the exterior potential and the interior potential agree to first order in the shape parameters, so at this order we can use the two potentials interchangeably.

For a body that has, in addition, an out-of-round core, we add to this potential the potential due to a core of additional density $\Delta\rho = \rho_c - \rho_m$. The additional potential exterior to the core-mantle boundary is

$$U_{ext}^c(r, \theta, \phi) = -\frac{4}{3}\pi G \Delta\rho a_c^3 \left(\frac{1}{r} + \frac{3}{5} \frac{a_c^2}{r^3} \epsilon_{20}^c P_2(\cos \theta) + \frac{3}{5} \frac{a_c^2}{r^3} \epsilon_{22}^c P_{22}(\cos \theta) \cos(2\phi) \right), \quad (6.9)$$

and the additional potential interior to the core-mantle boundary is

$$U_{int}^c(r, \theta, \phi) = -\frac{4}{3}\pi G \Delta\rho a_c^3 \left(\frac{3a_c^2 - r^2}{2a_c^3} + \frac{3}{5} \frac{r^2}{a_c^3} \epsilon_{20}^c P_2(\cos \theta) + \frac{3}{5} \frac{r^2}{a_c^3} \epsilon_{22}^c P_{22}(\cos \theta) \cos(2\phi) \right). \quad (6.10)$$

The potential U_m at the core-mantle boundary is

$$U_m^{cmb}(\theta, \phi) = U_{int}^s(r_c(\theta, \phi), \theta, \phi) + U_{ext}^c(r_c(\theta, \phi), \theta, \phi), \quad (6.11)$$

and the potential U_m at the surface is

$$U_m^{surf}(\theta, \phi) = U_{ext}^s(r_s(\theta, \phi), \theta, \phi) + U_{ext}^c(r_s(\theta, \phi), \theta, \phi). \quad (6.12)$$

The total potential on these surfaces in addition includes the rotational and tidal

contributions.

We solve two problems: (1) given the shape parameters for the mantle determined by matching the observed gravitational moments, find the hydrostatic shape of the core-mantle boundary (we call this the “non-hydrostatic mantle” case), and (2) find the hydrostatic shape of both the mantle and the core (we call this the “hydrostatic mantle” case). We solve both models as a function of the Earth-Moon distance (semimajor axis of the assumed circular orbit).

We use two methods of solution. In one method we define a function that is nonzero and positive if the surfaces that should be hydrostatic are non-hydrostatic. This function takes a number of differences of the potential at different colatitudes and longitudes, squares them, and sums over all differences taken. We then find the shape parameters by minimizing this function over the shape parameters, using the Nelder-Mead downhill simplex method. In the second method, we truncate the potentials at first order in the shape parameters. We then project the potentials (which are functions of colatitude and longitude) onto the second degree spherical harmonics, $P_2(\cos \theta)$ and $P_{22}(\cos \theta) \cos(2\phi)$, by performing the integrals of the products of these functions, the total potential on each surface, and the surface area element. The result is a set of linear equations in the shape parameters that we solved analytically, but are too complicated to display. The shape parameters determined by the two methods agree to first order in the shape parameters, about four or five digits.

Williams et al. (2009) found that the ratio of the core moment to the total moment of inertia of the Moon C_c/C was $1.2 \pm 0.4 \times 10^{-3}$. In Figure 6-1, we show the core flattening calculated for the hydrostatic and non-hydrostatic mantle models as a function of the core density, for three values of C_c/C . We vary the core density from 4700 kg/m^3 (Fe-FeS eutectic) to 8100 kg/m^3 (pure Fe) (Kuskov & Kronrod, 1998). The flattening is not sensitive to the assumed C_c/C as demonstrated in the figure (though the radius of the core does depend on the assumed C_c/C).

For the non-hydrostatic mantle model we use

$$C_{20} = \frac{(B + A)/2 - C}{ma_e^2} = -2.04 \times 10^{-4} \quad (6.13)$$

and

$$C_{22} = \frac{B - A}{4ma_e^2} = 2.24 \times 10^{-5}, \quad (6.14)$$

determined from the libration parameters (Dickey et al., 1994). These correspond to mantle shape parameters of $\epsilon_{20}^s = -3.40 \times 10^{-4}$ and $\epsilon_{22}^s = 3.74 \times 10^{-5}$, ignoring small contributions from the core. Here m is the mass of the Moon, and a_e is the mean equatorial radius. The principal moments of the Moon are $A < B < C$.

There is marginal detection of the ellipticity of the lunar core-mantle boundary from laser ranging analysis (Williams et al., 2009). They find the flattening of the core-mantle boundary to be $f_c = 2.0 \pm 2.3 \times 10^{-4}$. The large error bar is argued to be more a reflection of a correlation in the result with other uncertain parameters rather than uncertainty in the flattening. Williams et al. (2009) notes that the core flattening is not hydrostatic (by comparing the result to the expected hydrostatic core-mantle boundary with a hydrostatic mantle). Of course, the fact that the mantle is currently non-hydrostatic is well known. We can see from Figure 6-1 that the observed flattening agrees well with the hydrostatic flattening expected of the core-mantle boundary inside a non-hydrostatic mantle (the non-hydrostatic mantle model).

Emboldened by this success, we now calculate the hydrostatic flattening of the core-mantle boundary as the lunar orbit evolves. Figure 6-2 shows the results. The parameters we adopt are: $a_c = 350$ km, $a_s = 1738$ km, $\Delta\rho = 4400$ kg/m³, $\rho = 3300$ kg/m³. For the present lunar orbit we find, in the hydrostatic mantle case, $\epsilon_{20}^c = -1.01 \times 10^{-5}$; and, for the non-hydrostatic mantle case, we find $\epsilon_{20}^c = -1.39 \times 10^{-4}$. These correspond to core flattening parameters of $f_c = 1.52 \times 10^{-5}$ and $f_c = 2.09 \times 10^{-4}$. We see that at large semimajor axes the precession of the fluid core is not coupled to the precession of the mantle, but at small semimajor axes the two precess together. The point of transition is uncertain ($26.0R_e$ - $29.0R_e$, where R_e is the radius of the Earth), because the semimajor axis at which the Moon developed its nonhydrostatic shape is uncertain. The time is much more uncertain, as the timescale for tidal evolution early in the lunar history is unknown. But assuming average tidal parameters such that the orbit of the Moon reaches the Earth 4.5 Gyr ago, these lunar

semimajor axes are reached in less than 40 Myr. By comparison, the lunar sample 76535 shows evidence of a lunar magnetic field 4.2-4.3 Gyr ago (Garrrick-Bethell et al., 2009).

Requiring the core to be decoupled from the mantle at that time allows us to place a lower limit on the average rate of tidal evolution during this epoch. The rate of tidal evolution is no slower than a factor of about 6 compared to the average tidal evolution rate. For the constant Δt Mignard model this implies $\Delta t > 0.44$ minutes, compared to today's value of about 10 minutes.

The Cassini transition occurs at around $33.4R_e$. We see that it is likely that the core did not follow the mantle during the Cassini transition. Since the obliquity of the Moon is large during the Cassini transition, we may speculate that there was a large magnetic field during the transition because of the large stirring (presuming the hypothesis of Dwyer and Stevenson, 2005). So we might expect nonzero lunar paleomagnetic measurements to cluster near the time of the Cassini transition, perhaps allowing us to constrain that time. At present there are not enough paleomagnetic data to assess this hypothesis.

We have constructed a simple model to study the transition between locked and unlocked core and mantle, described in Appendix C. The behavior of the offset between the spin axes of the core and mantle is shown in Figure: C-1. We see that the spin axes can have large misalignment during the transition, which may be an additional epoch of large stirring.

6.3 Conclusion

The fluid core of the Moon does not precess with the mantle of the Moon. We have shown that this is also the case for much of lunar history. But when the Moon was close to the Earth the core followed the mantle. The transition occurred at $26.0R_e$ - $29.0R_e$.

Dwyer & Stevenson (2005) suggested that the lunar dynamo needs mechanical stirring to power it. The stirring is caused by the lack of locked precession of the

lunar core. So, we do not expect a lunar dynamo powered by mechanical stirring when the Moon was close to the Earth. The transition to unlocked spin axes and the Cassini transition are both events that would cause large stirring in the core and are therefore both candidates for sparking the onset of a core dynamo.

6.4 Acknowledgments

We thank Stan Peale, Dave Stevenson, Ben Weiss, and Jim Williams for helpful conversations.

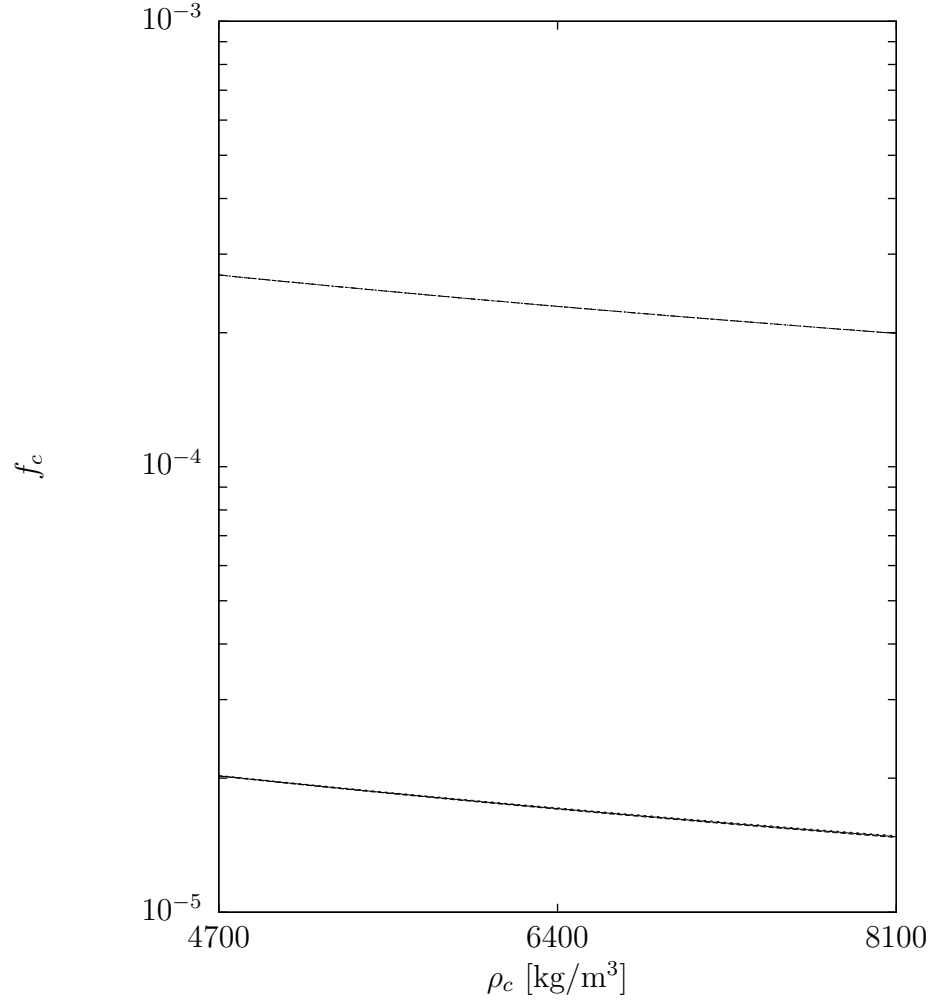


Figure 6-1: The flattening of the lunar core plotted versus the assumed density of the core, for fixed core moment of inertia. For the non-hydrostatic mantle model, three curves are plotted. These three curves are the upper three on the plot and indistinguishable from each other. These three curves correspond to different core moments: $C_f/C = 0.8 \times 10^{-3}$, 1.2×10^{-3} and 1.6×10^{-3} . Similarly, the lower curves (also indistinguishable) show the results for the hydrostatic mantle model and the same core moment values.

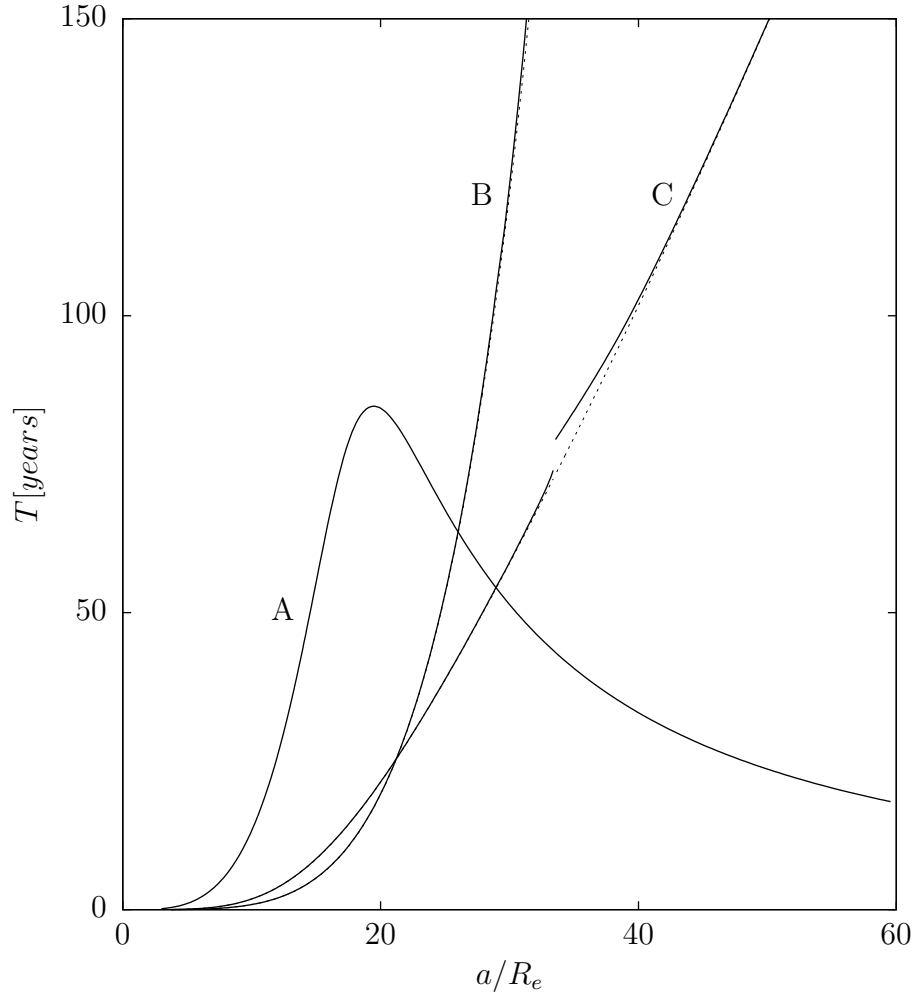


Figure 6-2: The period of precession of the lunar orbit and lunar mantle (line A), of the lunar core in the “hydrostatic mantle” model (lines B), and of the lunar core in the “non-hydrostatic mantle” model (lines C), plotted as a function of lunar semimajor axis in Earth radii. For lines *B* and *C* the solid line takes into account the forced obliquity of the Moon, whereas the dashed line assumes zero obliquity. The gap in the non-hydrostatic mantle model occurs at the Cassini transition. The core precesses with the mantle when the Moon is close to the Earth; and the lunar core decouples from the mantle at large semimajor axis. The point of transition depends on the model.

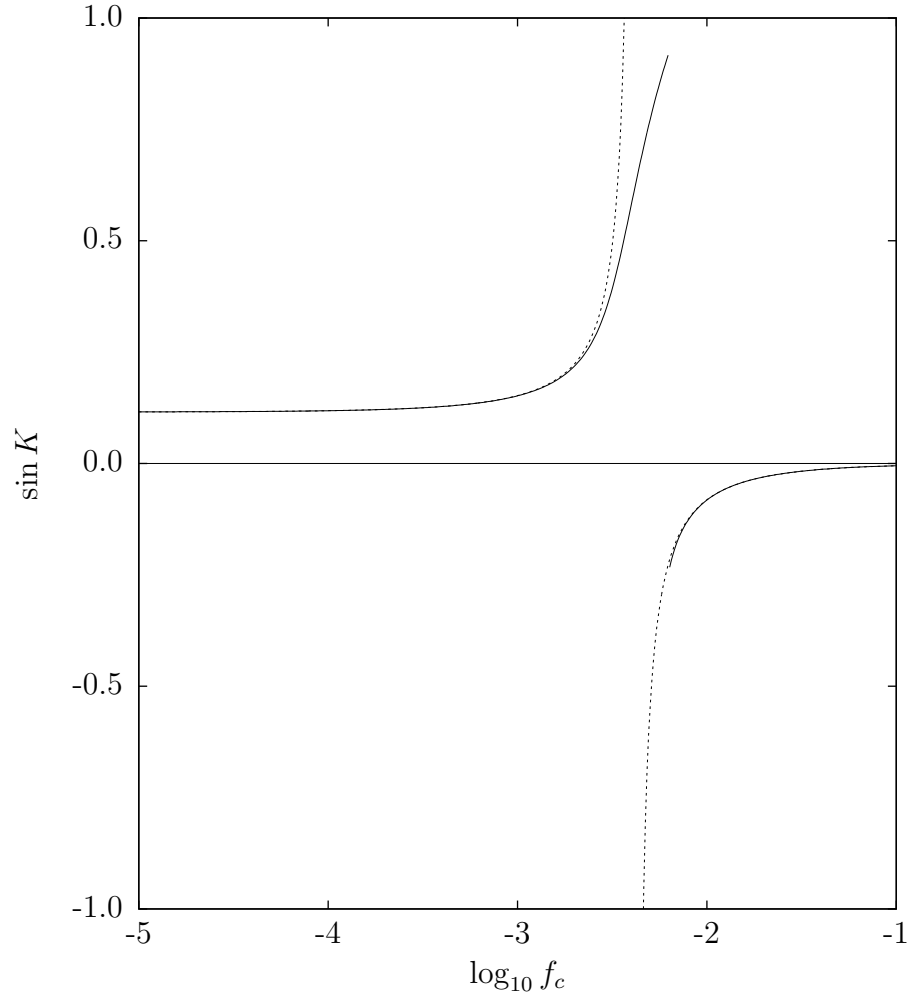


Figure 6-3: The offset of the core spin axis from the mantle symmetry axis is plotted versus the core flattening for the equilibrium points of the system. The equilibrium points are found by adding a small dissipation and integrating the equations of motion. Two broken curves are shown. For the solid curve the full resonance Hamiltonian was used; for the dotted curve the nonlinearity parameter k was set to zero. For small flattening the offset of the core is approximately the obliquity; the core spin axis is perpendicular to the orbit. For large flattening, the offset tends to zero; the core spin axis is locked to the mantle.

Chapter 7

Tidal theory in an elastic mode formulation

7.1 Introduction

Traditionally, solar system studies of tides have relied on the constant time lag model of Darwin (1880), which is the only tidal model with published analytic (not numerical) expressions for tidal heating and orbital decay at high eccentricity (Wisdom, 2008). In this model, tides are raised by an imaginary perturber displaced by a constant time lag along the orbit from the actual perturber. If the orbit expands due to the effect of tides, the time lag is constant and so the phase lag is forced to decrease along with the orbital frequency.

The constant time lag model predicts that tidal dissipation is linearly proportional to the orbital frequency for small phase lags. If we define the tidal quality factor $Q = \arctan \delta$ where δ is the phase lag, then the constant time lag model predicts that Q is proportional to $1/n$ where n is the orbital frequency. Unfortunately, this frequency-dependence is not in agreement with the few measured values.

For instance, the measured Q of the Moon is roughly frequency-independent over the limited frequency range studied. Williams (2008) reports a Q of approximately 30 for a forcing frequency of one month and a Q of about 35 for one year. Terrestrial geophysicists have studied the Earth over a broader frequency range and have found

more complicated frequency dependences, such as described by the Andrade model or Burgers model. Planetary scientists do not understand the frequency dependence of Q , but as far as we do, the constant time lag model seems like a poor choice. The widespread use of the constant time lag model is due to its mathematical tractability, not to any physical evidence in favor of it.

Models of stellar tides take a different approach. Stellar tides are generally described as the excitation of various modes of the star. The theory of the equilibrium tide was pioneered by Zahn (1966, 1970, 1975, 1977, 1989), who computed the viscous dissipation resulting from the velocity field in turbulent convective zones in the star. If dissipation is dominated by the equilibrium tide, the fundamental and acoustic modes of the star are the modes excited by the lower frequency tidal forcing. All dissipation occurs in turbulent regions.

The theory of the dynamical tide describes the response of the star to modes of higher frequency than the fundamental modes. For example, Terquem et al. (1998) and Barker & Ogilvie (2010) examine the excitation of g -modes (gravity modes) and resonances between the tidal forcing and the normal modes of the star. g -modes are modes with a restoring force due to buoyancy. Inertial modes have a restoring force from the Coriolis force and are important contributors to stellar dissipation (Ogilvie & Lin, 2007; Goodman & Lackner, 2009). Recently, Penev & Sasselov (2011) have re-examined the equilibrium tide and constrained the tidal quality factor that applies for extrasolar planets.

In this chapter, we describe a new formulation of solid body tides that models tidal displacements as a sum of excited elastic modes, analogous to the modeling of stellar tides as excited vibrational modes. The assumptions about the tidal frequency dependence enter near the end of the calculation in a modular and mathematically clean manner. This modularity will allow us to easily compare tidal dissipation and its effects for different rheologies in future work. Here we describe the theory and derive general expressions for wobble damping, tidal heating, tidal despinning, and rate of change of semimajor axis and eccentricity for a system with a zero-obliquity perturber in an eccentric, noninclined orbit. We then specify a Kelvin-Voigt rheology, which

corresponds to the constant time lag model, and verify our model with the classic results.

7.2 Static Tidal Distortion

Our principal source for this section is Love (1944). We assume the body is homogeneous and incompressible.

The external disturbing potential is

$$U_T(x, y, z) = \sum_{lm} w_l^m \bar{X}_l^m(x/R, y/R, z/R), \quad (7.1)$$

where w_l^m are the coefficients of solid spherical harmonics \bar{X}_l^m (see Eq. (D.13)), and R is the radius of the body. The external disturbing potential leads to a distortion of the body: this distortion contributes to the disturbing potential. The total potential can be written (Jeffreys, 1976) as $V = \sum_{lm} V_l^m$ where

$$V_l^m(x, y, z) = w_l^m \bar{X}_l^m(x/R, y/R, z/R) + \frac{3g}{2l+1} \epsilon_l^m \bar{X}_l^m(x/R, y/R, z/R). \quad (7.2)$$

The second term arises from the potential of the distortion of the body.

The displacement of a material particle in the body is given

$$\vec{u}(t, x, y, z), \quad (7.3)$$

where the coordinates (x, y, z) refer to the position in the body of material particle before displacement. The equations to be solved are

$$-\nabla p + \mu \nabla^2 \vec{u} + \rho \nabla V = 0, \quad (7.4)$$

Incompressibility implies

$$\nabla \cdot \vec{u} = 0. \quad (7.5)$$

Taking the divergence of the first equation and using the second equation, we see that

$\nabla^2 p = 0$. We then put

$$p(x, y, z) = \rho V(x, y, z) + \tilde{p}(x, y, z), \quad (7.6)$$

where

$$\tilde{p}(x, y, z) = \sum_{lm} p_l^m \bar{X}_l^m(x/R, y/R, z/R), \quad (7.7)$$

and where \bar{X}_l^m is a solid spherical harmonic. Let \vec{u}_1 be¹

$$\begin{aligned} \vec{u}_1(x, y, z) &= \sum_{lm} \left(A_l^m r^2 \nabla \bar{X}_l^m(x/R, y/R, z/R) + B_l^m \vec{x} \bar{X}_l^m(x/R, y/R, z/R) \right), \end{aligned} \quad (7.8)$$

where \bar{X}_l^m is, again, a solid harmonic. Using Eqs. (D.23-D.25), we find that \vec{u}_1 of the form of Eq. (7.8) satisfies Eqs. (7.4) and (7.5) if the following two equations are satisfied:

$$\begin{aligned} p_l^m / \mu &= (4l + 2) A_l^m + 2 B_l^m \\ 0 &= 2l A_l^m + (l + 3) B_l^m, \end{aligned} \quad (7.9)$$

respectively. For $l = 2$, these have the solution

$$\begin{aligned} A_2^m &= \frac{5p_2^m}{42\mu} \\ B_2^m &= -\frac{4p_2^m}{42\mu}. \end{aligned} \quad (7.10)$$

To this solution we may add arbitrary solutions of the equation

$$\nabla^2 \vec{u} = 0, \quad (7.11)$$

¹The gradient operator is $\nabla = \hat{x}\partial/\partial x + \hat{y}\partial/\partial y + \hat{z}\partial/\partial z$; it operates on the (x, y, z) dependence of the following expression, not on the function it is adjacent to. Thus $\nabla \bar{X}_l^m(x/R, y/R, z/R)$ is proportional to $1/R$ times a homogeneous polynomial in $(x/R, y/R, z/R)$.

with

$$\nabla \cdot \vec{u} = 0. \quad (7.12)$$

It will be enough to add solutions of the form

$$\vec{u}_2(x, y, z) = \sum_{lm} f_l^m \nabla \bar{X}_l^m(x/R, y/R, z/R). \quad (7.13)$$

The boundary conditions at the surface (see Love (1944)) require

$$0 = (lA_l^m + B_l^m)R^2 p_l^m + l f_l^m - R \epsilon_l^m \quad (7.14)$$

$$0 = (2lA_l^m + B_l^m)R^2 p_l^m + 2(l-1)f_l^m \quad (7.15)$$

$$\rho w_l^m = (\mu(2lA_l^m + (l+2)B_l^m) - 1)p_l^m + g\rho \left(1 - \frac{3}{2l+1}\right) \epsilon_l^m. \quad (7.16)$$

The solutions for $l = 2$ are

$$p_2^m = -(21/2)(\mu/gR)w_2^m/\Delta \quad (7.17)$$

$$f_2^m = 2(R/g)w_2^m/\Delta \quad (7.18)$$

$$\epsilon_2^m = (5/2)(w_2^m/g)/\Delta, \quad (7.19)$$

where

$$\Delta = 1 + 19\mu/(2\rho gR). \quad (7.20)$$

The displacement Love number is $h_2 = (5/2)/\Delta$. The total displacement $\vec{u}_1 + \vec{u}_2$, for this m , is

$$\vec{u}(x, y, z) = \vec{u}_T^m(x, y, z)h_2w_2^m/(gR), \quad (7.21)$$

defining the tidal shape function \vec{u}_T^m . For $m = 0$, the tidal shape function $\vec{u}_T^0(0, 0, R)$ has the components $(0, 0, R)$, and the displacement at the surface along the z axis, the axis of maximum tidal distortion, is $h_2w_2^0/g$.

7.3 Tidal Disturbing Potential

The tidal disturbing potential is the second harmonic contribution to the gravitational potential energy per unit mass

$$U_2(\vec{x}, \vec{R}') = -\frac{Gm}{(R')^3} \left(\frac{3}{2}(\vec{x} \cdot \hat{R}')^2 - \frac{1}{2}(\vec{x} \cdot \vec{x}) \right), \quad (7.22)$$

where \vec{x} has components (x, y, z) , m is the mass of the perturbing, tide-raising body, and \vec{R}' is the vector from center of mass of the body to the tide raising body. The distance between the bodies is R' , and the direction to the disturbing body is \hat{R}' . Let α , β , and γ be the direction cosines of $\hat{R}' = \alpha\hat{x} + \beta\hat{y} + \gamma\hat{z}$. Then, let N be the rotation that takes the direction \hat{R}' to the \hat{z} direction: $\hat{z} = N\hat{R}'$. Let $N(\theta, \psi) = M_x(\theta)M_z(\psi)$, where M_i are rotations about the indicated axes. Then, $\theta = \text{acos}(\gamma)$ and $\psi = \text{atan}(\alpha, \beta)$. Using the property $(N\vec{x}) \cdot (N\vec{y}) = \vec{x} \cdot \vec{y}$, we see

$$U_2(\vec{x}, \vec{R}') = U_2(N\vec{x}, \vec{z}) \quad (7.23)$$

$$= \sum_m w_2^m(\alpha, \beta, \gamma) \bar{X}_2^m(x/R, y/R, z/R). \quad (7.24)$$

We find $w_2^m(\alpha, \beta, \gamma) = W \bar{X}_2^m(\alpha, \beta, \gamma)$, where $W = -(Gm/R')(R/R')^2$. The corresponding tidal shape function can be obtained with an appropriate rotation of \vec{u}_T^0 .

We have

$$(N(\alpha, \beta, \gamma))^{-1} \vec{u}_T^0(N(\alpha, \beta, \gamma)\vec{x}) = \sum_m \bar{X}_2^m(\alpha, \beta, \gamma) \vec{u}_T^m(\vec{x}). \quad (7.25)$$

7.4 Elastic Free Modes

Our principal source for this section is Lamb (1882). In his terminology, modes corresponding to tidal distortions are vibrations in the second class. We will assume the material is incompressible. Our notation differs slightly from his.

The displacement is described as a sum over modes. Let

$$\phi_{ln}^m(x, y, z)/R = \quad (7.26)$$

$$(\Upsilon_{ln} + \psi_{l-1}^m(\kappa_{ln}r))\nabla \bar{X}_l^m - \frac{l}{l+1} \frac{\kappa_{ln}^2 r^{2l+3}}{(2l+1)(2l+3)} \psi_{l+1}(\kappa_{ln}r) \nabla \left(\frac{\bar{X}_l^m}{r^{2l+1}} \right),$$

where

$$\psi_n(\theta) = (-1)^n (2n+1)!! \left(\frac{1}{\theta} \frac{d}{d\theta} \right)^n \left(\frac{\sin \theta}{\theta} \right), \quad (7.27)$$

where κ_{ln} and Υ_{ln} are explained below. The functions ψ_n are related to the spherical Bessel functions. The displacement is

$$\vec{u}(t, x, y, z) = \sum_{lmn} R A_{ln}^m \phi_{ln}^m(x, y, z) \cos(\omega_l^n t + \epsilon_{ln}^m), \quad (7.28)$$

where A_{ln}^m and ϵ_{ln}^m are the amplitude and phase of each mode. The modes of interest in the tidal problem are $l = 2$, m runs from $-l$ to l , and $n = 1, 2, \dots$. The amplitude A_{ln}^m and the function ϕ_{ln}^m are dimensionless.

The modal frequencies are determined by the condition

$$a_l d_l - b_l c_l = 0, \quad (7.29)$$

where, in the incompressible case,

$$a_l = \frac{(\kappa_{ln} R)^2}{2l+1} - 2(l-1) \quad (7.30)$$

$$b_l = 1 \quad (7.31)$$

$$c_l = 2(l-1) \psi_{l-1}(\kappa_{ln} R) - \frac{(\kappa_{ln} R)^2}{2l+1} \psi_l(\kappa_{ln} R) \quad (7.32)$$

$$d_l = \frac{l}{l+1} \left(\psi_l(\kappa_{ln} R) + \frac{2(l+2)}{\kappa_{ln} R} \psi'_l(\kappa_{ln} R) \right) \quad (7.33)$$

where $\psi'(x) = d\psi(x)/dx$. Note that κ_{ln} occurs only in the combination $\kappa_{ln} R$, determined by Eq. (7.29). The frequencies ω_{ln} of the modes satisfy

$$\kappa_{ln}^2 = \omega_{ln}^2 \rho / \mu, \quad (7.34)$$

where ρ is the density and μ is the rigidity. Numerically, we find the lowest frequency tidal mode has $\kappa_{21} R / \pi = 0.8484938956$, the next lowest frequency mode has

$\kappa_{22}R/\pi = 1.7421226796$, and then $\kappa_{23}R/\pi = 2.8257142846$. Finally,

$$\Upsilon_{ln} = \frac{(\kappa_{ln}R)^2\psi_l(\kappa_{ln}R) - 2(l-1)(2l+1)\psi_{l-1}(\kappa_{ln}R)}{(\kappa_{ln}R)^2 - 2(l-1)(2l+1)}. \quad (7.35)$$

7.5 Representation of Tidal Distortion by Elastic Modes

Define the overlap integral

$$\langle \vec{u}_1, \vec{u}_2 \rangle = \frac{1}{V} \int_V (\vec{u}_1 \cdot \vec{u}_2) dV. \quad (7.36)$$

where $V = (4/3)\pi R^3$, the volume of the body. The elastic modes have zero overlap. Let

$$(\beta_{2n})^2 = \langle \phi_{2n}^m, \phi_{2n}^m \rangle. \quad (7.37)$$

Note that β_{2n} is independent of m . We find: $\beta_{21} = 0.5325432017$, $\beta_{22} = 0.2145631038$, and $\beta_{23} = 0.0826504258$. Define the $l = 2$ normalized elastic modes:

$$\vec{u}_{nm}^M = R\phi_{2n}^m/\beta_{2n}. \quad (7.38)$$

The tidal shape function \vec{u}_T^0 can be expanded in terms of the normalized elastic modes with $m = 0$. Let

$$\vec{u}_T^0(x, y, z) = \sum_n g_n \vec{u}_{n0}^M(x, y, z), \quad (7.39)$$

then

$$g_n = \langle \vec{u}_T^0, \vec{u}_n \rangle. \quad (7.40)$$

We find $g_1 = 0.5608256130$, $g_2 = -0.0381757369$, and $g_3 = 0.0039974227$. The tidal shape function and its representation in terms of the elastic modes is shown in Figure 7-1.

If the tidal distortion is rotated, then the representing modes rotate accordingly.

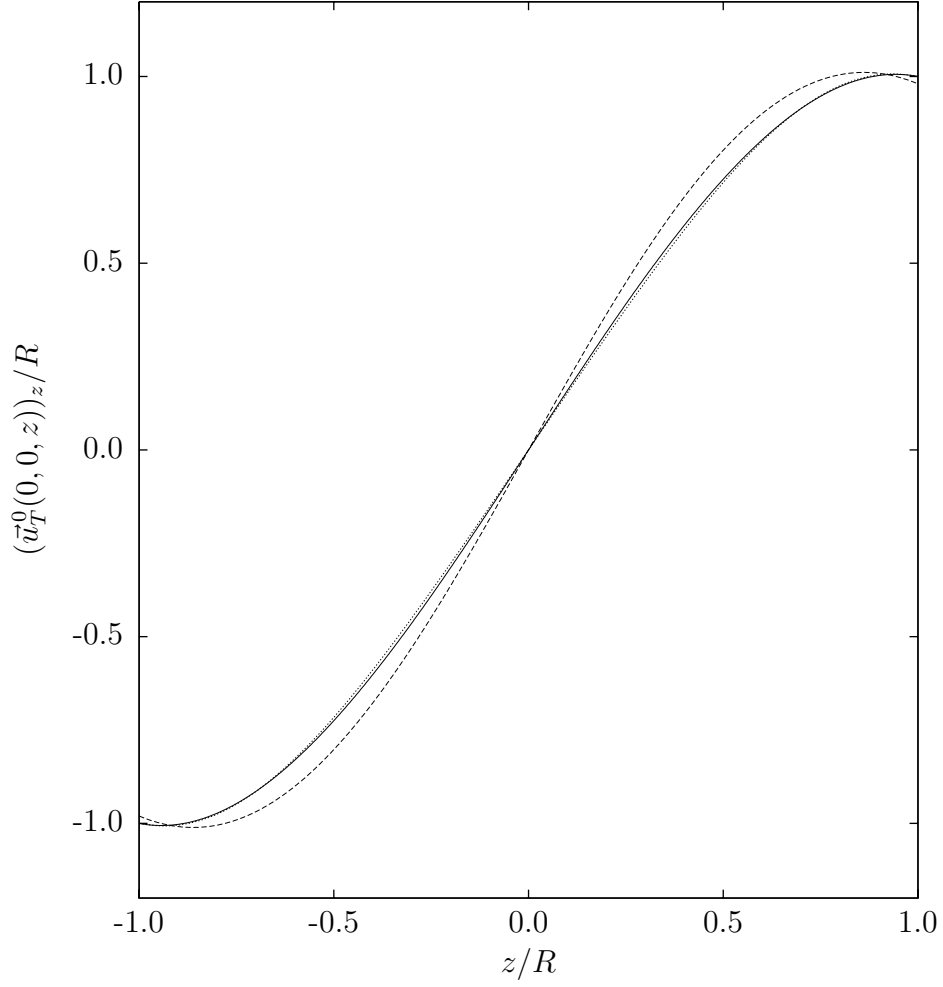


Figure 7-1: The solid line shows the z component of the tidal shape function \vec{u}_T^0 . The dashed line shows the representation of the tidal shape function using the $n = 1$ elastic mode. The dotted line shows the representation using the $n = 1$ and $n = 2$ modes. The three mode representation is indistinguishable from the solid line on this scale.

For a disturbing body with direction cosines (α, β, γ) the tidal distortion is

$$\vec{u}(x, y, z) = \frac{h_2 W}{gR} \sum_m \bar{X}_2^m(\alpha, \beta, \gamma) \vec{u}_T^m(x, y, z) \quad (7.41)$$

$$= \frac{h_2 W}{gR} \sum_{mn} g_n \bar{X}_2^m(\alpha, \beta, \gamma) \vec{u}_{nm}^M(x, y, z). \quad (7.42)$$

7.6 Lagrangian for Elastic Modes

We treat each mode as a degree of freedom. We assume here that the configuration of the body is given as a sum of modal distortions (with $l = 2$). We write the displacement as

$$\vec{u}(t, x, y, z) = \sum_{mn} \Pi_{nm}(t) \vec{u}_{nm}^M(x, y, z) \quad (7.43)$$

where $\Pi_{nm}(t)$ is the dimensionless modal coordinate at time t .

The kinetic energy in each mode is

$$T_{nm}(t, \Pi_{nm}, \dot{\Pi}_{nm}) = \frac{1}{2} M R^2 \dot{\Pi}_{nm}^2 \quad (7.44)$$

with $M = \rho V$, the mass of the body. Recall that the modes are normalized. We know the frequency of each mode, so we can write the elastic potential energy for each mode:

$$V_{nm}(t, \Pi_{nm}, \dot{\Pi}_{nm}) = \frac{1}{2} M R^2 \omega_{2n}^2 \Pi_{nm}^2. \quad (7.45)$$

The Lagrangian for the free elastic modes is then

$$L(t, \Pi, \dot{\Pi}) = \frac{1}{2} M R^2 \sum_{mn} (\dot{\Pi}_{nm}^2 - \omega_{2n}^2 \Pi_{nm}^2). \quad (7.46)$$

This give the equation of motion

$$M R^2 (\ddot{\Pi}_{nm} + \omega_{2n}^2 \Pi_{nm}) = 0, \quad (7.47)$$

confirming a free oscillation with frequency ω_{2n} . The modes will be forced when the

full potential energy is developed.

7.7 Kinetic Energy

The next task is to develop the kinetic energy of the rotating body, taking into account the fact that the shape is changing. We assume the undistorted starting configuration of the body is a sphere of radius R and density ρ , with moment of inertia $(2/5)MR^2$. The configuration of the body at time t is obtained by distorting and rotating this reference body. We give the body a distortion \vec{u}_A that gives the principal moments of inertia and a time-dependent modal tidal distortion $\vec{u}_T(t)$, followed by a time-dependent rotation $M(t)$ in space. The position of each constituent is

$$\vec{x}_\alpha(t) = M(t)(\vec{x}_0 + \vec{u}_A + \vec{u}_T(t)). \quad (7.48)$$

The velocity of the constituent is

$$\dot{\vec{x}}_\alpha(t) = \dot{M}(t)(\vec{x}_0 + \vec{u}_A + \vec{u}_T(t)) + M(t)(\dot{\vec{u}}_T(t)) \quad (7.49)$$

$$= \dot{M}(t)M(t)^{-1}M(t)(\vec{x}_0 + \vec{u}_A + \vec{u}_T(t)) + M(t)(\dot{\vec{u}}_T(t)) \quad (7.50)$$

$$= \vec{\omega}(t) \times (M(t)(\vec{x}_0 + \vec{u}_A + \vec{u}_T(t))) + M(t)(\dot{\vec{u}}_T(t)) \quad (7.51)$$

$$= M(t)(\vec{\omega}'(t) \times (\vec{x}_0 + \vec{u}_A + \vec{u}_T(t)) + \dot{\vec{u}}_T(t)) \quad (7.52)$$

The square of the velocity is

$$\begin{aligned} (\dot{\vec{x}}_\alpha(t))^2 &= (\vec{\omega}'(t) \times (\vec{x}_0 + \vec{u}_A)) \cdot (\vec{\omega}'(t) \times (\vec{x}_0 + \vec{u}_A)) \\ &\quad + 2(\vec{\omega}'(t) \times (\vec{x}_0 + \vec{u}_A)) \cdot (\vec{\omega}'(t) \times \vec{u}_T(t) + \dot{\vec{u}}_T(t)) \\ &\quad + (\vec{\omega}'(t) \times \vec{u}_T(t) + \dot{\vec{u}}_T(t)) \cdot (\vec{\omega}'(t) \times \vec{u}_T(t) + \dot{\vec{u}}_T(t)) \end{aligned} \quad (7.53)$$

The distortion \vec{u}_A that gives the principal moments is volume preserving; it can be represented as a gradient

$$\vec{u}_A(x, y, z) = aR^2 \nabla \bar{X}_2^0(x/R, y/R, z/R) + bR^2 \nabla \bar{X}_2^2(x/R, y/R, z/R), \quad (7.54)$$

where

$$a = \frac{(B+A)/2 - C}{A+B+C} \quad (7.55)$$

$$b = \frac{(\sqrt{3}/2)(B-A)}{A+B+C}. \quad (7.56)$$

The sum of the principal moments is $3I$ where $I = (2/5)MR^2$, the moment of inertia of a homogeneous sphere. In these expressions we are ignoring second order contributions to the moments in a and b ; we are assuming a and b are small. Note that we can write

$$R\nabla\bar{X}_2^0 = (-\bar{X}_1^1, -\bar{X}_1^{-1}, 2\bar{X}_1^0). \quad (7.57)$$

and

$$R\nabla\bar{X}_2^2 = (\sqrt{3}\bar{X}_1^1, -\sqrt{3}\bar{X}_1^{-1}, 0). \quad (7.58)$$

For convenience, we introduce

$$\vec{u}_A^0(x, y, z) = (x, y, z) \quad (7.59)$$

$$\vec{u}_A^1(x, y, z) = R^2\nabla\bar{X}_2^0(x/R, y/R, z/R) \quad (7.60)$$

$$\vec{u}_A^2(x, y, z) = R^2\nabla\bar{X}_2^2(x/R, y/R, z/R). \quad (7.61)$$

The first term in the kinetic energy integral is, by design,

$$\begin{aligned} & \frac{1}{2} \int_V \rho((\vec{\omega}'(t) \times (\vec{x}_0 + \vec{u}_A)) \cdot (\vec{\omega}'(t) \times (\vec{x}_0 + \vec{u}_A))) dV \\ &= \frac{1}{2} (A(\omega^a)^2 + B(\omega^b)^2 + C(\omega^c)^2), \end{aligned} \quad (7.62)$$

where the components of $\vec{\omega}'$ are $(\omega^a, \omega^b, \omega^c)$.

Introduce the integrals

$$I_{knmij}^{(1)} = \frac{1}{V} \int_V (e_i \times \vec{u}_A^k) \cdot (e_j \times \vec{u}_{nm}^M) dV, \quad (7.63)$$

$$I_{knmi}^{(2)} = \frac{1}{V} \int_V (e_i \times \vec{u}_A^k) \cdot \vec{u}_{nm}^M dV, \quad (7.64)$$

$$I_{nmn'm'ij}^{(3)} = \frac{1}{V} \int_V (e_i \times \vec{u}_{nm}^M) \cdot (e_j \times \vec{u}_{n'm'}^M) dV, \quad (7.65)$$

$$I_{nmn'm'i}^{(4)} = \frac{1}{V} \int_V (e_i \times \vec{u}_{nm}^M) \cdot \vec{u}_{n'm'}^M dV. \quad (7.66)$$

In terms of these integrals, the complete kinetic energy is

$$\begin{aligned} T(t; q, \Pi; \omega', \dot{\Pi}) = & \frac{1}{2} (A(\omega^a)^2 + B(\omega^b)^2 + C(\omega^c)^2) \\ & + MR^2 \sum_{knmij} a_k I_{knmij}^{(1)} (\omega')^i (\omega')^j \Pi_{nm} \\ & + MR^2 \sum_{knm i} a_k I_{knm i}^{(2)} (\omega')^i \dot{\Pi}_{nm} \\ & + \frac{1}{2} MR^2 \sum_{nmn'm'ij} I_{nmn'm'ij}^{(3)} (\omega')^i (\omega')^j \Pi_{nm} \Pi_{n'm'} \\ & + MR^2 \sum_{nmn'm'i} I_{nmn'm'i}^{(4)} (\omega')^i \Pi_{nm} \dot{\Pi}_{n'm'} \\ & + \frac{1}{2} MR^2 \sum_{nm} \left(\dot{\Pi}_{nm} \right)^2, \end{aligned} \quad (7.67)$$

where $a_0 = 1$, $a_1 = a$, and $a_2 = b$, and q are the coordinates that specify the orientation of the body in space. For $k = 0$, the nonzero coefficients are:

$$I_{0,n,0,0,0}^{(1)} = I_{0,n,0,1,1}^{(1)} = C_n \quad (7.68)$$

$$I_{0,n,0,2,2}^{(1)} = -2C_n \quad (7.69)$$

$$I_{0,n,1,0,2}^{(1)} = I_{0,n,2,0,0}^{(1)} = I_{0,n,-1,1,2}^{(1)} = I_{0,n,-2,0,1}^{(1)} = -\sqrt{3}C_n \quad (7.70)$$

$$I_{0,n,2,1,1}^{(1)} = \sqrt{3}C_n, \quad (7.71)$$

with $C_1 = 0.1747793752$, $C_2 = -0.0501544874$, and $C_3 = 0.0138166088$, and with $I_{0nmij}^{(1)} = I_{0nmji}^{(1)}$. These have a simple representation $I_{0nmij}^{(1)} = -C_n \partial_i \partial_j \bar{X}_2^m(\omega^a, \omega^b, \omega^c)$.

7.8 Potential Energy

The gravitational potential energy is the integral of Eq. (7.22) over the mass of the body:

$$V_G(t; q, \Pi; \omega', \dot{\Pi}) = \int_V \rho U_2(\vec{x}, \vec{R}') dV \quad (7.72)$$

It is convenient to introduce a number of integrals, and then write the potential energy in terms of them. Let

$$J_{knm}^{(1)} = \frac{1}{V} \int_V \vec{u}_A^k \cdot \vec{u}_{nm}^M dV, \quad (7.73)$$

$$J_{nmn'm'}^{(2)} = \frac{1}{V} \int_V \vec{u}_{nm}^M \cdot \vec{u}_{n'm'}^M dV = \delta_{nn'} \delta_{mm'} \quad (7.74)$$

$$J_{knmij}^{(3)} = \frac{1}{V} \int_V (\hat{e}_i \cdot \vec{u}_A^k) (\hat{e}_j \cdot \vec{u}_{nm}^M) dV, \quad (7.75)$$

$$J_{nmn'm'ij}^{(4)} = \frac{1}{V} \int_V (\hat{e}_i \cdot \vec{u}_{nm}^M) (\hat{e}_j \cdot \vec{u}_{n'm'}^M) dV. \quad (7.76)$$

In terms of these the gravitational potential energy is

$$\begin{aligned} & V_G(t; q, \Pi; \omega', \dot{\Pi}) \\ &= -\frac{Gm}{(R')^3} \left(\frac{(1 - 3(\alpha')^2)A + (1 - 3(\beta')^2)B + (1 - 3(\gamma')^2)C}{2} \right) \\ &+ \frac{GmM}{R'} \left(\frac{R}{R'} \right)^2 \sum_{knm} J_{knm}^{(1)} a_k \Pi_{nm} \\ &+ \frac{1}{2} \frac{GmM}{R'} \left(\frac{R}{R'} \right)^2 \sum_{nmn'm'} J_{nmn'm'}^{(2)} \Pi_{nm} \Pi_{n'm'} \\ &- 3 \frac{GmM}{R'} \left(\frac{R}{R'} \right)^2 \sum_{ijknm} J_{knmij}^{(3)} \alpha'_i \alpha'_j a_k \Pi_{nm} \\ &- \frac{3}{2} \frac{GmM}{R'} \left(\frac{R}{R'} \right)^2 \sum_{ijnmnm'm'} J_{nmn'm'ij}^{(4)} \alpha'_i \alpha'_j \Pi_{nm} \Pi_{n'm'}, \end{aligned} \quad (7.77)$$

where $\alpha'_0 = \alpha'$, $\alpha'_1 = \beta'$, $\alpha'_2 = \gamma'$, and $(\alpha', \beta', \gamma')$ are the direction cosines of the perturbing body with respect to the body axes:

$$(\alpha', \beta', \gamma') = (M(q))^{-1} (\alpha, \beta, \gamma), \quad (7.78)$$

and (α, β, γ) are the direction cosines of the perturbing body with respect to a spatially fixed rectangular basis, and $M(q)$ is the rotation that carries the body in its reference orientation (with principal axes aligned with the spatial axes) to the actual orientation specified by the coordinates q .

The coefficients $J_{0nm}^{(1)}$ are all zero, but there are some nonzero $k = 0$ terms among the $J_{knmij}^{(3)}$. Specifically,

$$J_{0,n,0,0,0}^{(3)} = J_{0,n,0,1,1}^{(3)} = -C_n \quad (7.79)$$

$$J_{0,n,0,2,2}^{(3)} = 2C_n \quad (7.80)$$

$$J_{0,n,2,0,0}^{(3)} = J_{0,n,-2,0,1}^{(3)} = J_{0,n,1,0,2}^{(3)} = J_{0,n,-1,1,2}^{(3)} = \sqrt{3}C_n \quad (7.81)$$

$$J_{0,n,2,1,1}^{(3)} = -\sqrt{3}C_n \quad (7.82)$$

with C_n as before, and $J_{ij0nm}^{(3)} = J_{ji0nm}^{(3)}$. These have the simple representation $J_{0nmij}^{(3)} = C_n \partial_i \partial_j \bar{X}_2^m(\alpha', \beta', \gamma')$.

Recall that the elastic potential energy, following Eq. (7.45), is

$$V_E(t; q, \Pi; \omega', \dot{\Pi}) = \frac{1}{2} M R^2 \sum_{nm} \omega_{2n}^2 \Pi_{nm}^2. \quad (7.83)$$

The total potential energy is $V = V_G + V_E$.

7.9 Lagrangian and Equations of Motion

The Lagrangian for the system is the difference of the kinetic energy T and the potential energy V . Note that the kinetic energy does not depend on q and the potential energy does not depend on ω' . Further, the potential energy depends on q only through $(\alpha', \beta', \gamma')$.

It will be convenient to use Euler-like angles to specify the orientation of the body with respect to its reference orientation with the principal axes $(\hat{a}, \hat{b}, \hat{c})$ aligned with the rectangular spatial axes $(\hat{x}, \hat{y}, \hat{z})$. These are the principal axes of the body without tidal distortion. We choose the rotation that carries the body to its actual orientation

as

$$M(\theta, \phi, \psi) = M_z(\phi)M_x(\theta)M_y(\psi). \quad (7.84)$$

Note that these are not the usual Euler angles.

The equations of motion for the angular velocities $(\omega^a, \omega^a, \omega^c)$ and the coordinates (θ, ϕ, ψ) are the Poincaré equations (Poincaré, 1910b). The equations of motion for the velocities $\dot{\Pi}$ and the coordinates Π are the Lagrange equations. In the derivation of the Poincaré equations, we use the vector field basis corresponding to infinitesimal rotations about the body axes $(\hat{a}, \hat{b}, \hat{c})$. In the chosen coordinates, the basis vector fields are

$$e_a = \cos \psi \frac{\partial}{\partial \theta} - \frac{\sin \psi}{\cos \theta} \frac{\partial}{\partial \phi} + \frac{\sin \psi \sin \theta}{\cos \theta} \frac{\partial}{\partial \psi} \quad (7.85)$$

$$e_b = \frac{\partial}{\partial \psi} \quad (7.86)$$

$$e_c = \sin \psi \frac{\partial}{\partial \theta} + \frac{\cos \psi}{\cos \theta} \frac{\partial}{\partial \phi} - \frac{\cos \psi \sin \theta}{\cos \theta} \frac{\partial}{\partial \psi} \quad (7.87)$$

The commutators of these basis fields satisfy

$$[e_i, e_j](f) = \sum_{ijk} c_{ij}^k e_k(f), \quad (7.88)$$

with structure constants

$$c_{ij}^k = \epsilon_{ijk}, \quad (7.89)$$

where ϵ_{ijk} is 1 for (i, j, k) equal to a cyclic permutation of $(0, 1, 2)$, -1 for a cyclic permutation of $(2, 1, 0)$, and 0 otherwise. Concretely,

$$[e_a, e_b] = e_c \quad (7.90)$$

$$[e_b, e_c] = e_a \quad (7.91)$$

$$[e_c, e_a] = e_b. \quad (7.92)$$

The Lagrangian depends on the coordinates (θ, ϕ, ψ) only through $(\alpha', \beta', \gamma')$. In the Poincaré equations we need $e_i(\hat{L})$, where \hat{L} is the Lagrangian written in terms of the

angular velocities, and the vector field takes the derivative of the coordinate slot of the Lagrangian. We have

$$e_a(\hat{L}) = \gamma' \frac{\partial \hat{L}}{\partial \beta'} - \beta' \frac{\partial \hat{L}}{\partial \gamma'} \quad (7.93)$$

$$e_b(\hat{L}) = \alpha' \frac{\partial \hat{L}}{\partial \gamma'} - \gamma' \frac{\partial \hat{L}}{\partial \alpha'} \quad (7.94)$$

$$e_c(\hat{L}) = \beta' \frac{\partial \hat{L}}{\partial \alpha'} - \alpha' \frac{\partial \hat{L}}{\partial \beta'}. \quad (7.95)$$

The Poincaré equations are, in this case,

$$\frac{d}{dt} \left(\frac{\partial \hat{L}}{\partial \omega^a} \right) = \gamma' \frac{\partial \hat{L}}{\partial \beta'} - \beta' \frac{\partial \hat{L}}{\partial \gamma'} + \omega^c \frac{\partial \hat{L}}{\partial \omega^b} - \omega^b \frac{\partial \hat{L}}{\partial \omega^c} \quad (7.96)$$

$$\frac{d}{dt} \left(\frac{\partial \hat{L}}{\partial \omega^b} \right) = \alpha' \frac{\partial \hat{L}}{\partial \gamma'} - \gamma' \frac{\partial \hat{L}}{\partial \alpha'} + \omega^a \frac{\partial \hat{L}}{\partial \omega^c} - \omega^c \frac{\partial \hat{L}}{\partial \omega^a} \quad (7.97)$$

$$\frac{d}{dt} \left(\frac{\partial \hat{L}}{\partial \omega^c} \right) = \beta' \frac{\partial \hat{L}}{\partial \alpha'} - \alpha' \frac{\partial \hat{L}}{\partial \beta'} + \omega^b \frac{\partial \hat{L}}{\partial \omega^a} - \omega^a \frac{\partial \hat{L}}{\partial \omega^b} \quad (7.98)$$

For our Lagrangian, including the $I_{knmij}^{(1)}$ terms in the kinetic energy with $k = 0$, but ignoring the other $I^{(i)}$ contributions, we find

$$\frac{\partial \hat{L}}{\partial \omega^a} = A\omega^a - 2MR^2 \sum_{nm} C_n \partial_0 \bar{X}_2^m(\omega^a, \omega^b, \omega^c) \Pi_{nm} \quad (7.99)$$

$$\frac{\partial \hat{L}}{\partial \omega^b} = B\omega^b - 2MR^2 \sum_{nm} C_n \partial_1 \bar{X}_2^m(\omega^a, \omega^b, \omega^c) \Pi_{nm} \quad (7.100)$$

$$\frac{\partial \hat{L}}{\partial \omega^c} = C\omega^c - 2MR^2 \sum_{nm} C_n \partial_2 \bar{X}_2^m(\omega^a, \omega^b, \omega^c) \Pi_{nm} \quad (7.101)$$

Similarly, keeping the $k = 0$ terms in $J_{knmij}^{(3)}$, but ignoring the other $J^{(i)}$ terms, we find

$$\frac{\partial \hat{L}}{\partial \alpha'} = -\frac{Gm}{(R')^3} 3A\alpha' + MR^2 \sum_{nm} \mathcal{F}_n \Pi_{nm} \partial_0 \bar{X}_2^m(\alpha', \beta', \gamma') \quad (7.102)$$

$$\frac{\partial \hat{L}}{\partial \beta'} = -\frac{Gm}{(R')^3} 3B\beta' + MR^2 \sum_{nm} \mathcal{F}_n \Pi_{nm} \partial_1 \bar{X}_2^m(\alpha', \beta', \gamma') \quad (7.103)$$

$$\frac{\partial \hat{L}}{\partial \gamma'} = -\frac{Gm}{(R')^3} 3C\gamma' + MR^2 \sum_{nm} \mathcal{F}_n \Pi_{nm} \partial_2 \bar{X}_2^m(\alpha', \beta', \gamma'), \quad (7.104)$$

where

$$\mathcal{F}_n = \frac{Gm}{(R')^3} (6C_n) \approx \frac{Gm}{(R')^3} \left(\frac{R\omega_{2n}^2 h_2 g_n}{g} \right), \quad (7.105)$$

where the last form of \mathcal{F}_n is valid for large rigidity. The Poincaré equations are constructed from these components.

Keeping the same terms as before, the Lagrange equations governing the motion of Π_{nm} are

$$\ddot{\Pi}_{nm} + \omega_{2n}^2 \Pi_{nm} = -2C_n \bar{X}_2^m(\omega^a, \omega^b, \omega^c) + \mathcal{F}_n \bar{X}_2^m(\alpha', \beta', \gamma'). \quad (7.106)$$

Note that if we ignore the terms involving Π Poincaré's equations become

$$A \frac{d\omega^a}{dt} = (B - C)\omega^b \omega^c - \frac{3Gm}{(R')^3} (B - C)\beta' \gamma' \quad (7.107)$$

$$B \frac{d\omega^b}{dt} = (C - A)\omega^a \omega^c - \frac{3Gm}{(R')^3} (C - A)\alpha' \gamma' \quad (7.108)$$

$$C \frac{d\omega^c}{dt} = (A - B)\omega^a \omega^b - \frac{3Gm}{(R')^3} (A - B)\alpha' \beta', \quad (7.109)$$

which are just Euler's equations for the motion of a rigid body subject to a gravity-gradient torque.

7.10 Chandler Wobble

Elasticity affects the period of the Eulerian wobble of the Earth (Chandler, 1891; Newcomb, 1892). As an illustration of the formalism we have developed we will calculate the elastic correction to the frequency of the Eulerian wobble. We assume the body is rotating very nearly with its spin axis aligned with the \hat{c} principal axis, and that the body is axisymmetric $A = B$. We assume there is no external perturbing body. For simplicity we take into account only the gravest elastic modes (those with $n = 1$). We assume here that the elastic modes are in equilibrium, so, from

Eq. (7.106), we have

$$\Pi_{1m} = -2C_1 \bar{X}_2^m(\omega^a, \omega^b, \omega^c)/\omega_{21}^2. \quad (7.110)$$

We will assume ω^a and ω^b are much smaller than ω^c ; we will systematically ignore terms that are second and higher order in ω^a and ω^b . With this assumption

$$\Pi_{1,0} = -2C_1 \frac{(\omega^c)^2}{\omega_{21}^2} \quad (7.111)$$

$$\Pi_{1,1} = -2\sqrt{3}C_1 \frac{\omega^a \omega^c}{\omega_{21}^2} \quad (7.112)$$

$$\Pi_{1,-1} = -2\sqrt{3}C_1 \frac{\omega^b \omega^c}{\omega_{21}^2} \quad (7.113)$$

$$\Pi_{1,2} = 0 \quad (7.114)$$

$$\Pi_{1,-2} = 0. \quad (7.115)$$

We have, in this case,

$$\begin{aligned} \frac{\partial \hat{L}}{\partial \omega^a} &= A\omega^a + 2C_1 MR^2 \Pi_{1,0} \omega^a - 2\sqrt{3}C_1 MR^2 \Pi_{1,1} \omega^c \\ \frac{\partial \hat{L}}{\partial \omega^b} &= B\omega^b + 2C_1 MR^2 \Pi_{1,0} \omega^b - 2\sqrt{3}C_1 MR^2 \Pi_{1,-1} \omega^c \\ \frac{\partial \hat{L}}{\partial \omega^c} &= C\omega^c - 4C_1 MR^2 \Pi_{1,0} \omega^c. \end{aligned} \quad (7.116)$$

The Poincaré equations, with these assumptions, show that ω^c is constant, so $\Pi_{1,0}$ is also constant. We define

$$A' = A + 2C_1 MR^2 \Pi_{1,0} = A - 4C_1^2 MR^2 \left(\frac{\omega^c}{\omega_{21}} \right)^2 \quad (7.117)$$

$$B' = B + 2C_1 MR^2 \Pi_{1,0} = B - 4C_1^2 MR^2 \left(\frac{\omega^c}{\omega_{21}} \right)^2 \quad (7.118)$$

$$C' = C - 4C_1 MR^2 \Pi_{1,0} = C + 8C_1^2 MR^2 \left(\frac{\omega^c}{\omega_{21}} \right)^2, \quad (7.119)$$

and assume that (A', B', C') are the observed principal moments of inertia. The

Poincaré equations are then

$$A'\dot{\omega}^a \left(1 + 12C_1^2 \frac{MR^2}{A'} \left(\frac{\omega^c}{\omega_{21}} \right)^2 \right) = \omega^b \omega^c (B' - C') + 12C_1^2 \left(\frac{\omega^c}{\omega_{21}} \right)^2 MR^2 \omega^b \omega^c \quad (7.120)$$

$$B'\dot{\omega}^b \left(1 + 12C_1^2 \frac{MR^2}{B} \left(\frac{\omega^c}{\omega_{21}} \right)^2 \right) = \omega^a \omega^c (C' - A') - 12C_1^2 \left(\frac{\omega^c}{\omega_{21}} \right)^2 MR^2 \omega^a \omega^c \quad (7.121)$$

Taking the time derivative of the first equation and using the second, we find

$$\ddot{\omega}^a = -\omega_C^2 \omega^a, \quad (7.122)$$

where the Chandler frequency is

$$\omega_C = \omega^c \left(\frac{C' - A'}{A'} - 12C_1^2 \frac{MR^2}{A} \left(\frac{\omega^c}{\omega_{21}} \right)^2 \right), \quad (7.123)$$

and we have ignored a quantity of second order. We see that the Eulerian frequency, $\omega^c(C' - A')/A'$, is reduced by elasticity. As developed, our theory does not apply to a body such as the Earth where the body has significant radial variation in density. Nevertheless, we can see what effective rigidity a homogeneous Earth must have to get the observed Chandler period of 434 days. Using a density of 5500kg/m^3 and a radius of 6371000m , $C'/(MR^2) = 0.3307$, and $A'/(MR^2) = 0.3296$, we find $\mu = 1.8 \times 10^{11}\text{N/m}^2$, which is actually comparable to modern estimates of the rigidity of the Earth at a depth of about 1000km (Stacey, 1992). But our model is not really applicable to the Earth.

7.11 Dissipation

The Q of an oscillator is defined as

$$\frac{1}{Q} = \frac{1}{2\pi E^*} \oint \frac{dE}{dt} dt, \quad (7.124)$$

where dE/dt is the rate at which work is done on the oscillator, E^* is the energy stored in the oscillator, and the integral is over one cycle of the oscillation. Consider the damped driven oscillator

$$m(\ddot{x} + d\dot{x} + \omega_0^2 x) = A \cos(\omega t). \quad (7.125)$$

The forced response is

$$x(t) = B \cos(\omega t - \delta), \quad (7.126)$$

where

$$B^2 = \left(\frac{A}{m}\right)^2 \frac{1}{(\omega_0^2 - \omega^2)^2 + (\omega d)^2}. \quad (7.127)$$

Let

$$\delta_0 = \arctan(\omega d, \omega_0^2 - \omega^2), \quad (7.128)$$

then for $\omega < \omega_0$ the phase shift $\delta = \delta_0$ is positive, meaning that the response of the oscillator lags the forcing, and B is positive. For $\omega > \omega_0$, the phase shift δ_0 is greater than $\pi/2$. We could take $\delta = \delta_0$ for all ω and always keep B positive. Alternatively, we can bring δ into the range of $-\pi/2$ to $\pi/2$ (the range of the one argument arctan) by subtracting π from δ_0 making $\delta = \delta_0 - \pi$ negative. Then we flip the sign of B to be negative, so that the solution remains valid. So for $\omega < \omega_0$, both δ and B are positive, and for $\omega > \omega_0$ both δ and B are negative. This reflects more clearly that the response is out of phase with the forcing.

The energy dissipated per cycle is

$$\Delta E = \pi AB \sin \delta, \quad (7.129)$$

which is positive. For now, we take the peak energy stored in the oscillator to be

$$E^* = m\omega_0^2 B^2/2, \quad (7.130)$$

and return to this definition later. The Q is then given by

$$\frac{1}{Q} = \frac{((\omega_0^2 - \omega^2)^2 + (\omega d)^2)^{1/2}}{\omega_0^2} \sin \delta \quad (7.131)$$

$$\approx \frac{((\omega_0^2 - \omega^2)^2)^{1/2}}{\omega_0^2} \sin \delta \quad (7.132)$$

$$\approx \sin \delta, \quad (7.133)$$

where the first approximation is for small dissipation (small d), and the second approximation additionally assumes small forcing frequency ($\omega \ll \omega_0$). In the same limit

$$\tan \delta \approx \omega d / \omega_0^2. \quad (7.134)$$

So for large Q

$$\frac{1}{Q} \approx \frac{\omega d}{\omega_0^2}. \quad (7.135)$$

Note that in this model and with these definitions Q is inversely proportional to ω .

We incorporate tidal dissipation by adding an ad hoc dissipative term to the modal equations, Eq. (7.106),

$$\ddot{\Pi}_{nm} + d_n \dot{\Pi}_{nm} + \omega_{2n}^2 \Pi_{nm} = -2C_n \bar{X}_2^m(\omega^a, \omega^b, \omega^c) + \mathcal{F}_n \bar{X}_2^m(\alpha', \beta', \gamma'). \quad (7.136)$$

We assume d_n is independent of m . We have

$$\frac{1}{Q_n} \approx \frac{\omega d_n}{\omega_{2n}^2}, \quad (7.137)$$

where ω is the forcing frequency, assumed to be much less than the modal frequency.

7.12 Wobble Damping

Here we consider the decay of the Eulerian wobble due to dissipation in the elastic modes. We again assume that the spin axis is nearly aligned with the \hat{c} axis. The damped modal equations (keeping only $n = 1$ modes) are

$$\ddot{\Pi}_{1,0} + d_1 \dot{\Pi}_{1,0} + \omega_{21}^2 \Pi_{1,0} = -2C_1(\omega^c)^2 \quad (7.138)$$

$$\ddot{\Pi}_{1,1} + d_1 \dot{\Pi}_{1,1} + \omega_{21}^2 \Pi_{1,1} = -2\sqrt{3}C_1\omega^c\omega^a \quad (7.139)$$

$$\ddot{\Pi}_{1,-1} + d_1 \dot{\Pi}_{1,-1} + \omega_{21}^2 \Pi_{1,-1} = -2\sqrt{3}C_1\omega^c\omega^b. \quad (7.140)$$

As ω^c is constant, we can assume

$$\Pi_{1,0} = -2C_1(\omega^c/\omega_{21})^2, \quad (7.141)$$

is constant. To construct the Poincaré equations we need

$$\begin{aligned} \frac{\partial \hat{L}}{\partial \omega^a} &= A\omega^a + 2C_1MR^2\Pi_{1,0}\omega^a - 2\sqrt{3}C_1MR^2\Pi_{1,1}\omega^c \\ \frac{\partial \hat{L}}{\partial \omega^b} &= B\omega^b + 2C_1MR^2\Pi_{1,0}\omega^b - 2\sqrt{3}C_1MR^2\Pi_{1,-1}\omega^c \end{aligned} \quad (7.142)$$

ignoring second order quantities. Define (A', B', C') as before, and assume these are the observed values of the principal moments. Then the left hand sides of the Poincaré equations are

$$\frac{d}{dt} \frac{\partial \hat{L}}{\partial \omega^a} = A'\dot{\omega}^a - 2\sqrt{3}C_1MR^2\omega^c\dot{\Pi}_{1,1} \quad (7.143)$$

$$\frac{d}{dt} \frac{\partial \hat{L}}{\partial \omega^b} = B'\dot{\omega}^b - 2\sqrt{3}C_1MR^2\omega^c\dot{\Pi}_{1,-1} \quad (7.144)$$

and the right hand sides are

$$\omega^c \frac{\partial \hat{L}}{\partial \omega^b} - \omega^b \frac{\partial \hat{L}}{\partial \omega^c} = \omega^c\omega^b(B' - C') - 2\sqrt{3}C_1MR^2(\omega^c)^2\Pi_{1,-1} \quad (7.145)$$

$$\omega^a \frac{\partial \hat{L}}{\partial \omega^c} - \omega^c \frac{\partial \hat{L}}{\partial \omega^a} = \omega^c \omega^a (C' - A') + 2\sqrt{3}C_1 MR^2 (\omega^c)^2 \Pi_{1,1}. \quad (7.146)$$

Collecting the equations, the wobble damping is governed by the constant coefficient linear differential equations:

$$0 = \ddot{\Pi}_{1,1} + d_1 \dot{\Pi}_{1,1} + \omega_{21}^2 \Pi_{1,1} + \xi \omega^c \omega^a \quad (7.147)$$

$$0 = \ddot{\Pi}_{1,-1} + d_1 \dot{\Pi}_{1,-1} + \omega_{21}^2 \Pi_{1,-1} + \xi \omega^c \omega^b \quad (7.148)$$

$$0 = A' \dot{\omega}^a - \xi \omega^c MR^2 \dot{\Pi}_{1,1} - \omega^c \omega^b (B' - C') + \xi \omega^c MR^2 \omega^c \Pi_{1,-1} \quad (7.149)$$

$$0 = B' \dot{\omega}^b - \xi \omega^c MR^2 \dot{\Pi}_{1,-1} - \omega^c \omega^a (C' - A') - \xi \omega^c MR^2 \omega^c \Pi_{1,1} \quad (7.150)$$

where $\xi = 2\sqrt{3}C_1$. We find the solution decays exponentially, proportional to $e^{-t/\tau}$, with

$$\frac{1}{\tau} = \xi^2 \left(\frac{\omega^c}{\omega_{21}} \right)^4 \left(\frac{MR^2}{A'} \right) \left(\frac{\omega_C}{\omega^c} \right) d_1. \quad (7.151)$$

Using Eq. (7.135), we define the effective Q for an oscillation at the Chandler frequency to satisfy

$$\frac{1}{Q_C} = \frac{\omega_C d_1}{\omega_{21}^2}, \quad (7.152)$$

then

$$\frac{1}{\tau} = \xi^2 \frac{(\omega^c)^3}{(\omega_{21})^2} \left(\frac{MR^2}{A'} \right) \left(\frac{1}{Q_C} \right). \quad (7.153)$$

The wobble damping timescale is approximately

$$\tau \approx 19.38 \frac{A}{MR^2} \frac{\mu Q_C}{\rho R^2 (\omega^c)^3}. \quad (7.154)$$

This agrees with Peale (1973), though the method of calculation is very different.

7.13 Tidal Friction

Consider a perturbing body in orbit about a dissipative elastic body. We assume the spin axis of the body is perpendicular to the orbit plane ($\gamma' = 0$) and that there is no wobble ($\omega^a = \omega^b = 0$). We will use the same coordinates (θ, ϕ, ψ) to specify the

orientation as before. Let n be the mean motion of the perturbing body, with true longitude λ . We assume that $A' = B'$. We will consider only the gravest elastic mode. With these assumptions the equations of motion are

$$C'\dot{\omega}^c = \sqrt{3}MR^2\mathcal{F}_1(\Pi_{1,2}2\alpha'\beta' - \Pi_{1,-2}((\alpha')^2 - (\beta')^2)) \quad (7.155)$$

$$\dot{\omega}^a = \dot{\omega}^b = 0 \quad (7.156)$$

with

$$\ddot{\Pi}_{1,2} + d_1\dot{\Pi}_{1,2} + \omega_{21}^2\Pi_{1,2} = \mathcal{F}_1\frac{\sqrt{3}}{2}((\alpha')^2 - (\beta')^2) \quad (7.157)$$

$$\ddot{\Pi}_{1,-2} + d_1\dot{\Pi}_{1,-2} + \omega_{21}^2\Pi_{1,-2} = \mathcal{F}_1\frac{\sqrt{3}}{2}2\alpha'\beta' \quad (7.158)$$

$$\Pi_{1,1} = \Pi_{1,-1} = 0. \quad (7.159)$$

with

$$\Pi_{1,0} \approx -(2C_1(\omega^c)^2 + \mathcal{F}_1/2)/\omega_{21}^2. \quad (7.160)$$

The average polar moment is

$$C' = C + 8C_1^2MR^2\left(\frac{\omega^c}{\omega_{21}}\right)^2 + 2C_1MR^2\frac{\mathcal{F}_1}{\omega_{21}^2}. \quad (7.161)$$

For this geometry $\alpha' = \cos(\lambda - \phi)$ and $\beta' = \sin(\lambda - \phi)$, with $\omega^c = \dot{\phi}$. Define $\phi' = \phi - \lambda$, then the equations of motion are

$$C'\dot{\omega}^c = \sqrt{3}MR^2\mathcal{F}_1(-\Pi_{1,2}\sin(2\phi') - \Pi_{1,-2}\cos(2\phi')) \quad (7.162)$$

$$\ddot{\Pi}_{1,2} + d_1\dot{\Pi}_{1,2} + \omega_{21}^2\Pi_{1,2} = \mathcal{F}_1\frac{\sqrt{3}}{2}\cos(2\phi') \quad (7.163)$$

$$\ddot{\Pi}_{1,-2} + d_1\dot{\Pi}_{1,-2} + \omega_{21}^2\Pi_{1,-2} = -\mathcal{F}_1\frac{\sqrt{3}}{2}\sin(2\phi') \quad (7.164)$$

Let's assume that the rotation is not near synchronous, and that ϕ' moves approximately uniformly

$$\phi' \approx (\omega^c - n)t. \quad (7.165)$$

(We are taking the orbital eccentricity to be zero.) Then the Π equations are periodically forced damped harmonic oscillators, with solutions (assuming $\omega_{21} \gg |\omega^c - n|$)

$$\Pi_{1,2} = \frac{\sqrt{3}}{2} \frac{\mathcal{F}_1}{\omega_{21}^2} \cos(2(\omega^c - n)t - \delta_{2\omega^c - 2n}) \quad (7.166)$$

$$\Pi_{1,-2} = -\frac{\sqrt{3}}{2} \frac{\mathcal{F}_1}{\omega_{21}^2} \sin(2(\omega^c - n)t - \delta_{2\omega^c - 2n}) \quad (7.167)$$

where

$$\tan \delta_{2\omega^c - 2n} \approx \frac{2(\omega^c - n)d_1}{\omega_{21}^2} = \frac{1}{Q_T}, \quad (7.168)$$

defining Q_T as the effective Q at the frequency $2(\omega^c - n)$. Substituting these into the equation for $\dot{\omega}^c$ we find

$$\dot{\omega}^c = -\frac{3}{2} \frac{MR^2}{C'} \frac{(\mathcal{F}_1)^2}{\omega_{21}^2} \sin \delta_{2\omega^c - 2n}. \quad (7.169)$$

This gives the rate of deceleration of rotation for a perturber of mass m in a circular orbit. It can apply to either the case of the deceleration of a planet by a satellite or of the rotation of a satellite by the primary. This expression is easily generalized using Eqs. (7.127-7.131).

To reduce this expression to the usual expression we have to make an additional assumption. For one of the factors of \mathcal{F}_1 , we use the approximate form for large rigidity in Eq. (7.105). We also use $k_2 = (3/5)h_2$. We find then

$$\dot{\omega}^c = -\frac{3}{2} \frac{k_2}{Q_T} \left(\frac{R}{R'}\right)^3 \left(\frac{Gm}{a^3}\right) \left(\frac{m}{M}\right) \frac{MR^2}{C'} f, \quad (7.170)$$

where

$$f = 10C_1g_1 \approx 0.98. \quad (7.171)$$

Except for the f factor Eq. (7.170) gives the expression in Goldreich (1966).² We find that $\sum_{i=1}^{\infty} 10C_i g_i = 1$. Therefore we ignore the f factor from here out. In each case m is the tidal perturber, and M is the perturbed solid body.

²The expression given by Peale (1973) is too big by a factor of 2, as noted by Dobrovolskis (2007).

This formula can be applied to get the tidal decay of rotation for a non-synchronous satellite, but also for the tidal evolution of semimajor axis. Assuming the angular momentum of the system is conserved, the angular momentum lost by the rotating body goes into the orbit. We find, using Eq. (7.170), that the rate of tidal evolution of the semimajor axis a of a circular orbit is

$$\frac{1}{a} \frac{da}{dt} = 3n \frac{k_2}{Q_T} \frac{R^5}{a^5} \frac{m}{M}, \quad (7.172)$$

which agrees with Peale (1986).

7.14 Tidal Friction with Eccentricity

Consider a perturbing body in an elliptic orbit about a dissipative elastic body. To start, we will assume the spin axis of the body is perpendicular to the orbit plane ($\gamma' = 0$) and that there is no wobble ($\omega^a = \omega^b = 0$). Let n be the mean motion of the perturbing body, a the semimajor axis, e the orbital eccentricity, ϖ the longitude of pericenter, and λ the true longitude. Following Eqs. (7.162-7.164), the equations of motion are

$$C' \dot{\omega}^c = \sqrt{3} M R^2 \mathcal{F}_1 (-\Pi_{1,2} \sin(2(\phi - \lambda)) - \Pi_{1,-2} \cos(2(\phi - \lambda))) \quad (7.173)$$

$$\ddot{\Pi}_{1,2} + d_1 \dot{\Pi}_{1,2} + \omega_{21}^2 \Pi_{1,2} = \mathcal{F}_1 \frac{\sqrt{3}}{2} \cos(2(\phi - \lambda)) \quad (7.174)$$

$$\ddot{\Pi}_{1,-2} + d_1 \dot{\Pi}_{1,-2} + \omega_{21}^2 \Pi_{1,-2} = -\mathcal{F}_1 \frac{\sqrt{3}}{2} \sin(2(\phi - \lambda)), \quad (7.175)$$

$$\ddot{\Pi}_{1,0} + d_1 \dot{\Pi}_{1,0} + \omega_{21}^2 \Pi_{1,0} = -(2C_1 (\omega^c)^2 + \mathcal{F}_1/2), \quad (7.176)$$

where both \mathcal{F}_1 and λ vary nonuniformly because of the Keplerian orbital motion. Recall that $\mathcal{F}_1 \propto (a/R'(t))^3$ (see Eq. 7.105).

To solve these equations we Fourier expand the periodic forcing. We use

$$\left(\frac{a}{R'(t)} \right)^3 \cos(kf(t)) = \sum_{j=-\infty}^{\infty} X_j^{-3,k}(e) \cos(jnt), \quad (7.177)$$

and

$$\left(\frac{a}{R'(t)}\right)^3 \sin(kf(t)) = \sum_{j=-\infty}^{\infty} X_j^{-3,k}(e) \sin(jnt), \quad (7.178)$$

where f is the true anomaly and $X_j^{-3,2}(e)$ are Hansen functions.

Substituting these into the Π equations of motion gives

$$\ddot{\Pi}_{1,2} + d_1 \dot{\Pi}_{1,2} + \omega_{21}^2 \Pi_{1,2} = \mathcal{G}_1 \frac{\sqrt{3}}{2} \sum_{j=-\infty}^{\infty} X_j^{-3,2}(e) \cos(2\phi - 2\varpi - jnt) \quad (7.179)$$

$$\ddot{\Pi}_{1,-2} + d_1 \dot{\Pi}_{1,-2} + \omega_{21}^2 \Pi_{1,-2} = -\mathcal{G}_1 \frac{\sqrt{3}}{2} \sum_{j=-\infty}^{\infty} X_j^{-3,2}(e) \sin(2\phi - 2\varpi - jnt),$$

$$\ddot{\Pi}_{1,0} + d_1 \dot{\Pi}_{1,0} + \omega_{21}^2 \Pi_{1,0} = -2C_1(\omega^c)^2 - \mathcal{G}_1 \frac{1}{2} \sum_{j=-\infty}^{\infty} X_j^{-3,0}(e) \cos(jnt), \quad (7.180)$$

where $\phi = \phi_0 + \omega^c t$ (with ϕ_0 giving the orientation of the planet at time $t = 0$) and

$$\mathcal{G}_1 \left(\frac{a}{R'(t)}\right)^3 = \mathcal{F}_1. \quad (7.181)$$

These linear equations have the approximate solutions

$$\Pi_{1,2} = \frac{\sqrt{3}}{2} \frac{\mathcal{G}_1}{\omega_{21}^2} \sum_{j=-\infty}^{\infty} X_j^{-3,2}(e) \cos(2\phi - 2\varpi - jnt - \delta_{2\omega^c-jn}) \quad (7.182)$$

$$\Pi_{1,-2} = -\frac{\sqrt{3}}{2} \frac{\mathcal{G}_1}{\omega_{21}^2} \sum_{j=-\infty}^{\infty} X_j^{-3,2}(e) \sin(2\phi - 2\varpi - jnt - \delta_{2\omega^c-jn}) \quad (7.183)$$

$$\Pi_{1,0} = -2C_1 \frac{(w^c)^2}{\omega_{21}^2} - \frac{1}{2} \frac{\mathcal{G}_1}{\omega_{21}^2} \sum_{j=-\infty}^{\infty} X_j^{-3,0}(e) \cos(jnt - \delta_{jn}) \quad (7.184)$$

where

$$\tan \delta_{2\omega^c-jn} \approx \frac{(2\omega^c - jn)d_1}{\omega_{21}^2}, \quad (7.185)$$

$$\tan \delta_{jn} \approx \frac{jnd_1}{\omega_{21}^2}. \quad (7.186)$$

In writing these expressions we have used the approximation that $|2\omega^c - jn| \ll \omega_{21}$. These expressions are easily generalized.

Substituting these expressions into the equation for $\dot{\omega}^c$ and averaging over the orbital period, we find

$$\dot{\omega}^c = -\frac{3}{2} \frac{MR^2}{C'} \frac{(\mathcal{G}_1)^2}{\omega_{21}^2} \sum_{j=-\infty}^{\infty} (X_j^{-3,2}(e))^2 \sin \delta_{2\omega^c - jn}, \quad (7.187)$$

where we have ignored the small time variation in C' which exists because \mathcal{F}_1 (see Eq. 7.161) is now time dependent. Note that $X_0^{-3,2}(e) = 0$. This expression looks more familiar if we assume large rigidity:

$$\dot{\omega}^c = -\frac{3}{2} k_2 \left(\frac{R}{R'} \right)^3 \left(\frac{Gm}{a^3} \right) \left(\frac{m}{M} \right) \frac{MR^2}{C'} \sum_{j=-\infty}^{\infty} (X_j^{-3,2}(e))^2 \sin \delta_{2\omega^c - jn}, \quad (7.188)$$

where we have ignored the factor of f .

Next we compute the total energy dissipation. For the simple driven oscillator the rate of dissipation is given by Eq. (7.129). Generalizing this to our case, where there are many forcing terms, and integrating over an orbit period, we find the average rate of energy dissipation to be

$$\begin{aligned} \frac{dE}{dt} &= \frac{3}{4} \frac{MR^2 \mathcal{G}_1^2}{\omega_{21}^2} \sum_{j=-\infty}^{\infty} (X_j^{-3,2}(e))^2 (2\omega^c - jn) \sin \delta_{2\omega^c - jn} \\ &\quad + \frac{1}{4} \frac{MR^2 \mathcal{G}_1^2}{\omega_{21}^2} \sum_{j=-\infty}^{\infty} (X_j^{-3,0}(e))^2 (jn) \sin \delta_{jn}. \end{aligned} \quad (7.189)$$

For the special case of synchronous rotation we set $\omega^c = n$.

To derive the usual expression for tidal heating in synchronous rotation at low eccentricity, we select the lowest order terms in eccentricity:

$$\frac{dE}{dt} = \frac{21}{2} \frac{MR^2 \mathcal{G}_1^2}{\omega_{21}^2} e^2 \sin \delta_n, \quad (7.190)$$

where $\delta_n = -\delta_{-n} = \delta_{2\omega^c - n} = -\delta_{2\omega^c - 3n}$. To get the familiar formula, we make a large

μ approximation (as before) and find

$$\frac{dE}{dt} = \frac{21}{2} \frac{k_2}{Q} \frac{Gm^2 n R^5}{a^6} e^2, \quad (7.191)$$

where we have again ignored a factor of $f = 0.98$ and approximated $\sin \delta_n$ by $1/Q$. This agrees with Peale & Cassen (1978) and Peale et al. (1979).

For the case of phase lags proportional to frequency we use $\delta_{2\omega^c - jn} = (2 - j)\delta_n$ and $\delta_{jn} = j\delta_n$. Making the large μ approximation again, we derive

$$\frac{dE}{dt} = \frac{21}{2} \frac{k_2}{Q} \frac{Gm^2 n R^5}{a^6} e^2 \eta(e), \quad (7.192)$$

where the tidal heating enhancement factor is

$$\eta(e) = 1 + 18e^2 + \frac{3329}{28}e^4 + \frac{55551}{112}e^6 + \dots. \quad (7.193)$$

This agrees with Peale & Cassen (1978) and Wisdom (2008). Wisdom (2008) gave an expression valid at arbitrary eccentricity:

$$\zeta(e) = e^2 \eta(e) = \frac{2}{7} \frac{f_0(e)}{\beta^{15}} - \frac{4}{7} \frac{f_1(e)}{\beta^{12}} + \frac{2}{7} \frac{f_2(e)}{\beta^9}, \quad (7.194)$$

where

$$\begin{aligned} f_0(e) &= 1 + \frac{31}{2}e^2 + \frac{255}{8}e^4 + \frac{185}{16}e^6 + \frac{25}{64}e^8, \\ f_1(e) &= 1 + \frac{15}{2}e^2 + \frac{45}{8}e^4 + \frac{5}{16}e^6, \\ f_2(e) &= 1 + 3e^2 + \frac{3}{8}e^4, \end{aligned} \quad (7.195)$$

with $\beta = (1 - e^2)^{1/2}$.

7.14.1 Orbital Evolution Not in Spin-Orbit Resonance

Next, we can use conservation of energy and angular momentum with the above results to compute the rates of change of semimajor axis and eccentricity for the case

in which there is no spin-orbit resonance. Based on conservation of energy,

$$\frac{da}{dt} = -\frac{2a^2}{GMm} \left(C\omega^c \dot{\omega}^c + \frac{dE}{dt} \right). \quad (7.196)$$

Substituting in Eq. (7.187) and Eq. (7.189) yields

$$\frac{1}{a} \frac{da}{dt} = \frac{\kappa}{2} \sum_{j=-\infty}^{\infty} j \left(3(X_j^{-3,2}(e))^2 \sin \delta_{2\omega^c-jn} - (X_j^{-3,0}(e))^2 \sin \delta_{jn} \right), \quad (7.197)$$

where

$$\kappa = \frac{a}{GMm} MR^2 \frac{\mathcal{G}_1^2}{\omega_{21}^2} \approx \frac{k_2 n R^5}{a^5} \frac{m}{M}, \quad (7.198)$$

where the approximation is for large rigidity. Conservation of angular momentum gives

$$\begin{aligned} \frac{1}{e} \frac{de}{dt} = & \frac{\kappa}{4} \frac{\sqrt{1-e^2}}{e^2} \left(-\sqrt{1-e^2} \sum_{j=-\infty}^{\infty} (X_j^{-3,0}(e))^2 j \sin \delta_{jn} \right. \\ & \left. + 3 \sum_{j=-\infty}^{\infty} \left(j\sqrt{1-e^2} - 2 \right) (X_j^{-3,2}(e))^2 \sin \delta_{2\omega^c-jn} \right). \end{aligned} \quad (7.199)$$

Note that the leading term in $1/e \, de/dt$ as a polynomial in e is proportional to a constant—the $1/e^2$ factor is cancelled by a leading factor of e^2 in the subsequent expression.

If we keep only the lowest order terms in eccentricity, the expressions reduce to

$$\frac{1}{a} \frac{da}{dt} = 3\kappa \sin \delta_{2\omega^c-2n} \quad (7.200)$$

and

$$\frac{1}{e} \frac{de}{dt} = -\frac{3\kappa}{4} \left(\frac{3}{2} \sin \delta_n + \frac{1}{4} \sin \delta_{2\omega^c-n} + \sin \delta_{2\omega^c-2n} - \frac{49}{4} \sin \delta_{2\omega^c-3n} \right), \quad (7.201)$$

which confirms Equation 7 of Goldreich (1963). (Goldreich's ϵ_3 is actually δ_n , which is associated with frequency n , not $\frac{3}{2}n$, as stated.)

For Mignard tides, where phase lags are proportional to frequency,

$$\begin{aligned} \frac{1}{a} \frac{da}{dt} = & 6 \frac{\kappa}{Q} \left[\left(\frac{\omega^c}{n} - 1 \right) + e^2 \left(\frac{27}{2} \frac{\omega^c}{n} - 23 \right) + e^4 \left(\frac{573}{8} \frac{\omega^c}{n} - 180 \right) \right. \\ & \left. + e^6 \left(\frac{3961}{16} \frac{\omega^c}{n} - \frac{6765}{8} \right) + \dots \right] \end{aligned} \quad (7.202)$$

$$\begin{aligned} \frac{1}{e} \frac{de}{dt} = & \frac{33}{2} \frac{\kappa}{Q} \left[\left(\frac{\omega^c}{n} - \frac{18}{11} \right) + e^2 \left(\frac{13}{2} \frac{\omega^c}{n} - \frac{369}{22} \right) \right. \\ & \left. + e^4 \left(\frac{181}{8} \frac{\omega^c}{n} - \frac{3645}{44} \right) + \dots \right]. \end{aligned} \quad (7.203)$$

7.14.2 Orbital Evolution in Spin-Orbit Resonance

Similar calculations yield the rates of change of semimajor axis and eccentricity in spin-orbit resonance, where $\omega^c = kn$ and therefore

$$\dot{\omega}^c = -\frac{3}{2} k \frac{n}{a} \frac{da}{dt}. \quad (7.204)$$

For the case of a tide-raising perturber orbiting around an extended body,

$$\frac{1}{a} \frac{da}{dt} = \frac{2a}{GMm} (3k^2 \Gamma_m - 1)^{-1} \frac{dE}{dt}, \quad (7.205)$$

with $\Gamma_m = C/(ma^2)$. Substituting in Eq. (7.189) yields

$$\frac{1}{a} \frac{da}{dt} = \frac{\kappa}{2} (3k^2 \Gamma_m - 1)^{-1} \Upsilon, \quad (7.206)$$

where

$$\Upsilon = \sum_{j=-\infty}^{\infty} (3(X_j^{-3,2}(e))^2 (2k-j) \sin \delta_{2\omega^c-jn} + (X_j^{-3,0}(e))^2 j \sin \delta_{jn}). \quad (7.207)$$

Conservation of angular momentum gives

$$\frac{1}{e} \frac{de}{dt} = -\frac{\kappa}{4} \frac{\sqrt{1-e^2}}{e^2} \left(\frac{\sqrt{1-e^2} - 3k\Gamma_m}{1 - 3k^2\Gamma_m} \right) \Upsilon \quad (7.208)$$

Note that the first parenthesized factor in Eq. (7.208) is approximately one for small eccentricity in synchronous rotation, in both the limit that $\Gamma_m = C/(ma^2)$ is large and small compared to one. Both these limits occur in the solar system: for the satellites of the giant planets $\Gamma_m \gg 1$, whereas for the Moon $\Gamma_m \ll 1$.

For the case of an extended body orbiting around a perturbing central mass,

$$\frac{1}{a} \frac{da}{dt} = \frac{\kappa}{2} (3k^2 \Gamma_M - 1)^{-1} \Upsilon, \quad (7.209)$$

with $\Gamma_M = C/(Ma^2)$, and

$$\frac{1}{e} \frac{de}{dt} = -\frac{\kappa}{4} \frac{\sqrt{1-e^2}}{e^2} \left(\frac{\sqrt{1-e^2} - 3k\Gamma_M}{1 - 3k^2\Gamma_M} \right) \Upsilon. \quad (7.210)$$

Note that $\Gamma_M = C/(Ma^2)$ is typically small compared to one.

For Mignard tides we can expand Υ as a power series in e

$$\begin{aligned} \Upsilon = & 12(k-1)^2 + e^2(90k^2 - 324k + 276) + e^4(315k^2 - 1719k + 2160) \\ & + \frac{1}{2}e^6(1575k^2 - 11883k + 20295) + \dots \end{aligned} \quad (7.211)$$

Notice that for synchronous rotation the leading term in Υ is order e^2 , but for other spin-orbit commensurabilities the leading term is a constant. Thus a satellite would not be expected to be in nonsynchronous spin-orbit resonance at low eccentricity. The eccentricity would decay rapidly to zero in finite time and then the resonance lock would be lost.

If we specialize to synchronous rotation ($k=1$) and keep only the lowest order terms in eccentricity, the expressions reduce to

$$\frac{1}{a} \frac{da}{dt} = \frac{3\kappa}{4} e^2 (3\Gamma_m - 1)^{-1} \left(3 \sin \delta_n + \frac{1}{2} \sin \delta_{2\omega^c - n} - \frac{49}{2} \sin \delta_{2\omega^c - 3n} \right) \quad (7.212)$$

for a perturber with mass m orbiting around a synchronous extended body with mass

M and

$$\frac{1}{a} \frac{da}{dt} = \frac{3\kappa}{4} e^2 (3\Gamma_M - 1)^{-1} \left(3 \sin \delta_n + \frac{1}{2} \sin \delta_{2\omega^c - n} - \frac{49}{2} \sin \delta_{2\omega^c - 3n} \right) \quad (7.213)$$

for an extended body with mass M orbiting around a central body with mass m . For Mignard tides, where the phase lags are proportional to frequency, the common factor in parentheses is $28\delta_n$. The rate of change of eccentricity is the same in both cases:

$$\frac{1}{e} \frac{de}{dt} = -\frac{3\kappa}{8} \left(3 \sin \delta_n + \frac{1}{2} \sin \delta_{2\omega^c - n} - \frac{49}{2} \sin \delta_{2\omega^c - 3n} \right), \quad (7.214)$$

which again confirms Equation 8 of Goldreich (1963), if his $2\epsilon_3$ is actually the lag for frequency n , not $\frac{3}{2}n$. For Mignard tides, where the phase lags are proportional to frequency,

$$\frac{1}{e} \frac{de}{dt} = -\frac{21}{2} \frac{\kappa}{Q}. \quad (7.215)$$

7.15 Conclusion

In this chapter, we have laid out the basis for a new tidal formulation that treats solid body tides as the excitation of elastic modes in the body. We derived expressions for wobble damping, tidal dissipation, tidal despinning, and rates of change of semimajor axis and eccentricity. The most interesting result of these derivations is the discovery that the rate of change of semimajor axis and eccentricity are, to lowest order, proportional to e^2 for the synchronous resonance and to a constant for all other spin-orbit resonances. This would imply that we would not find objects in nonsynchronous resonances at low eccentricities because the damping would rapidly drop the eccentricity to zero and break the object out of resonance. This result has only been derived for the constant time lag (Mignard) model so far.

In future work, we plan to extend the model to include inclination and obliquity. We also plan to apply the model to different rheologies with different frequency dependences for the phase lags. Our model will then be relevant and useful for any solid body that evolves, due to tides, over a significant frequency range. We will

be able to compare the evolution of the Moon, icy satellites, and super-Earths in different rheologies and perhaps constrain both the possible evolutions and the likely rheologies.

Chapter 8

Conclusions and Future Work

In this thesis, we have explored tides in general and in specific. We found that tides can have an amazingly transformative effect on satellites.

For Enceladus, we found that the equilibrium tidal heating can be calculated to be $1.1(18,000/Q_S)$ GW, independent of satellite rheology. The actual heat flow on Enceladus is an order of magnitude higher, so we investigated possible orbital and thermal nonequilibrium. We found no evidence of current orbital non-equilibrium and were able to conclude, based on the magnitude of the libration of the resonance angle, that Enceladus is in or near equilibrium in its 2:1 mean motion resonance with Dione (Meyer & Wisdom, 2008b). We also applied the thermal oscillation model of Ojakangas & Stevenson (1986) that produces oscillations around equilibrium for Io and did not find thermal nonequilibrium for Enceladus (Meyer & Wisdom, 2008a).

Recent work by others has focused on other models to produce thermal oscillations (O'Neill & Nimmo, 2010; Běhouňková et al., 2010) and non-tidal sources of heating (Nimmo et al., 2007). However, no model has been able to produce enough heat within the constraints put forward in Meyer & Wisdom (2007). At this point, I believe that the key to understanding Enceladus' mysterious heat flow lies with the Q of Saturn. Conservation of energy and angular momentum forces the heat flow to be less than $1.1(18,000/Q_S)$ GW. We argued in Meyer & Wisdom (2007) that the minimum Q of Saturn is 18,000, based on the orbit of Mimas. A Q_S of 18,000 is what is required for Mimas to begin at the synchronous radius and then evolve outward to

its current orbit. We argued that if Q_S was smaller than 18,000, Mimas would have evolved outward farther than is observed.

However, there are two clear ways to avoid this constraint. First, we are applying a constraint derived from the evolution of the orbit over the age of the solar system. If Q_S is time dependent, such that the current Q_S is an order of magnitude less than the average Q_S of 18,000, we can produce enough heating in equilibrium. Perhaps this time dependence would be due to cooling over time or the precipitation of helium from the upper layers of the atmosphere. Second, the constraint is derived from the orbit of Mimas, not that of Enceladus. Perhaps frequency dependence allows a different Q_S to apply to Enceladus than to Mimas. Theoretical work on the Q of giant planets finds large variations in dissipation over small variations in frequency (Ogilvie & Lin, 2004; Wu, 2005).

Recent astrometric observations by Lainey et al. (2010) have measured the Q of Saturn by directly measuring the orbital changes of Mimas and Enceladus. The methodology is very similar to that in Lainey et al. (2009). They find a very small Q of Saturn, about a factor of 10 smaller than the putative minimum Q of 18,000. If Q is indeed this low, the measured tidal heating is consistent with the amount of tidal heating expected from Meyer & Wisdom (2007). If this measurement of Saturn's Q is verified, it would be exciting confirmation of either time or frequency dependence for dissipation in giant planets.

In addition, we studied tides on the Moon. We found that we could not match the shape solution of Garrick-Bethell et al. (2006) without stretching the terrestrial dissipation parameters to unphysical values (Meyer et al., 2011). In addition, we prove that the Moon would either break or deform and would not maintain the shape from the time of the shape solution until the present (Meyer et al., 2010). Therefore, the shape of the Moon remains an unsolved problem.

Another lunar puzzle, the remanent magnetization of the lunar rocks, motivated our study (Meyer & Wisdom, 2011) of the history of the core precession. We found that inertial coupling would force the core spin axis and mantle spin axis to precess together before the Moon reached a semimajor axis of about 26 to 29 Earth radii.

Until the Moon reaches this point, an early lunar dynamo is precluded. We also note that the Cassini transition occurs after the transition to unlocked core. Perhaps the Cassini transition is the best chance for a powerful dynamo on the Moon. Future work should include an estimate of the power available for the dynamo.

And finally, we have presented a new formulation of solid body tides that treats tidal deformations as the excitation of the elastic modes of the body. There are many promising directions for further research on this subject. We plan to expand the model to include inclined orbits around an oblique extended body. We also plan to include different rheologies. Rheology describes how the material inside the body flows as a response to the tidal perturbation. Geophysicists model the interiors of planets as sets of mass elements, where the motion of each mass element is analogous to the motion of a mass connected to a combination of springs and dashpots.

Our work thus far has modelled the dissipation as a frictional force linearly proportional to the rate of change of the modal coordinate (see Equations 7.125 and 7.136). This corresponds to a simple model in which a spring and dashpot are connected in parallel. This spring-dashpot model is known as the Kelvin-Voigt model and corresponds to phase lags that are linearly proportional to frequency. Therefore, the constant time lag tidal model corresponds to the Kelvin-Voigt rheology.

We have specialized to the constant time lag tidal model only in the last steps of each derivation. To extend our results to other rheologies just involves deriving the appropriate magnitude and phase lag of the tidal response as a function of frequency for whichever tidal models we would like to include. We have so far calculated the magnitude and phase lags for the Maxwell, Standard Linear Solid, and Burgers rheologies. We plan to also compute these quantities for the Andrade model and a generic model with a phase lag that is a simple power law in frequency.

Appendix A

The Resonance Model

We derived our model in a Hamiltonian framework and then added dissipative terms. The Hamiltonian is

$$H = H_K + H_J + H_s + H_r, \quad (\text{A.1})$$

where H_K is the sum of the Kepler Hamiltonians for all the satellites, H_J is the Hamiltonian for the oblateness contributions, H_s is the secular Hamiltonian, and H_r is the resonant Hamiltonian, which has both direct and indirect contributions. Each of these is initially expressed in Jacobi coordinates to effect the elimination of the center of mass (Wisdom & Holman, 1991). We then reexpress each term in terms of canonical Delaunay and then modified Delaunay elements. Finally, we make a polar canonical transformation (Sussman & Wisdom, 2001) on each pair of eccentricity-like momenta and conjugate coordinates to get coordinates that are nonsingular at small eccentricity. The individual steps will not be shown in detail.

The state variables are as follows:

$$h_i = e_i \cos \sigma_i \quad (\text{A.2})$$

$$k_i = e_i \sin \sigma_i \quad (\text{A.3})$$

$$\tilde{a}_i = \Lambda_i^2 / m_i \mu_i, \quad (\text{A.4})$$

where we label the satellites with subscript $i = 0$ for the inner satellite and $i = 1$ for

the outer satellite in the resonant pair. The mass of satellite i is m_i , and $\mu_i = Gm_iM$, where M is the planet mass. The eccentricity of satellite i is e_i . The resonance variables are $\sigma_i = j\lambda_1 + (1-j)\lambda_0 - \varpi_i$, where λ_i and ϖ_i are the mean longitude and longitude of pericenter of satellite i . We also have

$$\Lambda_0 = L_0 - (1-j)(\Sigma_0 + \Sigma_1) \quad (\text{A.5})$$

$$\Lambda_1 = L_1 - j(\Sigma_0 + \Sigma_1), \quad (\text{A.6})$$

where $L_i = \sqrt{m_i\mu_i a_i}$, for semimajor axis a_i , and

$$\Sigma_i = \sqrt{m_i\mu_i a_i}(1 - (1 - e_i^2)^{1/2}) \approx \Lambda_i e_i^2/2, \quad (\text{A.7})$$

where $L_i \approx \Lambda_i$ to first order in eccentricity. We define $\Sigma_i = \Lambda_i \bar{\Sigma}_i$. Note that in the absence of tides the state variables \tilde{a}_i and the associated variables Λ_i are constants of the motion. The osculating semimajor axes a_i and the associated L_i are not constant.

Let

$$\frac{\partial H_K}{\partial \Sigma_i} = (1-j)n_0 + jn_1, \quad (\text{A.8})$$

where the mean motions are $n_0 = m_0\mu_0^2/L_0^3$ and $n_1 = m_1\mu_1^2/L_1^3$. We also define $\tilde{n}_0 = m_0\mu_0^2/\Lambda_0^3$ and $\tilde{n}_1 = m_1\mu_1^2/\Lambda_1^3$. In terms of these, we define

$$\Delta n_0 = \tilde{n}_0 \left(3 \frac{J_2 R^2}{\tilde{a}_0^2} + \frac{45}{4} \frac{J_2^2 R^4}{\tilde{a}_0^4} - \frac{15}{4} \frac{J_4 R^4}{\tilde{a}_0^4} \right) \quad (\text{A.9})$$

$$\Delta n_1 = \tilde{n}_1 \left(3 \frac{J_2 R^2}{\tilde{a}_1^2} + \frac{45}{4} \frac{J_2^2 R^4}{\tilde{a}_1^4} - \frac{15}{4} \frac{J_4 R^4}{\tilde{a}_1^4} \right) \quad (\text{A.10})$$

$$\Delta \dot{\varpi}_0 = \tilde{n}_0 \left(\frac{3}{2} \frac{J_2 R^2}{\tilde{a}_0^2} + \frac{63}{8} \frac{J_2^2 R^4}{\tilde{a}_0^4} - \frac{15}{4} \frac{J_4 R^4}{\tilde{a}_0^4} \right) \quad (\text{A.11})$$

$$\Delta \dot{\varpi}_1 = \tilde{n}_1 \left(\frac{3}{2} \frac{J_2 R^2}{\tilde{a}_1^2} + \frac{63}{8} \frac{J_2^2 R^4}{\tilde{a}_1^4} - \frac{15}{4} \frac{J_4 R^4}{\tilde{a}_1^4} \right) \quad (\text{A.12})$$

These are the changes in the mean motions and the changes in the rates of precession of the pericenters due to planetary oblateness (Brouwer, 1959).

Next we define

$$\Delta \dot{\sigma}_0 = (1-j)\Delta n_0 + j\Delta n_1 - \Delta \dot{\varpi}_0 \quad (\text{A.13})$$

and

$$\Delta\dot{\sigma}_1 = (1-j)\Delta n_0 + j\Delta n_1 - \Delta\dot{\omega}_1. \quad (\text{A.14})$$

These are the changes in the rates of change of the resonant arguments due to planetary oblateness.

The equations of motion are as follows:

$$\begin{aligned} \frac{dk_0}{dt} &= \frac{\partial H_K}{\partial \Sigma_0} h_0 + \Delta\dot{\sigma}_0 h_0 \\ &\quad - \frac{Gm_0 m_1}{\tilde{a}_1 \Lambda_0} (C_{ee'}^s h_1 + 2C_{ee}^s h_0 + C_e^r + 2C_{ee}^r h_0 + C_{ee'}^r h_1) + \left. \frac{dk_0}{dt} \right|_t \end{aligned} \quad (\text{A.15})$$

$$\begin{aligned} \frac{dh_0}{dt} &= -\frac{\partial H_K}{\partial \Sigma_0} k_0 - \Delta\dot{\sigma}_0 k_0 \\ &\quad - \frac{Gm_0 m_1}{\tilde{a}_1 \Lambda_0} (-C_{ee'}^s k_1 - 2C_{ee}^s k_0 + 2C_{ee}^r k_0 + C_{ee'}^r k_1) + \left. \frac{dh_0}{dt} \right|_t \end{aligned} \quad (\text{A.16})$$

$$\begin{aligned} \frac{dk_1}{dt} &= \frac{\partial H_K}{\partial \Sigma_1} h_1 + \Delta\dot{\sigma}_1 h_1 \\ &\quad - \frac{Gm_0 m_1}{\tilde{a}_1 \Lambda_1} (2C_{e'e'}^s h_1 + C_{ee'}^s h_0 + C_{e'}^r + 2C_{e'e'}^r h_1 + C_{ee'}^r h_0) + \left. \frac{dk_1}{dt} \right|_t \end{aligned} \quad (\text{A.17})$$

$$\begin{aligned} \frac{dh_1}{dt} &= -\frac{\partial H_K}{\partial \Sigma_1} k_1 - \Delta\dot{\sigma}_1 k_1 \\ &\quad - \frac{Gm_0 m_1}{\tilde{a}_1 \Lambda_1} (-2C_{e'e'}^s k_1 - C_{ee'}^s k_0 + 2C_{e'e'}^r k_1 + C_{ee'}^r k_0) + \left. \frac{dh_1}{dt} \right|_t. \end{aligned} \quad (\text{A.18})$$

The tidal damping terms for satellite i are

$$\left. \frac{dk_i}{dt} \right|_t = -\frac{7}{2} c_i D_i a_i^{-13/2} k_i \eta \quad (\text{A.19})$$

$$\left. \frac{dh_i}{dt} \right|_t = -\frac{7}{2} c_i D_i a_i^{-13/2} h_i \eta \quad (\text{A.20})$$

where

$$c_i = 3 \frac{k_2}{Q} \frac{m_0}{M} \sqrt{GM} R^5 \quad (\text{A.21})$$

and

$$D_i = \frac{k_{2i}/Q_i}{k_2/Q} \left(\frac{M}{m_i} \right)^2 \left(\frac{R_i}{R} \right)^5. \quad (\text{A.22})$$

The factor η is a “speedup” factor that artificially enhances the rate of tidal evolution. We found in selected test evolutions that the evolution was insensitive to the speedup factor over a range of speedups of 1 to 1000. We typically used a speedup of 100 in our numerical explorations.

The tidal contribution to the rate of change of semimajor axis a_i is

$$\left. \frac{da_i}{dt} \right|_t = c_i(1 - 7D_i e_i^2) a^{-11/2} \eta. \quad (\text{A.23})$$

From $L_i = \sqrt{m_i \mu_i a_i}$ we have

$$\dot{L}_i^t = \left. \frac{dL_i}{dt} \right|_t = \frac{L_i}{2a_i} \left. \frac{da_i}{dt} \right|_t. \quad (\text{A.24})$$

From $\bar{\Sigma}_i = (h_i^2 + k_i^2)/2$ we have

$$\dot{\bar{\Sigma}}_i^t = \left. \frac{d\bar{\Sigma}_i}{dt} \right|_t = h_i \left. \frac{dh_i}{dt} \right|_t + k_i \left. \frac{dk_i}{dt} \right|_t. \quad (\text{A.25})$$

From the definitions

$$\Lambda_0 = L_0 - (1 - j)(\Lambda_0 \bar{\Sigma}_0 + \Lambda_1 \bar{\Sigma}_1) \quad (\text{A.26})$$

$$\Lambda_1 = L_1 - j(\Lambda_0 \bar{\Sigma}_0 + \Lambda_1 \bar{\Sigma}_1) \quad (\text{A.27})$$

we differentiate to get

$$\dot{\Lambda}_0^t = \dot{L}_0^t - (1 - j) \left(\dot{\Lambda}_0^t \bar{\Sigma}_0 + \dot{\Lambda}_1^t \bar{\Sigma}_1 + \Lambda_0 \dot{\bar{\Sigma}}_0^t + \Lambda_1 \dot{\bar{\Sigma}}_1^t \right) \quad (\text{A.28})$$

$$\dot{\Lambda}_1^t = \dot{L}_1^t - j \left(\dot{\Lambda}_0^t \bar{\Sigma}_0 + \dot{\Lambda}_1^t \bar{\Sigma}_1 + \Lambda_0 \dot{\bar{\Sigma}}_0^t + \Lambda_1 \dot{\bar{\Sigma}}_1^t \right). \quad (\text{A.29})$$

Note that the nontidal contributions to \dot{L}_i and $\dot{\bar{\Sigma}}_i$ cancel because Λ_i are constant except for the tidal terms. Then we solve for $\dot{\Lambda}_0^t$ and $\dot{\Lambda}_1^t$,

$$\dot{\Lambda}_0^t = \frac{(1 + j \bar{\Sigma}_1) \dot{L}_0^t - (1 - j) \Lambda_0 \dot{\bar{\Sigma}}_0^t - (1 - j) \Lambda_1 \dot{\bar{\Sigma}}_1^t - (1 - j) \dot{L}_1^t \bar{\Sigma}_1}{1 + (1 - j) \bar{\Sigma}_0 + j \bar{\Sigma}_1} \quad (\text{A.30})$$

$$\dot{\Lambda}_1^t = \frac{(1 + (1 - j)\bar{\Sigma}_0)\dot{L}_1^t - j\Lambda_0\dot{\bar{\Sigma}}_0^t - j\Lambda_1\dot{\bar{\Sigma}}_1^t - j\dot{L}_0^t\bar{\Sigma}_0}{1 + (1 - j)\bar{\Sigma}_0 + j\bar{\Sigma}_1}. \quad (\text{A.31})$$

And finally, from here, we use the definition of $\tilde{a}_i = \sqrt{m_i\mu_i\Lambda_i}$ to get the rate of change of the state variables \tilde{a}_i .

$$\frac{d\tilde{a}_i}{dt} = 2\frac{\tilde{a}_i}{\Lambda_i}\dot{\Lambda}_i^t \quad (\text{A.32})$$

The disturbing function coefficients are as follows:

$$C_{ee}^s = C_{e'e'}^s = \frac{1}{8} (2D_\alpha b_{1/2}^0(\alpha) + D_\alpha^2 b_{1/2}^0(\alpha)) \quad (\text{A.33})$$

$$C_{ee'}^s = \frac{1}{4} (2b_{1/2}^1(\alpha) - 2D_\alpha b_{1/2}^1(\alpha) - D_\alpha^2 b_{1/2}^1(\alpha)) \quad (\text{A.34})$$

$$C_e^r = \frac{1}{2} (-2jb_{1/2}^j(\alpha) - D_\alpha b_{1/2}^j(\alpha)) \quad (\text{A.35})$$

$$C_{e'}^r = \frac{1}{2} ((2j - 1)b_{1/2}^{j-1}(\alpha) + D_\alpha b_{1/2}^{j-1}(\alpha)) - 2\alpha\delta_{j2} \quad (\text{A.36})$$

$$C_{ee}^r = \frac{1}{8} ((-5k + 4k^2)b_{1/2}^k(\alpha) + (-2 + 4k)D_\alpha b_{1/2}^k(\alpha) + D_\alpha^2 b_{1/2}^k(\alpha)) \quad (\text{A.37})$$

$$C_{ee'}^r = \frac{1}{4} ((-2 + 6k - 4k^2)b_{1/2}^{k-1}(\alpha) + (2 - 4k)D_\alpha b_{1/2}^{k-1}(\alpha) - D_\alpha^2 b_{1/2}^{k-1}(\alpha)) \quad (\text{A.38})$$

$$C_{e'e'}^r = \frac{1}{8} ((2 - 7k + 4k^2)b_{1/2}^{k-2}(\alpha) + (-2 + 4k)D_\alpha b_{1/2}^{k-2}(\alpha) + D_\alpha^2 b_{1/2}^{k-2}(\alpha)) \quad (\text{A.39})$$

where $D_\alpha f = \alpha df/d\alpha$, $k = 2j$, and $b_l^m(\alpha)$ are the usual Laplace coefficients (Murray & Harper, 1993). We have evaluated the coefficients at $\alpha = ((j - 1)/j)^{2/3}$.

Appendix B

Tidal Heating in a Two-Layer Model

In a classic paper Peale and Cassen (1978) calculated the rate and distribution of tidal dissipation in the Moon. They also calculated the rate of tidal heating in a two-layer model, consisting of an inviscid molten interior overlain by a rigid lid. The result was used in another classic paper, Peale, Cassen, and Reynolds (1979), in which it was predicted that there would be volcanoes on Io. We set out to use the two layer model, but found that there were a number of typographical errors, and that a considerable amount of work was required to recover explicit expressions for the local energy dissipation. So the result of our labor is presented here.

The two-layer model consists of an inviscid fluid interior overlain by a rigid lid. The lid has rigidity μ , density ρ , and surface gravity g . The radius of the satellite is R , G is Newton's constant, a is the semimajor axis of the orbit, e is orbital eccentricity, and n is orbital mean motion. The radius of the interior divided by the radius of the satellite is η .

Let

$$A(a, b) = (a(1 + \eta + \eta^2) + b(\eta^3 + \eta^4))/E \quad (\text{B.1})$$

$$B(c, d) = (c(1 + \eta + \eta^2 + \eta^3 + \eta^4) + d(\eta^5 + \eta^6))/E \quad (\text{B.2})$$

$$C(e, f) = (e(\eta^3 + \eta^4) + f(\eta^5 + \eta^6 + \eta^7 + \eta^8 + \eta^9))/E \quad (\text{B.3})$$

$$D(g, h) = (g(\eta^5 + \eta^6) + h(\eta^7 + \eta^8 + \eta^9))/E, \quad (\text{B.4})$$

where $E = 252(1 + \eta + \eta^2) + 672(\eta^3 + \eta^4)$. Then, define

$$\alpha_0 = A(-108, -288)r_1^2 + B(96, 180) + C(-320, -152)r_1^{-3} + D(384, 114)r_1^{-5} \quad (\text{B.5})$$

$$\alpha_1 = A(-30, -80)r_1^2 + B(48, 90) + C(0, 0)r_1^{-3} + D(32, 19/2)r_1^{-5} \quad (\text{B.6})$$

$$\alpha_2 = A(-36, -96)r_1^2 + B(96, 180) + C(160, 76)r_1^{-3} + D(-96, -57/2)r_1^{-5} \quad (\text{B.7})$$

$$\alpha_3 = A(-48, -128)r_1^2 + B(48, 90) + C(80, 38)r_1^{-3} + D(-128, -38)r_1^{-5} \quad (\text{B.8})$$

Note that $A(-108, -288) = -3/7$, $A(-30, -80) = -5/42$, $A(-36, -96) = -1/7$, and $A(-48, -128) = -4/21$. We find that the coefficient of r_1^{-3} in α_3 is a factor of 2 smaller than is given in Peale and Cassen (1978). Otherwise, these expressions reproduce the numbers given in the appendix of Peale and Cassen (1978).

Also, let

$$G(x) = F(19, 64, 64, 24) + xF(-228, 672, -672, 228), \quad (\text{B.9})$$

where $x = \mu/(\rho g R)$, for rigidity μ , density ρ , surface gravity g , and radius R , and where

$$F(a, b, c, d) = a(\eta^7 + \eta^8 + \eta^9) + b(\eta^5 + \eta^6) + c(\eta^3 + \eta^4) + d(1 + \eta + \eta^2), \quad (\text{B.10})$$

then define

$$k'_2(x) = E/G(x). \quad (\text{B.11})$$

For $\mu = 6.5 \times 10^{11}$, $\rho = 3.34$, $g = 162.$, and $R = 1.738 \times 10^8$ (all in cgs), we find $k'_2 = 0.2649$, for $\eta = 1/2$, and $k'_2 = 2.027$, for $\eta = 0.95$, which are in satisfactory agreement with the appendix in Peale and Cassen (1978).

Algebraically, the choice of E is arbitrary, since the strain depends on the product of k'_2 and the α_i and this product is independent of E . Given the notation k'_2 one

might have expected it to reduce to the Love number k_2 for a homogeneous body when $\eta = 0$, but this is not the case. For $\eta = 0$, $k'_2(x) = (21/2)/(1 + (19/2)x) = 7k_2$. So the reason for the choice of the factor E is a mystery; it looks like it should have had $1/7$ the value it was given. Hence, we will choose $E' = E/7$. Define $A' = 7A$, $B' = 7B$, $C' = 7C$, and $D' = 7D$, then $\alpha'_i = 7\alpha_i$. And then we can set $k_2(x) = k'_2(x)/7$. This $k_2(x)$ has the expected value $(3/2)/(1 + (19/2)x)$ for $\eta = 0$. And the coefficients in Equations (10)-(15) in Peale and Cassen (1978) can be recognized as α'_i for $\eta = 0$.

The strains are:

$$e_{rr} = \frac{k_2 R}{g} \sum_{m,p,q} \alpha'_0(r_1) \left(\frac{V_{2mpq}}{r^2} \right) \quad (\text{B.12})$$

$$e_{\theta\theta} = \frac{k_2 R}{g} \sum_{m,p,q} \left[\alpha'_1(r_1) \frac{\partial^2}{\partial \theta^2} \left(\frac{V_{2mpq}}{r^2} \right) + \alpha'_2(r_1) \left(\frac{V_{2mpq}}{r^2} \right) \right] \quad (\text{B.13})$$

$$e_{\phi\phi} = \frac{k_2 R}{g} \sum_{m,p,q} \left[\alpha'_1(r_1) \left(\frac{-m^2}{\sin^2 \theta} + \cot \theta \frac{\partial}{\partial \theta} \right) \left(\frac{V_{2mpq}}{r^2} \right) + \alpha'_2(r_1) \left(\frac{V_{2mpq}}{r^2} \right) \right] \quad (\text{B.14})$$

$$e_{r\theta} = \frac{k_2 R}{g} \sum_{m,p,q} \alpha'_3(r_1) \frac{\partial}{\partial \theta} \left(\frac{V_{2mpq}}{r^2} \right) \quad (\text{B.15})$$

$$e_{r\phi} = \frac{k_2 R}{g} \sum_{m,p,q} \alpha'_3(r_1) \frac{1}{\sin \theta} \frac{\partial}{\partial \phi} \left(\frac{V_{2mpq}}{r^2} \right) \quad (\text{B.16})$$

$$e_{\theta\phi} = \frac{k_2 R}{g} \sum_{m,p,q} \left[\frac{\alpha'_1(r_1)}{\sin \theta} \left(\frac{\partial^2}{\partial \theta \partial \phi} - \cot \theta \frac{\partial}{\partial \phi} \right) \left(\frac{V_{2mpq}}{r^2} \right) \right]. \quad (\text{B.17})$$

This corrects a typo in Eq. (B.16) in Peale and Cassen (1978).

Given the strains, we can compute the local rate of energy dissipation per unit mass and, by integration, the total rate of energy dissipation. The local rate of energy dissipation is, from Peale and Cassen (1978), Eq. (17),

$$H = \sum_{ij} 2\mu e_{ij} \dot{e}_{ij}^*, \quad (\text{B.18})$$

where the dot indicates time derivative and the $*$ indicates that the phase of each term is given a phase lag of $1/Q_{2mpq}$. Keeping only the potential terms $(lmpq) = (2, 0, 1, 1)$, $(2, 0, 1, -1)$, $(2, 2, 0, 1)$, and $(2, 2, 0, -1)$, which are the most important terms for

synchronous rotation in an eccentric non-inclined orbit, we find that the integral of the local dissipation over angles gives

$$\frac{dE_r}{dt} = \frac{2\pi 2\mu G^2 M^2 e^2 k_2^2 R^2 n}{a^6 Q g^2} \left(-126(\alpha'_1)^2 + \frac{252}{5}\alpha'_1\alpha'_2 - \frac{42}{5}(\alpha'_2)^2 - \frac{21}{5}(\alpha'_0)^2 - \frac{252}{5}(\alpha'_3)^2 \right). \quad (\text{B.19})$$

In this case all the phase lags have the same frequency, so we assume they have the same magnitude.

For $\eta = 0$ this becomes

$$\left. \frac{dE_r}{dt} \right|_{\eta=0} = \frac{2\pi 2\mu G^2 M^2 e^2 k_2^2 R^2 n}{a^6 Q g^2} \left(224 + -392r_1^2 + \frac{1813}{10}r_1^4 \right), \quad (\text{B.20})$$

where $r_1 = r/R$. Multiplying by r^2 and integrating from 0 to R , gives the total rate of energy dissipation

$$\left. \frac{dE}{dt} \right|_{\eta=0} = \frac{2\pi 2\mu G^2 M^2 e^2 k_2^2 R^5 n}{a^6 Q g^2} \frac{133}{6}. \quad (\text{B.21})$$

Using $g = Gm/R^2$, where $m = (4/3)\pi\rho R^3$, and replacing one factor of k_2 by $(3/2)/(1+(19/2)x)$, which for large $x = \mu/(2\rho g R)$ becomes

$$k_2 \approx \frac{3\rho g R}{19\mu}, \quad (\text{B.22})$$

we obtain

$$\left. \frac{dE}{dt} \right|_{\eta=0} = \frac{21}{2} \frac{GM^2 e^2 R^5 n}{a^6} \frac{k_2}{Q}. \quad (\text{B.23})$$

This is the usual expression for tidal heating (Peale and Cassen, 1978, see also Wisdom 2004, 2008). Note that we had to make a large μ approximation to get it.

More generally, the angle integrated rate of tidal dissipation is given by Eq. (B.19). The radial integral can be done analytically, but the expression is complicated, so will not be displayed. Figure 5-6 shows the total tidal heating in the two-layer model as a function of η , for Io parameters ($R = 1.821 \times 10^8$, $\rho = 3.53$, $g = 179.71$, $\mu = 6.5 \times 10^{11}$, in cgs). This recalculates Figure 5-6 from Peale, Cassen, and Reynolds (1979). The

agreement is not perfect, but they do not give the assumed values of their parameters, and there was a factor of 2 error (typographical error?) in one of their coefficients.

Appendix C

Transition from Locked to Unlocked Core

We consider here a simple model that illustrates and illuminates the transition from locked to unlocked core. Our model system is a core-mantle system perturbed by a third body. We assume the orbital period is long enough compared to the natural periods of the core-mantle system that the potential interaction can be averaged over the orbit. We assume the orbit is fixed and circular, with zero inclination to the ecliptic. For the real Moon the orbit is slightly inclined and regresses with an 18.6 year period, and the regression of the mantle of the Moon is locked to the regression of the orbit. In this simple model the mantle regresses uniformly at a rate determined by its obliquity and moments.

Following Touma & Wisdom (2001), we describe the core-mantle system, with zero amplitude wobble, by the Hamiltonian

$$H_{CM}(t, \theta, \Theta) = \omega_c \Theta + \frac{1}{2} k \Theta^2, \quad (\text{C.1})$$

where, as before,

$$\omega_c = f_c \omega \frac{C}{C_m} \quad (\text{C.2})$$

is the precession frequency of the core tilt mode, f_c is the core flattening, ω is the

rotational angular frequency, C is the principal moment of the body, and C_m is the principal moment of the mantle. The nonlinearity parameter is

$$k = -\frac{f_c}{\delta C} \left[\frac{1 - 2\delta^2 + \delta^3}{(1 - \delta)^3} \right], \quad (\text{C.3})$$

where $\delta = C_c/C$, where C_c is the principal moment of the core. Note that the nonlinearity parameter is large for both small and large core. Let g' be the angle that measures the direction of the tilted core in inertial space. The canonical coordinate $\theta = -g'$. The canonical momentum Θ is a measure of the tilt J of the symmetry axis of the core-mantle boundary from the angular momentum of the body. We have

$$\sin^2 J = \frac{2G'}{C\omega}, \quad (\text{C.4})$$

with

$$G' = (c^2/D)\Theta, \quad (\text{C.5})$$

where $c = -\sqrt{\delta}$ and $D = 1 - c^2$. The tilt K of the core rotation axis from the symmetry axis of the body is approximately $K = J/\delta$. See Touma & Wisdom (2001) for more details.

Again following Touma & Wisdom (2001), the potential energy is

$$n^2(C - A)P_2(\cos \theta_s), \quad (\text{C.6})$$

where n is the mean orbital motion, C and A are the largest and smallest principal moments of the core-mantle body, and θ_s is the angle from the symmetry axis of the mantle to the perturbing body. The complete expression for the potential can be found in Touma & Wisdom (2001). Averaging over the orbital period is straightforward and simpler than the analysis in Touma & Wisdom (2001) because we are taking the orbit to be circular. The resulting averaged potential energy is

$$n^2(C - A) \left[-\frac{1}{2} + \frac{3}{8} \cos^2 I \sin^2 J + \frac{3}{4} \cos^2 J \sin^2 I + \frac{3}{8} \sin^2 J \right]$$

$$+ \frac{3}{2} \cos I \cos J \sin I \sin J \cos(f' - g') - \frac{3}{8} \sin^2 I \sin^2 J \cos(2f' - 2g') \Big], \quad (\text{C.7})$$

where I is the obliquity of the symmetry axis of the body to inertial z -axis (which is perpendicular to the fixed orbit plane), and f' is the angle of the ascending node of the equator on the orbit plane. The precession of the body is largely independent of the core mode dynamics, so we take the obliquity to be fixed, and $f' = -\omega_f t$, where the rate of regression of the equator is

$$\omega_f = \frac{3}{2} \frac{n^2(C - A)}{C\omega} \cos I. \quad (\text{C.8})$$

The fact that the angles only appear in the combination $f' - g'$ and that f' is uniformly regressing suggests a transformation to a rotating frame. We choose a new coordinate $\theta' = f' - g' = \theta - \omega_f t$ with canonical momentum $\Theta' = \Theta$. Finally, we use the non-singular canonical variables

$$y = \sqrt{2\Theta'} \sin \theta' \quad (\text{C.9})$$

$$x = \sqrt{2\Theta'} \cos \theta'. \quad (\text{C.10})$$

The Hamiltonian is

$$\begin{aligned} H(t, y, x) = & (\omega_c - \omega_f) \frac{x^2 + y^2}{2} + \frac{1}{2} k \left(\frac{x^2 + y^2}{2} \right)^2 + \\ & + n^2(C - A) \left[\frac{3}{2} (\cos I \sin I) \alpha x + \right. \\ & + \left(\frac{3}{4} - \frac{9}{8} \cos^2 I \right) \alpha^2 (x^2 + y^2) - \frac{3}{8} (\sin^2 I) \alpha^2 (x^2 - y^2) \\ & \left. - \frac{3}{4} (\cos I \sin I) \alpha^3 x (x^2 + y^2) \right] \end{aligned} \quad (\text{C.11})$$

where $\alpha = \sqrt{\delta / ((1 - \delta)C\omega)}$, and we have left out some constant terms. Note that we used the approximation $\cos J = 1 - (\sin^2 J)/2$, as J is small. Note that though J remains small, K can be large.

We carried out a numerical experiment to track the fixed points of the system

as we varied the core flattening. We used parameters for the Moon, as given in the body of the text. We integrated the equations of motion with the Bulirsch-Stoer algorithm. We added a small dissipation so that the system would settle on the fixed points. We started the integrations with initial conditions for x and y very close to zero. Figure C-1 shows the magnitude of K for the resulting fixed points as a function of the core flattening. We see that for large flattening the offset of the core to the mantle symmetry axis goes to zero. For ω_c near ω_f the system passes through a resonance and there is large offset of the core to the mantle. Then for small core flattening the core is offset from the mantle by the obliquity $K = I$.

The pattern of bifurcations and fixed points on the phase portraits (the trajectories in the $x - y$ plane) are those of a first order resonance. We can obtain the standard approximate Hamiltonian for a first order resonance by keeping only the first three terms in the Hamiltonian. The resonance is between the precession of the core and the precession of the equator. We obtain

$$H(t, y, x) = (\omega_c - \omega_f) \left(\frac{x^2 + y^2}{2} \right) + \frac{1}{2}k \left(\frac{x^2 + y^2}{2} \right)^2 + n^2(C - A)\frac{3}{2}(\cos I \sin I)\alpha x \quad (\text{C.12})$$

Using this approximate Hamiltonian we can derive the limiting values of the fixed points for small and large core flattening. The fixed points are on the $y = 0$ axis, and satisfy

$$0 = \frac{\partial H}{\partial x} = (\omega_c - \omega_f)x + \frac{1}{2}kx^3 + n^2(C - A)\frac{3}{2}(\cos I \sin I)\alpha. \quad (\text{C.13})$$

Away from resonance we can ignore the nonlinearity term (i.e. set $k = 0$), and find the fixed points to be

$$x = -\frac{n^2(C - A)\frac{3}{2}(\cos I \sin I)\alpha}{\omega_c - \omega_f}. \quad (\text{C.14})$$

For small flattening, $\omega_c \ll \omega_f$ and we find

$$\sin K = \sin I, \quad (\text{C.15})$$

exactly. So the core spin axis is offset from the mantle symmetry axis by the obliquity,

and thus is normal to the orbit plane. In the other limit of large flattening, $\omega_c \gg \omega_f$, and therefore the fixed point approaches zero.

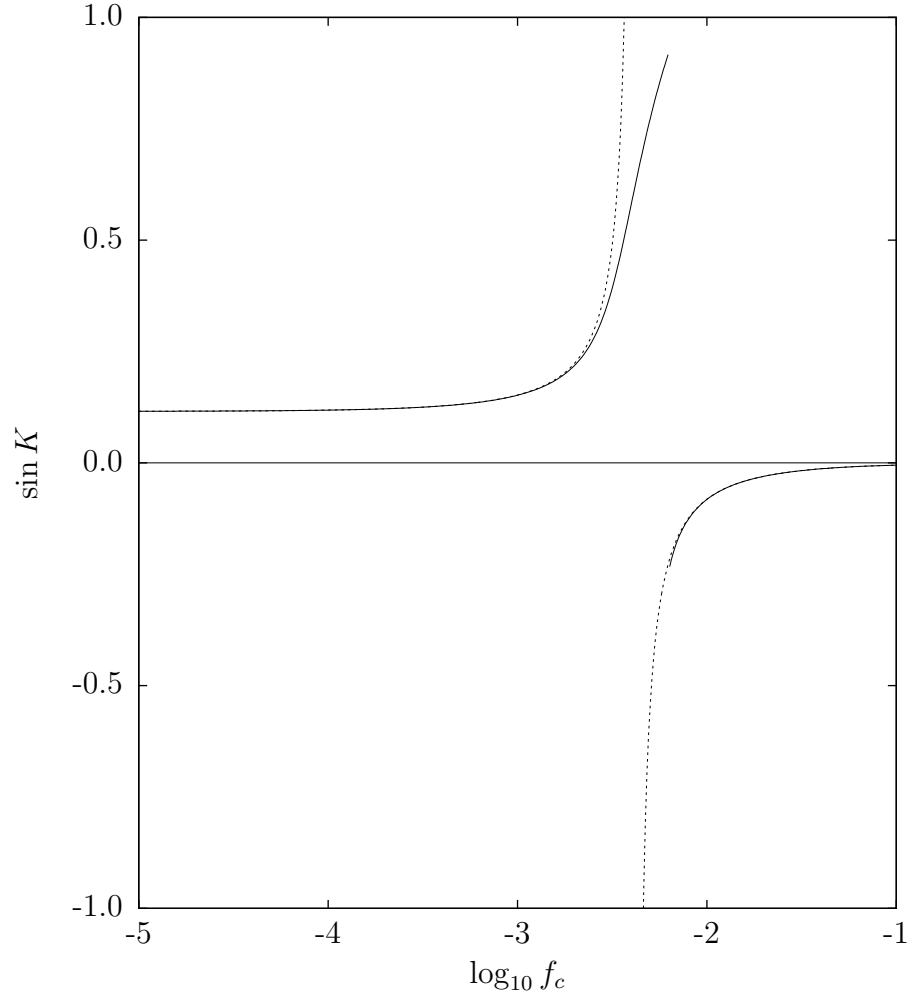


Figure C-1: The offset of the core spin axis from the mantle symmetry axis is plotted versus the core flattening for the equilibrium points of the system. The equilibrium points are found by adding a small dissipation and integrating the equations of motion. Two broken curves are shown. For the solid curve the full resonance Hamiltonian was used; for the dotted curve the nonlinearity parameter k was set to zero. For small flattening the offset of the core is approximately the obliquity; the core spin axis is perpendicular to the orbit. For large flattening, the offset tends to zero; the core spin axis is locked to the mantle.

Appendix D

Surface and Solid Spherical Harmonics

We will use the terms “solid spherical harmonic” and “surface spherical harmonic.” The normalized surface spherical harmonics are

$$C_l^m(\theta, \phi) = P_l^m(\cos \theta) \cos(m\phi) \quad (\text{D.1})$$

$$S_l^m(\theta, \phi) = P_l^m(\cos \theta) \sin(m\phi), \quad (\text{D.2})$$

where the normalized associated Legendre polynomials satisfy

$$P_l^m(x) = N_l^m P_{lm}(x), \quad (\text{D.3})$$

with

$$N_l^m = \left[(2 - \delta_{m,0})(2l+1) \frac{(l-m)!}{(l+m)!} \right]^{1/2}, \quad (\text{D.4})$$

and

$$P_{lm}(x) = \frac{1}{2^l l!} (1-x^2)^{m/2} \frac{d^{l+m}}{dx^{l+m}} [(x^2-1)^l]. \quad (\text{D.5})$$

A few of the P_{lm} are

$$P_{20}(\cos \theta) = \frac{3}{2}(\cos \theta)^2 - \frac{1}{2} \quad (\text{D.6})$$

$$P_{21}(\cos \theta) = 3 \sin \theta \cos \theta \quad (\text{D.7})$$

$$P_{22}(\cos \theta) = 3(\sin \theta)^2. \quad (\text{D.8})$$

For convenience we introduce

$$\begin{aligned} X_l^m(\theta, \phi) &= C_l^m(\theta, \phi) & m \geq 0 \\ &= S_l^{-m}(\theta, \phi) & m < 0 \end{aligned} \quad (\text{D.9})$$

The X_l^m (C_l^m and S_l^m) are orthonormal in that

$$\delta_{ll'} \delta_{mm'} = \frac{1}{4\pi} \int_0^\pi \int_0^{2\pi} X_l^m(\theta, \phi) X_{l'}^{m'}(\theta, \phi) \sin \theta d\theta d\phi. \quad (\text{D.10})$$

The solid spherical harmonics are

$$\tilde{X}_l^m \left(\frac{x}{R}, \frac{y}{R}, \frac{z}{R} \right) = \left(\frac{r}{R} \right)^l X_l^m(\theta, \phi), \quad (\text{D.11})$$

where $r^2 = x^2 + y^2 + z^2$, $\cos \theta = z/r$, $\phi = \text{atan}(y, x)$. The solid harmonics satisfy the orthogonality relations

$$\begin{aligned} & \frac{\delta_{ll'} \delta_{mm'}}{2l+3} \\ &= \frac{1}{4\pi R^3} \int_0^a \int_0^\pi \int_0^{2\pi} \tilde{X}_l^m \left(\frac{x}{R}, \frac{y}{R}, \frac{z}{R} \right) \tilde{X}_{l'}^{m'} \left(\frac{x}{R}, \frac{y}{R}, \frac{z}{R} \right) r^2 \sin \theta dr d\theta d\phi \\ &= \frac{1}{4\pi a^3} \int_V \tilde{X}_l^m \tilde{X}_{l'}^{m'} dV, \end{aligned} \quad (\text{D.12})$$

where the V is the sphere of radius R , and the last line introduces an abbreviated notation.¹

It is convenient to introduce

$$\bar{X}_l^m = \frac{1}{\sqrt{2l+1}} \tilde{X}_l^m. \quad (\text{D.13})$$

¹Whenever we write a \tilde{X}_l^m without arguments, they are assumed to be $(x/R, y/R, z/R)$.

The first few \bar{X}_l^m are

$$\bar{X}_0^0(x, y, z) = 1 \quad (\text{D.14})$$

$$\bar{X}_1^0(x, y, z) = z \quad (\text{D.15})$$

$$\bar{X}_1^1(x, y, z) = x \quad (\text{D.16})$$

$$\bar{X}_1^{-1}(x, y, z) = y \quad (\text{D.17})$$

$$\bar{X}_2^0(x, y, z) = (2z^2 - x^2 - y^2)/2 \quad (\text{D.18})$$

$$\bar{X}_2^1(x, y, z) = \sqrt{3}xz \quad (\text{D.19})$$

$$\bar{X}_2^2(x, y, z) = \sqrt{3}(x^2 - y^2)/2 \quad (\text{D.20})$$

$$\bar{X}_2^{-1}(x, y, z) = \sqrt{3}yz \quad (\text{D.21})$$

$$\bar{X}_2^{-2}(x, y, z) = \sqrt{3}xy. \quad (\text{D.22})$$

Let \tilde{X}_l^m be a solid spherical harmonic. It is a homogeneous function of degree l in the coordinates $(x/R, y/R, z/R)$. Euler's theorem tells us that

$$(\vec{x} \cdot \nabla) \tilde{X}_l^m(x/R, y/R, z/R) = l \tilde{X}_l^m(x/R, y/R, z/R). \quad (\text{D.23})$$

A little calculation shows that

$$\nabla^2(\vec{x} \tilde{X}_l^m(x/R, y/R, z/R)) = 2 \nabla \tilde{X}_l^m(x/R, y/R, z/R), \quad (\text{D.24})$$

and

$$\nabla^2(r^k \tilde{X}_l^m(x/R, y/R, z/R)) = k(k + 2l + 1) r^{k-2} \tilde{X}_l^m(x/R, y/R, z/R). \quad (\text{D.25})$$

Bibliography

- Abe, Y. 1993, *Lithos*, 30, 223
- . 1997, *Physics of the Earth and Planetary Interiors*, 100, 27
- Barker, A. J., & Ogilvie, G. I. 2010, *Monthly Notices of the Royal Astronomical Society*, 404, 1849
- Brouwer, D. 1959, *Astronomical Journal*, 64, 378
- Bulirsch, R., & Stoer, J. 1966, *Numerische Mathematik*, 8, 1, 10.1007/BF02165234
- Běhouňková, M., Tobie, G., Choblet, G., & Čadež, O. 2010, *Journal of Geophysical Research (Planets)*, 115, E09011
- Callegari, N., & Yokoyama, T. 2007, *Celestial Mechanics and Dynamical Astronomy*, 98, 5
- Canup, R. M. 2004, *Annual Review of Astronomy and Astrophysics*, 42, 441
- Chandler, S. C. 1891, *Astronomical Journal*, 11, 59
- Cherniak, D., & Watson, E. 2003, *Reviews in Mineralogy and Geochemistry*, 53, 113
- Connelly, J. N., Amelin, Y., Krot, A. N., & Bizzarro, M. 2008, *Astrophysical Journal Letters*, 675, L121
- Darwin, G. H. 1880, *Royal Society of London Philosophical Transactions Series I*, 171, 713
- Deer, W. A., Howie, R. A., & Zussman, J. 1996, *An introduction to the rock-forming minerals*, 2nd edn. (Essex : Longman Scientific and Technical)
- Dickey, J. O., et al. 1994, *Science*, 265, 482
- Dobrovolskis, A. R. 2007, *Icarus*, 192, 1
- Durham, W. B., Kirby, S. H., & Stern, L. A. 1997, *Journal of Geophysical Research*, 102, 16293
- Dwyer, C. A., & Stevenson, D. J. 2005, *AGU Fall Meeting Abstracts*, A6

- Efroimsky, M., & Williams, J. G. 2009, *Celestial Mechanics and Dynamical Astronomy*, 104, 257
- Elkins-Tanton, L. T. 2008, *Earth and Planetary Science Letters*, 271, 181
- Fischer, H., & Spohn, T. 1990, *Icarus*, 83, 39
- Garrick-Bethell, I., Weiss, B. P., Shuster, D. L., & Buz, J. 2009, *Science*, 323, 356
- Garrick-Bethell, I., Wisdom, J., & Zuber, M. T. 2006, *Science*, 313, 652
- Gavrilov, S. V., & Zharkov, V. N. 1977, *Icarus*, 32, 443
- Ghiorso, M. S., & Sack, R. O. 1995, *Computer*, 119, 197
- Goldreich, P. 1963, *Monthly Notices of the Royal Astronomical Society*, 126, 257
- . 1966, *Reviews of Geophysics and Space Physics*, 4, 411
- . 1967, *Journal of Geophysical Research*, 72, 3135
- Goldreich, P. M., & Mitchell, J. L. 2010, *Icarus*, 209, 631
- Goodman, J., & Lackner, C. 2009, *Astrophysical Journal*, 696, 2054
- Howett, C. J. A., Spencer, J. R., Pearl, J., & Segura, M. 2010, *Icarus*, 206, 573
- Hut, P. 1981, *Astronomy and Astrophysics*, 99, 126
- Jeffreys, H. 1976, *The Earth: Its Origin, History, and Physical Constitution*, sixth edn. (Cambridge : Cambridge University Press)
- Kieffer, S. W., Lu, X., Bethke, C. M., Spencer, J. R., Marshak, S., & Navrotsky, A. 2006, *Science*, 314, 1764
- Kokubo, E., Canup, R. M., & Ida, S. 2000, *Lunar Accretion from an Impact-Generated Disk* (Tucson : The University Of Arizona Press), 145–163
- Kuskov, O. L., & Kronrod, V. A. 1998, *Physics of the Earth and Planetary Interiors*, 107, 285
- Lainey, V., Arlot, J., Karatekin, Ö., & van Hoolst, T. 2009, *Nature*, 459, 957
- Lainey, V., Karatekin, Ö., Desmars, J., & Charnoz, S. 2010, in *Bulletin of the American Astronomical Society*, Vol. 42, AAS/Division of Dynamical Astronomy Meeting #41, 936
- Lamb, H. 1882, *Proceedings of the London Mathematical Society*, 14, 50
- Levrard, B., Correia, A. C. M., Chabrier, G., Baraffe, I., Selsis, F., & Laskar, J. 2007, *Astronomy and Astrophysics*, 462, L5

- Lissauer, J. J., Peale, S. J., & Cuzzi, J. N. 1984, *Icarus*, 58, 159
- Longhi, J. 2003, *Journal of Geophysical Research (Planets)*, 108, 5083
- Love, A. E. H. 1944, *A treatise on the mathematical theory of elasticity*, 4th edn. (New York : Dover)
- Matsuyama, I., & Nimmo, F. 2008, *Icarus*, 195, 459
- Meyer, J., Elkins-Tanton, L., & Wisdom, J. 2010, *Icarus*, 208, 1
- . 2011, *Icarus*, 212, 448
- Meyer, J., & Wisdom, J. 2007, *Icarus*, 188, 535
- . 2008a, *Icarus*, 198, 178
- . 2008b, *Icarus*, 193, 213
- . 2011, *Icarus*, 211, 921
- Mignard, F. 1979, *Moon and Planets*, 20, 301
- . 1980, *Moon and Planets*, 23, 185
- . 1981, *Moon and Planets*, 24, 189
- Moore, W. B. 2004, in *Workshop on Europa's Icy Shell: Past, Present, and Future*, ed. P. Schenk, F. Nimmo, and L. Prockter, 7055–7056
- Murray, C., & Harper, D. 1993, *Queen Mary Maths Notes*, Vol. 15, *Expansion of the Planetary Disturbing Function to Eighth Order in the Individual Orbital Elements* (London : University of London)
- Nemchin, A., Timms, N., Pidgeon, R., Geisler, T., Reddy, S., & Meyer, C. 2009, *Nature Geoscience*, 2, 133
- Newcomb, S. 1892, *Monthly Notices of the Royal Astronomical Society*, 52, 336
- Nimmo, F., Spencer, J. R., Pappalardo, R. T., & Mullen, M. E. 2007, *Nature*, 447, 289
- Ogilvie, G. I., & Lin, D. N. C. 2004, *Astrophysical Journal*, 610, 477
- . 2007, *Astrophysical Journal*, 661, 1180
- Ojakangas, G. W., & Stevenson, D. J. 1986, *Icarus*, 66, 341
- O'Neill, C., & Nimmo, F. 2010, *Nature Geoscience*, 3, 88
- Peale, S. J. 1969, *Astronomical Journal*, 74, 483

- . 1973, *Reviews of Geophysics and Space Physics*, 11, 767
- Peale, S. J. 1986, in *Satellites*, ed. J. A. Burns and M. S. Matthews, 159–223
- . 2003, *Celestial Mechanics and Dynamical Astronomy*, 87, 129
- Peale, S. J., & Cassen, P. 1978, *Icarus*, 36, 245
- Peale, S. J., Cassen, P., & Reynolds, R. T. 1979, *Science*, 203, 892
- Peale, S. J., & Gold, T. 1965, *Nature*, 206, 1240
- Penev, K., & Sasselov, D. 2011, ArXiv e-prints
- Plummer, H. C. 1960, *An introductory treatise on dynamical astronomy* (New York : Dover Publication)
- Poincaré, H. 1910a, *Bulletin Astronomique, Serie I*, 27, 321
- . 1910b, *Comptes rendus de l’Académie des Sciences*, 132, 369
- Porco, C. C., et al. 2006, *Science*, 311, 1393
- Ray, R. D., Eanes, R. J., & Lemoine, F. G. 2001, *Geophysical Journal International*, 144, 471
- Ross, M. N., & Schubert, G. 1989, *Icarus*, 78, 90
- Schubert, G., Spohn, T., & Reynolds, R. T. 1986, in *Satellites*, ed. J. A. Burns and M. S. Matthews, 224–292
- Sinclair, A. T. 1972, *Monthly Notices of the Royal Astronomical Society*, 160, 169
- Sinclair, A. T. 1983, in *Astrophysics and Space Science Library*, Vol. 106, IAU Colloq. 74: *Dynamical Trapping and Evolution in the Solar System*, ed. V. V. Markellos and Y. Kozai, 19–25
- Smith, J. V., Anderson, A. T., Newton, R. C., Olsen, E. J., Crewe, A. V., Isaacson, M. S., Johnson, D., & Wyllie, P. J. 1970, *Geochimica et Cosmochimica Acta Supplement*, 1, 897
- Snyder, G. A., Taylor, L. A., & Neal, C. R. 1992, *Geochim. Cosmochim. Acta*, 56, 3809
- Solomon, S. C. 1986, in *Origin of the Moon*, ed. W. K. Hartmann, R. J. Phillips, and G. J. Taylor, 435–452
- Spencer, J. R., et al. 2006, *Science*, 311, 1401
- Squyres, S. W., Reynolds, R. T., & Cassen, P. M. 1983, *Icarus*, 53, 319
- Stacey, F. D. 1992, *Physics of the Earth*. (Brisbane : Brookfield Press)

- Stevenson, D. J. 2006, AGU Fall Meeting Abstracts, B3
- Sussman, G. J., & Wisdom, J. 2001, *Structure and interpretation of classical mechanics* (Cambridge, Mass.: MIT Press)
- Terquem, C., Papaloizou, J. C. B., Nelson, R. P., & Lin, D. N. C. 1998, *Astrophysical Journal*, 502, 788
- Thompson, C., & Stevenson, D. J. 1988, *Astrophysical Journal*, 333, 452
- Tittlemore, W. C., & Wisdom, J. 1989, *Icarus*, 78, 63
- Toomre, A. 1966, in *The Earth-Moon System*, ed. B. G. Marsden and A. G. W. Cameron, 33–45
- Touboul, M., Kleine, T., Bourdon, B., Palme, H., & Wieler, R. 2007, *Nature*, 450, 1206
- Touma, J., & Wisdom, J. 1994, *Astronomical Journal*, 108, 1943
- . 1998, *Astronomical Journal*, 115, 1653
- . 2001, *Astronomical Journal*, 122, 1030
- Turcotte, D. L., & Schubert, G. 2002, *Geodynamics - 2nd Edition* (Cambridge : Cambridge University Press)
- Vening Meinesz, F. 1947, *Trans. Am. Geophys. Union*, 28, 123
- Ward, W. R. 1975, *Science*, 189, 377
- Warren, P. H. 1986, in *Origin of the Moon*, ed. W. K. Hartmann, R. J. Phillips, and G. J. Taylor, 279–310
- Wieczorek, M. A., & Phillips, R. J. 1999, *Icarus*, 139, 246
- Williams, J. G. 2008, in *16th International Workshop on Laser Ranging*
- Williams, J. G., Boggs, D. H., & Ratcliff, J. T. 2009, in *Lunar and Planetary Institute Science Conference Abstracts*, Vol. 40, 1452–1453
- Williams, J. G., Boggs, D. H., Yoder, C. F., Ratcliff, J. T., & Dickey, J. O. 2001, *Journal of Geophysical Research*, 106, 27933
- Wisdom, J. 2004, *Astronomical Journal*, 128, 484
- . 2006, *Astronomical Journal*, 131, 1864
- . 2008, *Icarus*, 193, 637
- Wisdom, J., & Holman, M. 1991, *Astronomical Journal*, 102, 1528

- Wood, J. A., Dickey, Jr., J. S., Marvin, U. B., & Powell, B. N. 1970, *Geochimica et Cosmochimica Acta Supplement*, 1, 965
- Wu, Y. 2005, *Astrophysical Journal*, 635, 688
- Yin, Q., Jacobsen, S. B., Yamashita, K., Blichert-Toft, J., Télouk, P., & Albarède, F. 2002, *Nature*, 418, 949
- Yoder, C. F., & Peale, S. J. 1981, *Icarus*, 47, 1
- Yoder, C. F., Synnott, S. P., & Salo, H. 1989, *Astronomical Journal*, 98, 1875
- Zahn, J. P. 1966, *Annales d'Astrophysique*, 29, 313
- . 1970, *Astronomy and Astrophysics*, 4, 452
- . 1975, *Astronomy and Astrophysics*, 41, 329
- . 1977, *Astronomy and Astrophysics*, 57, 383
- . 1989, *Astronomy and Astrophysics*, 220, 112